

In vivo NMR-methods to study effects of
atherosclerosis in mice

Dissertation zur Erlangung des
naturwissenschaftlichen Doktorgrades
der Julius-Maximilians-Universität
Würzburg

vorgelegt von

Marco Parczyk

Würzburg 2010

Eingereicht am: 13.08.2010

bei der Fakultät für Physik und Astronomie

1. Gutachter: Prof. Dr. Peter M. Jakob
 2. Gutachter: Prof. Dr. Dr. Wolfgang R. Bauer
- der Dissertation

1. Prüfer: Prof. Dr. Peter M. Jakob
2. Prüfer: Prof. Dr. Dr. Wolfgang R. Bauer
3. Prüfer: Prof. Dr. Wolfgang Kinzel

im Promotionskolloquium

Tag des Promotionskolloquiums: 07.12.2010

Doktorurkunde ausgehändigt am:

In vivo NMR-methods to study effects of
atherosclerosis in mice

von

Marco Parczyk

Julius-Maximilians-Universität Würzburg

2010

Wo liegt die Wohlfühlzone beim IQ?

Contents

1	Motivation	5
2	Fundamentals	9
2.1	Physical Principles of MRI	9
2.1.1	Equilibrium Alignment of Nuclear Magnetization	9
2.1.2	Excitation & Relaxation of the Magnetization	11
2.1.3	Magnetic Resonance Imaging	13
2.1.3.1	Slice Encoding	15
2.1.3.2	Frequency & Phase Encoding	15
2.1.3.3	Small Excitation Angles	17
2.1.4	Motion Measurements in MRI	18
2.1.4.1	Spins Moving in Magnetic Field Gradients	19
2.1.4.2	Motion Compensation	25
2.1.4.3	Motion Encoding	27
2.1.4.4	Artifacts Not Eliminated by Motion Compensation	28
2.2	Biological Principles	31
2.2.1	The Arterial System	31
2.2.2	Atherosclerosis	32
2.2.3	Hemodynamics	33
2.2.3.1	Empirical Hemodynamics	33
2.2.3.2	Hemodynamics and the Navier-Stokes Equations	35
2.2.3.3	Clinical Parameters Describing Hemodynamics	39
2.2.4	The Transit Time Method to Determine the Regional PWV	40
2.2.5	The QA Method to Determine the Local PWV	42
2.3	Animals & Experimental Equipment	44
2.3.1	ApoE ^(-/-) Mice	44
2.3.2	The Magnetic Resonance Tomograph	44
2.3.3	Heart Triggering & Breath Gating	45

3	The Pulsatile Elastic Vessel Phantom	47
3.1	Methods	49
3.1.1	Fabrication of the Phantom Vessel	49
3.1.2	Experimental Setup of the Vessel Phantom	51
3.1.3	Performance Tests on the Vessel Phantom	53
3.2	Results	56
3.3	Discussion	59
4	Transit Time Measurements of Flow Waveforms	61
4.1	Methods	63
4.1.1	The MR Sequence	63
4.1.2	Data Analyzing Software	66
4.1.3	Validation Experiments	67
4.1.4	In Vivo Experiments	69
4.1.4.1	Animal Handling	69
4.1.4.2	Data Acquisition on Mice	69
4.2	Results	73
4.2.1	Validation Experiments	73
4.2.2	In Vivo Experiments	73
4.3	Discussion	79
4.3.1	The MR Sequence	79
4.3.2	Validation Experiments	79
4.3.3	In Vivo Experiments	79
5	Transit Time Measurements of Distension Waveforms	83
5.1	Methods	85
5.1.1	Partial Volume Effect and Zero-Filling	85
5.1.2	Validation Experiments	87
5.1.3	In Vivo Experiments	88
5.1.4	Data Processing	89
5.2	Results	91
5.2.1	Validation Experiments	91
5.2.2	In Vivo Experiments	91
5.3	Discussion	95
5.3.1	Validation Experiments	95
5.3.2	In Vivo Experiments	95

6	The QA-Method	97
6.1	Methods	98
6.1.1	Validation Experiments	98
6.1.2	In Vivo Experiments	98
6.1.3	Data Analysis	99
6.2	Results	101
6.2.1	Validation Experiments	101
6.2.2	In Vivo Experiments	102
6.3	Discussion	105
6.3.1	Validation Experiments	105
6.3.2	In Vivo Experiments	106
7	Summary	111
8	Zusammenfassung	115
	Eigene Veröffentlichungen	131
	Lebenslauf	135
	Ehrenwörtliche Erklärung	137

Chapter 1

Motivation

Cardiovascular diseases (CVD) have superseded infections as the leading cause of death. The World Health Organization (WHO) stated that 29.3% of the worldwide deaths were caused by cardiovascular diseases in the year 2002 [1]. In industrialized countries the fraction is even higher (e.g., USA: 38.1%, Germany: 47.6%). In the year 2002 in Germany the expenditures for the treatment of cardiovascular diseases were one sixth of the total annual expenses in health care [2].

Currently medical research mainly focusses on molecular and cellular biological methods to optimize diagnostics and therapy. Emphasis is laid on the characterization of the interactions between molecular biological processes and the pathology or rather etiopathology of CVD. Therefore, animal models of CVD are phenotyped on a molecular and cellular level. However, *in vivo* examinations on intact animals are necessary for a comprehensive characterization of CVD. This work presents approaches for the *in vivo* characterization of CVD in mice. The CVD focussed on in this work is atherosclerosis.

Atherosclerosis is the main kind of CVD. Pathogenic risk factors include genetic dispositions, male sex, diabetes, lipoprotein abnormalities, increased age, and environmental factors such as smoking and life style. In this work the aorta was examined because it plays a major role in the analysis of atherosclerosis. It provides at least 60 to 70% of systemic compliance [3]. Reduced elasticity and compliance of the aorta are etiologic in atherosclerosis and therefore serve as early indicators of asymptomatic atherosclerotic lesions [4, 5]. The velocity of pressure and flow pulses traveling down an elastic vessel, termed the pulse wave velocity (PWV), increases with arterial stiffness [6]. It serves as a surrogate marker for arterial compliance [7].

A regional average of the PWV can be assessed using the transit time (TT) method [8] which is explained in section 2.2.4. Originally the transit time method had been used to determine the PWV in humans before it was applied to smaller mammals such as mice.

In humans the TT method has been applied using several invasive methods [9, 10] and non-invasive methods such as ultrasound [11, 12] and magnetic resonance imaging (MRI) [13]. To this day the MRI methods have been refined by many workgroups [14, 15] and they constitute a comprehensive technique for the characterization of morphologic and functional arterial systemic parameters in humans. Vulliemoz et al. introduced the QA method (section 2.2.5) to estimate the PWV in humans locally by MR measurements of volume flow and arterial cross sections in the early systole [16].

The foundation of MRI was laid by Bloch and Purcell [17, 18] when they independently discovered the nuclear magnetic resonance (NMR) in 1946. Subsequently NMR was mainly applied as a spectroscopic method to elucidate molecular structures in chemistry. In 1973 Mansfield and Lauterbur introduced the use of magnetic field gradients to impress spatial information onto the NMR signals [19, 20]. This was the essential step towards clinical MRI. In 1975 Kumar presented Fourier imaging [21] which became the standard imaging method. Today clinical MRI is a standardized non-invasive method to investigate the morphology and function of the human organism.

In the past years the need to determine morphologic and functional parameters of the murine arterial system in living animals arose. A genetically engineered phenotype of mice, deficient in apolipoprotein E (ApoE^(-/-) mice), spontaneously develops severe hyperlipidemia and atherosclerotic lesions at the arterial wall [22]. The ApoE^(-/-) mouse develops all stages of lesions observed during atherogenesis resembling lesions found in humans [23]. Because of this and its short generation times the ApoE^(-/-) mouse became an important model for human atherosclerosis [24].

Physical dimensions in mice are approximately 20 times smaller than in humans and mice have high heart rates of 8 to 10 beats per second. The necessities of very high spatial and temporal resolutions constitute the challenges for the determination of the PWV in mice. In MRI of the corresponding animal model the acquirable spatial resolution is limited by the signal-to-noise ratio (SNR). For years MRI systems did not provide a sufficient SNR to allow for PWV measurements in mice.

The SNR increases with the static magnetic field [25]. New high-field MRI systems permit MRI to become an exceptionally capable method for examinations of morphologic and also functional parameters of the arterial system of mice [26, 27, 28, 29]. The advantages of MRI are well known: it is non-invasive and delivers two- or three-dimensional images of the analyzed objects, without the application of ionizing radiation. MRI offers a manifold variety of image contrast parameters, such as proton spin density, longitudinal or transverse relaxation times of excited magnetization, diffusion, and motional velocities. These contrast parameters can be controlled by specifically tailored image acquisition schemes.

In the scope of this work, an image acquisition scheme with high spatial and temporal resolutions that encodes blood flow velocities was designed in order to determine regional and local PWVs in the descending murine aorta.

Before MRI became an alternative for the in vivo determination of the PWV, ultrasound methods have been utilized to non-invasively measure PWVs in mice [30, 31, 32]. However, the results of these ultrasound methods turned out to be highly observer dependent and in general were limited by acoustical windows in the thorax and by angular offsets in the alignment of the ultrasound transducer and the aorta [33]. The limited spatial resolution of ultrasound is a substantial impediment for morphological studies [34].

The primary objective of this study was to develop a high-resolution MR-method and to test the applicability of high-field MRI in combination with the TT and the QA method to assess the regional and local PWVs of the descending murine aorta.

Chapter 2

Fundamentals

2.1 Physical Principles of MRI

Nuclear Magnetic Resonance (NMR) describes the behavior of nuclear spins inside an external magnetic field. In the following the physical principles of NMR will be elucidated as far as they are essential to the comprehension of this research project.

2.1.1 Equilibrium Alignment of Nuclear Magnetization

Atomic nuclei with unpaired nucleons possess a non-evanescent intrinsic angular momentum, termed the nuclear spin \mathbf{I}^* . In quantum mechanics the nuclear spin is described by the following eigen-value equations [35].

$$\begin{aligned} \mathbf{I}^2 |Im\rangle &= \hbar^2 I(I+1) |Im\rangle \\ I_Z |Im\rangle &= \hbar m |Im\rangle \end{aligned} \tag{2.1}$$

A magnetic dipole moment μ is linked to the nuclear spin \mathbf{I} . The magnetic dipole moment is proportional to the nuclear spin; and the constant of proportionality γ is called the gyromagnetic ratio.

$$\mu = \gamma \mathbf{I} \tag{2.2}$$

The gyromagnetic ratio is characteristic to every considered atomic nucleus. In this work hydrogen nuclei were of sole importance. Consequently the hydrogen nucleus will be the only one considered in this work. Its gyromagnetic ratio is $\gamma/2\pi = 42.58 \text{ MHz/T}$.

*The notation in this work shows vectors in bold face type.

The eigen-value equations (2.1) provide discrete eigen-values. Consequently and according to equation (2.2) the magnetic dipole moment can only have discrete values. Without external influences the energy levels of the nuclei are degenerate, but they will separate into $2I + 1$ levels under the influence of a static magnetic field \mathbf{B}_0 . The separated energy levels are indexed by the magnetic quantum number m . In the hydrogen nucleus m can have the values $+1/2$ and $-1/2$. The energy difference between the two energy levels of the hydrogen nucleus is:

$$\Delta E = \gamma \hbar |\mathbf{B}_0|. \quad (2.3)$$

Whereas \hbar is Planck's constant normed to 2π . Quantum transitions between the separated energy levels will be induced when photons with an energy $\hbar\omega_0 = \Delta E$ are irradiated into the system. The phenomenon of induced resonant transitions is called *nuclear magnetic resonance* (NMR). Equating the quantum energy of the photons with the energy difference between the energy levels yields the *Larmor frequency* of the spin system.

$$\omega_0 = \gamma |\mathbf{B}_0| \quad (2.4)$$

The magnetic moment of one single spin is not observable in the NMR experiment. Only the macroscopic magnetization \mathbf{M} can be determined by NMR experiments. Therefore a transition from the quantum mechanical description to classical mechanics will be made here. The macroscopic magnetization \mathbf{M} is composed of the magnetic moments μ_i of large numbers of spins and is defined as the average of the magnetic moments μ_i taken over the volume V .

$$\mathbf{M} = \frac{1}{V} \sum_i \mu_i \quad (2.5)$$

The magnetic moments of single nuclei mutually interact thermodynamically. In the classical approximation, the spin system can be described by the Boltzmann statistics [36]. For a sample of material, the macroscopic magnetization in thermodynamic equilibrium is defined as [37]:

$$\mathbf{M}_0 = \frac{\rho_0 \gamma^2 \hbar}{4k_B T} \mathbf{B}_0. \quad (2.6)$$

Whereas ρ_0 indicates the spin density of the sample, k_B is the Boltzmann number, and T is the absolute temperature. Equation (2.6) describes the orientation of \mathbf{M}_0 to be parallel to \mathbf{B}_0 in thermal equilibrium. At magnetic field strengths of a few tesla and at common temperature the surplus of magnetic moments populating the lower energy level will be of the order of 10^{-6} to 10^{-5} of the total number of nuclei.

2.1.2 Excitation & Relaxation of the Magnetization

In the following, $\mathbf{B}_0 = (0, 0, B_0)$ shall be fixed to the z direction of a Cartesian laboratory coordinate system without loss of generality. The alignment of the macroscopic magnetization \mathbf{M} to \mathbf{B}_0 can be disturbed by a magnetic field \mathbf{B}_1 which is oriented perpendicularly to the z direction and rotates in the xy plane of the laboratory coordinate system with the Larmor frequency ω_0 . This is the classical analogy to the induction of quantum transitions between the energy states of magnetic moments. The magnitude of \mathbf{M} is constant under the influence of \mathbf{B}_1 . The angle α of \mathbf{M} (relative to the z direction) will change and is given by the following equation wherein τ is the time in which the \mathbf{B}_1 -field is interfering.

$$\alpha = \gamma \int_{\tau} \mathbf{B}_1(t) dt. \quad (2.7)$$

In the practice of NMR experiments the oscillating magnetic field $\mathbf{B}_1(t)$ is generated by pulses of electromagnetic radiation in the radio frequency range, shortly termed **R F p u l s e s**. The RF pulses are named according to the angle of rotation α which they generate. The selective perturbation of the magnetization in NMR is termed excitation. A common RF pulse is the 90° pulse which flips \mathbf{M} into the xy plane of the coordinate system, termed the transversal plane. Another common example is the 180° pulse. It inverts \mathbf{M} .

In the classical approach the behavior of the macroscopic magnetization $\mathbf{M}(t)$ is described by the Bloch equations [17].

$$\frac{dM_x}{dt} = \gamma (M_y B_z - M_z B_y) - \frac{M_x}{T_2} \quad (2.8)$$

$$\frac{dM_y}{dt} = \gamma (M_z B_x - M_x B_z) - \frac{M_y}{T_2} \quad (2.9)$$

$$\frac{dM_z}{dt} = \gamma (M_x B_y - M_y B_x) - \frac{M_z - M_0}{T_1} \quad (2.10)$$

B_i designates the Cartesian components of a net magnetic field \mathbf{B} which is compounded of the static field \mathbf{B}_0 and the rotating field \mathbf{B}_1 .

The terms on the right side that contain the characteristic time constants T_1 and T_2 describe relaxation processes towards thermal equilibrium of the magnetization.

T_1 is the **s p i n - l a t t i c e r e l a x a t i o n t i m e**. It describes the interaction of the spin system with the environment (e.g. a crystal lattice) that follows a perturbation by e.g. a \mathbf{B}_1 field. The system does exchange energy with its environment. Consequently the longitudinal component of the magnetization M_z will change towards the equilibrium magnetization M_0 [38].

$$M_z(t) = M_z(0) e^{-t/T_1} + M_0 (1 - e^{-t/T_1}) \quad (2.11)$$

T_1 is a measure for the time which the magnetization needs to reach the thermodynamical equilibrium. Biological tissues have T_1 values in the range of a few milliseconds to several seconds.

T_2 is the *s p i n - s p i n r e l a x a t i o n t i m e*. It describes the overall exponential decay of the transversal component of the magnetization M_{xy} . The spin-spin relaxation time constant includes two relaxation processes. One of them is the spin-lattice relaxation mechanism, the other is the spin-spin relaxation process. During the spin-spin relaxation process no energy is exchanged with the environment; rather the process is an irreversible entropic effect. Directly after the excitation by the \mathbf{B}_1 field, the spins of the system exhibit coherent phases. Due to interactions between the spins, their coherence and, hence, the magnitude of the transversal magnetization will decay.

$$M_{xy}(t) = M_{xy}(0) e^{-t/T_2} \quad (2.12)$$

In biological tissues the T_2 values range from 40 ms to 1 s. Because T_2 includes the spin lattice relaxation process, the spin-spin relaxation time must be shorter than the spin-lattice relaxation time, $T_2 < T_1$.

The terms $dM_i/dt = (M_j B_k - M_k B_j)$ of the Bloch equations (2.8, 2.9, 2.10) describe a precession of the magnetization \mathbf{M} around the magnetic field \mathbf{B} . The precession of \mathbf{M} inside the magnetic field \mathbf{B} can be visualized by a gyroscope precessing inside the gravitational field of the earth. A precessing magnetization \mathbf{M} induces a voltage at the ends of a stationary loop or solenoid of conductive wire; hence solenoids or loops of wire can be used to detect signals in NMR.

$$U_{ind} = -\dot{\Phi} = - \int_V \frac{d}{dt} (\mathbf{B}'_1(\mathbf{r}) \cdot \mathbf{M}(\mathbf{r})) dV \quad (2.13)$$

The magnetic flux through a loop of wire is symbolized by Φ , V identifies the volume of the sample, $\mathbf{B}'_1(\mathbf{r})$ denotes the magnetic field strength at the position \mathbf{r} that would be generated by a unit current of 1 ampere flowing inside the wire loop, and \mathbf{M} is the magnetization of the sample at the position \mathbf{r} . When the geometrical axis of the loop is in the xy plane, as is usually the case in MR, then the magnitude of the induced voltage is directly proportional to the transversal component of the magnetization M_{xy} .

Under the assumption of a perfectly homogeneous magnetic field \mathbf{B}_0 , the excited transversal magnetization M_{xy} will induce a signal voltage U_{ind} with the shape of a sine wave in a detector coil; and the magnitude of the signal will decay exponentially (Eq.2.12). This signal is called *f r e e i n d u c t i o n d e c a y* (FID). The time constant of the decay is T_2 . In reality the signal decays with an effective time constant T_2^* which is shorter than T_2 . Inhomogeneities of the magnetic field cause a distribution of the resonance frequencies and

accelerate the dephasing of the nuclear spins. The measurable signal is a superposition of a frequency distribution of decaying sine waves. Eq.(2.14) shows the composition of T_2^* . The effects caused by the field inhomogeneities are represented by T_2' .

$$\frac{1}{T_2^*} = \frac{1}{T_2} + \frac{1}{T_2'} \quad (2.14)$$

2.1.3 Magnetic Resonance Imaging

In the previously described NMR experiment the magnetization was excited in the whole sample and the signal was detected from the same volume. In MRI the main goal is to obtain information about the spatial distribution of the nuclei. The contemporary standard of spatial encoding was developed by Kumar in 1975 [21] and is called *F o u r i e r i m a g i n g*. The method uses magnetic gradient fields G in superposition to the main magnetic field \mathbf{B}_0 to generate a spatial dependence of the Larmor frequency ω_0 . In general the magnetic gradient fields are generated, so that they have spatial linearity.

$$G_x = \frac{\Delta B}{\Delta x} = \text{const.} \quad (2.15)$$

Therefore the Larmor frequency will also show a linear spatial dependence.

$$\omega(x) = \omega_0 + \gamma G_x x \quad (2.16)$$

The spatially dependent component $\gamma G_x x$ is relatively small compared to ω_0 . Usually it lies within the audio range and can extend up to a few hundred kilohertz.

Three gradient fields (G_x, G_y, G_z) can be used to obtain a complete spatial encoding in a Cartesian coordinate system. Overall the magnetic field lines of the gradient fields are parallel to \mathbf{B}_0 and the magnitude of each gradient field changes with the direction that is indicated in the assignment of each particular gradient field. Technically the magnitude is set to zero at the center of the coordinate system. This point is called the iso-center. The iso-center is located in the region where \mathbf{B}_0 features maximum homogeneity, i.e. in the magnet center. The three gradient fields are generated by a set of three gradient coils. In MRI on small animals, gradient strengths of up to 1T/m and cycle times of a few hundred microseconds are common.

In the following, an imaging experiment will be described on the example of a *g r a d i e n t e c h o* experiment. The scheme of the experiment is depicted in Fig.2.1. The three field gradients are called the read, phase, and slice gradients. Without loss of generality the gradients are affixed to the $x, y,$ and z directions in the following explanations. In general

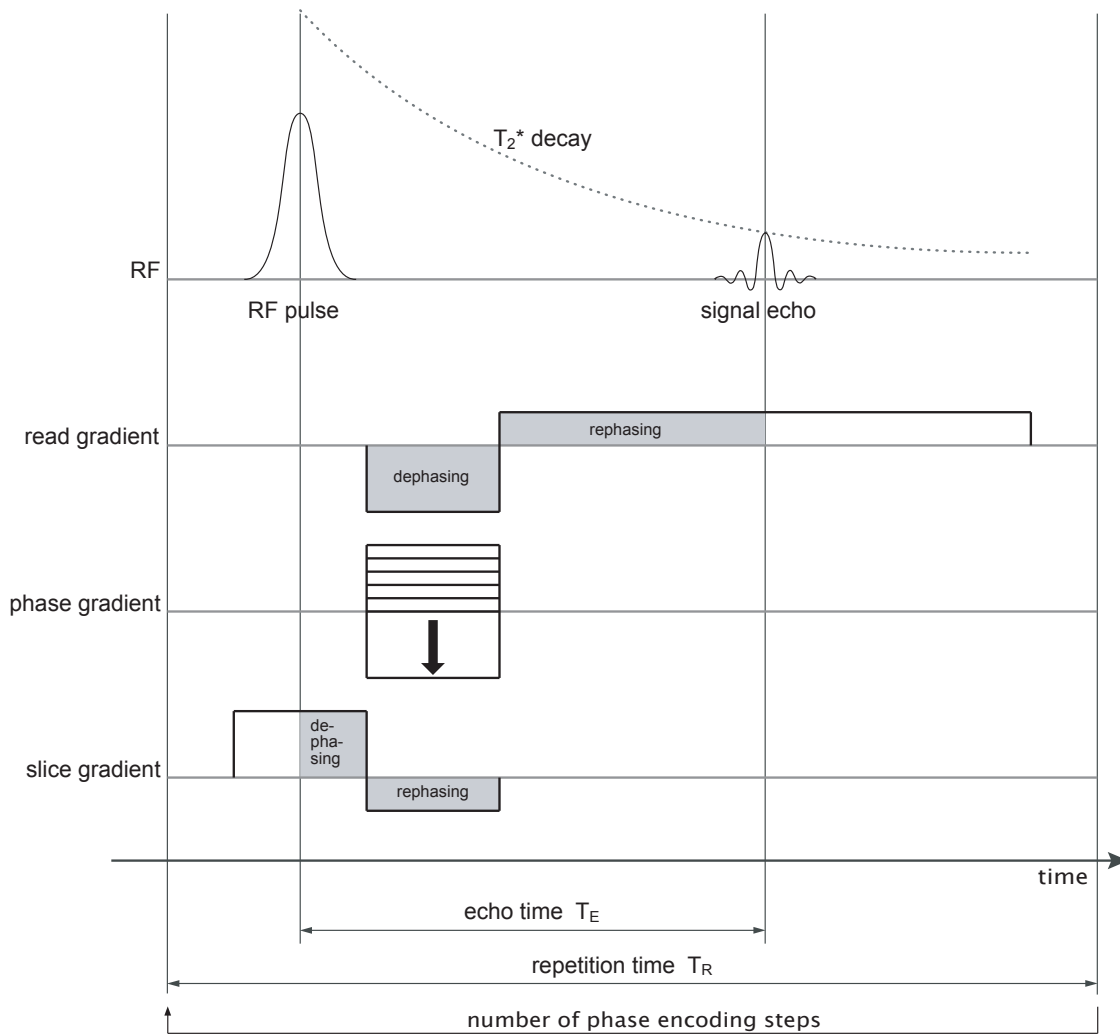


Figure 2.1: Switching scheme of a gradient echo experiment. The gradient switching curves show an idealized switching pattern in which the final amplitudes are reached instantaneously. In reality the ramps are gradual. The shaded areas in the read and slice gradients demonstrate the rephasing condition which states that the spin phases are rephased when the integral of the gradient curves is zero. The signal echo is formed when the spins are rephased. The phase encoding gradient is set to a different amplitude for each phase encoding step.

the gradients can be aligned in any preferred orientation under the condition that they remain mutually orthogonal. This can be achieved by forming linear combinations of the x , y , and z gradients. Mathematically the stationary x , y , z coordinate system can be converted to any arbitrary coordinate system by multiplication with a rotary matrix.

2.1.3.1 Slice Encoding

Spatial encoding in the slice direction is performed during the excitation of the magnetization by the RF pulse (Fig.2.1). The pulse has the center frequency ν_{Pulse} and the bandwidth $\Delta\nu_{Pulse}$. Simultaneous application of the slice selection gradient with the gradient strength G_s excites only magnetization within a slice of the thickness STh when the following relation is fulfilled.

$$STh = \frac{2\pi}{\gamma} \cdot \frac{\Delta\nu_{Pulse}}{G_s} \quad (2.17)$$

The position of the slice is adjusted by an appropriate frequency offset in the center frequency ν_p of the RF pulse and the slice thickness is set by the pulses bandwidth $\Delta\nu_p$ and the field gradient. The profile of the excited slice is approximately the Fourier transform of the envelope of the pulse's waveform [39]. For example, in the time domain the envelope of the RF pulse must be a sinc profile to excite a rectangular slice profile.

The spins within the slice have different Larmor frequencies due to the slice selection gradient field and will, therefore, dephase. The coherence of the phases is restored by the slice refocusing gradient field $G_{s,Ref}$, which follows the slice selection gradient field. The spins are refocused when the following relation holds.

$$\int G_{s,Ref} dt = \int_{RF\ pulse\ center}^{end\ of\ G_s} G_s dt \quad (2.18)$$

2.1.3.2 Frequency & Phase Encoding

The spatial encodings of the read and phase directions are performed after the excitation of the magnetization. The cumulative signal $S(t)$ that is to be detected is the sum of contributions from signal sources or spin isochromats within the excited slice. Neglecting relaxation effects $S(t)$ can be described by the following equation:

$$S(t) = \iint \rho(x, y) e^{-i\phi(x, y, t)} dx dy . \quad (2.19)$$

Here $\rho(x, y, t)$ is the effective spin density within the sample which depends on the actual spin density, the magnetic field strength \mathbf{B}_0 , and the intensity of the RF pulse at the location (x, y) . The phase ϕ of the signal contributions is made spatially dependent by the read gradient G_r and by the phase gradient G_p .

$$\phi(x, y, t) = \gamma \int (x G_r(t) + y G_p(t) + B_0) dt \quad (2.20)$$

Only the phase contributions from the gradients are needed to extract the spatial information from the signal $S(t)$. The contribution of the B_0 field is eliminated by down-mixing

the signal frequency to 0 Hz. Mathematically this is done by the multiplication with a reference frequency ω_L which produces a down-mixed signal and one with twice the frequency. Practically, double balanced mixers (DBM) are used in combination with a low pass filter. After the down-mixing and with the definitions of:

$$k_x = \gamma \int G_r dt \quad (2.21)$$

$$k_y = \gamma \int G_p dt, \quad (2.22)$$

and the assumption of stationary spins, equation (2.19) becomes:

$$S(k_x, k_y) = \iint \rho(x, y) e^{-ik_x x} e^{-ik_y y} dx dy. \quad (2.23)$$

Equation (2.23) shows that the detected signal S is the Fourier transform of the effective spin density $\rho(x, y)$. The other way around, the inverse Fourier transform of the signal $S(k_x, k_y)$ that is measured in the time domain yields the spatial distribution of the effective spin density, synonymic to the NMR tomogram.

$$\rho(x, y) = \frac{1}{2\pi} \iint S(k_x, k_y) e^{ik_x x} e^{ik_y y} dk_x dk_y \quad (2.24)$$

The parameters k_x and k_y must be varied in order to be able to reconstruct the NMR tomogram. The image is recorded in k -space. The k -space data must be Fourier transformed in order to obtain the NMR tomogram. The equations (2.21 & 2.22) point out that the variation of k_x and k_y is achieved by varying the magnitude of the magnetic field gradients or their activation time.

The activation time of the constant read gradient G_r passes through during the readout of the signal. N_r discrete data points are recorded along one k -space line in the read direction k_x during the acquisition time T_{acq} . This encoding method is called frequency encoding. The separation between the data points Δt is called the *d w e l l t i m e*. The reciprocal value is the *s w e e p w i d t h* SW . Each k -space line is recorded with a different phase value k_y . In the current experiment a gradient refocused echo of the transversal magnetization (shortly termed: gradient echo) is recorded (Fig.2.1) instead of the previously described FID. The transversal magnetization is dephased by the read dephase gradient directly after the slice selection. The following readout field gradient G_r rephases the magnetization to produce the gradient echo. The lag between the center of the RF pulse and the echo is called the *e c h o t i m e* T_E . Generally the echo time shall be minimized because the magnitude of the signal decays with the time constant T_2^* . Therefore, it is common to adjust the read dephasing field gradient in order that the signal echo maximum occurs when a quarter of the acquisition time T_{acq} has passed [40]. The

gradient echo is recorded N_p times. The magnitude of the phase encoding field gradient G_p is incremented every time. The activation time of the phase encoding field gradient is constant. In this way k_y is varied and the spatial encoding in the phase direction is accomplished. Every phase encoding step takes the time T_R , the r e p e t i t i o n t i m e.

The reconstructed MR tomogram has the matrix size $N_p \times N_r$. The image section is called the field of view (FOV) and depends on the maximum magnitude of the readout and the phase encoding field gradients. Due to the Nyquist theorem [41] the following equations hold true.

$$\Delta k_x = \gamma G_r \cdot \Delta t = \frac{2\pi}{FOV_r} \quad (2.25)$$

$$\Delta k_y = \gamma \Delta G_p \cdot \tau_p = \frac{2\pi}{FOV_p} \quad (2.26)$$

Δt is the sample rate, τ_p is the time G_p is active, and ΔG_p is the phase encoding gradient increment that is applied for every phase encoding step.

2.1.3.3 Small Excitation Angles

The application of 90° RF pulses produces the maximum transversal magnetization and delivers the maximally possible signal amplitude. The complete longitudinal magnetization is excited to the transversal plane. A relatively long repetition time must pass before the next RF pulse can be applied in order that a sufficient amount of longitudinal magnetization can build up again.

$$TR \gg T_1 \quad (2.27)$$

Therefore, the use of 90° RF pulses lengthens the acquisition time.

In 1986 Haase et al. [42] presented a method to reduce the repetition time. The method is a gradient echo sequence with RF pulses that deflect the longitudinal magnetization by small angles $\alpha \ll 90^\circ$. Thus only a small portion of the longitudinal magnetization is expended when the magnetization is excited. For example, a 10° RF pulse generates 17% of the maximally obtainable transversal magnetization and uses only 1.5% of the longitudinal magnetization. The method is called FLASH, the short term for Fast Low Angle SHot. With this method the phase encoding steps are acquired in direct succession without any delay dedicated to spin lattice relaxation. For artifact-free imaging, it is very important that the longitudinal magnetization has a constant value before every RF pulse. Only then will all acquired k-space lines have consistent signal amplitudes. The concurrence of perpetually repeated excitation of magnetization and spin lattice relaxation

will generate a steady state of longitudinal magnetization after a few RF pulses. The flip angle that produces the maximum signal in steady state is called the Ernst angle. For $T_R \ll T_1$ it is given by [37]:

$$\Theta_E \approx \sqrt{\frac{2T_R}{T_1}}. \quad (2.28)$$

The sequences used in this work are based on the FLASH method.

2.1.4 Motion Measurements in MRI

Motion detection in MRI is commonly achieved by spin tagging, the time-of-flight method, phase velocity encoding, or displacement encoding with stimulated echoes (DENSE).

With spin tagging, the spins within the imaging slice are tagged by selective saturation [43] or a modulation of the magnetization vector [44] in order that the image will show a grid pattern of reduced signal intensity. Between RF excitation and acquisition, in-plane motion of the spins is detected as a deformation of the otherwise periodical pattern.

A disadvantage of this very fast and robust method is that the grid distortions must be estimated in order to obtain velocity values; this is an additional source of error. Further, the grating of the grid is limited to resolutions inferior to the intrinsic image resolution. The method can only determine motion within the plane of the imaging slice; through-slice motion is not detectable.

The time-of-flight method quantifies motion perpendicular to the imaging slice. The spins are marked by a saturation pulse in one slice [45] and can be detected in a parallel slice when they have the appropriate velocity. The velocity is calculated from the slice displacement and the time of flight [46].

The main application of this method is the determination of flow velocities in angiography. The velocity measurement is based on the signal intensity; thus the measurement is affected by T_1 and T_2 relaxation. The method can only determine the maximum velocity of a flow profile inside a vessel. Imaging cannot be performed simultaneous to the velocity determination.

Phase velocity encoding uses the fact that spins of nuclei moving inside a magnetic gradient field will acquire an additional, velocity-dependent phase. Several acquisitions of the same sample with different encoding gradient strengths can be compared to determine the velocity of every voxel. The need to record several data sets extends the acquisition time.

The method has several advantages which made it the method of choice for velocity measurements in this work. Every data set contains image and velocity data that are directly accessible without the need for additional measurement procedures. Velocity distributions are acquired with the image resolution. Motion detection can be performed in all three spatial directions. The physical and mathematical background that is needed to understand the functional principle of this method is given in section 2.1.4.1.

DENSE, developed by Aletras et al. [47], combines the advantages of spin tagging and phase velocity encoding to detect displacements over periods of time that are comparable to T_1 with the spatial resolution of the image. DENSE requires small gradient fields for displacement encoding and modulates the spin phase according to a shift in position rather than its velocity. The magnetization vector is stored along the direction of the \mathbf{B}_0 field during displacement encoding to avoid T_2^* effects. DENSE was developed to encode slower motion. Rapidly flowing blood typically provides no signal because the blood leaves the imaging slice during the long echo times.

2.1.4.1 Spins Moving in Magnetic Field Gradients

The motion of spins during an MR experiment has manifold consequences on the results of a measurement. The consequences include phase shifts and intensity diminution of the signal and are dependent on the orientation of magnetic field gradients and the direction of motion.

Considering the one-dimensional case of spins moving in a gradient field; the accumulated phase is described in analogy to Eq.(2.20) but now the position x is time dependent.

$$\phi(x, t) = -\gamma \int x(t) G_x(t) dt \quad * \quad (2.29)$$

The effects of constant velocity and of acceleration on the phase become clear when $x(t)$ is described by its Taylor expansion in time

$$x(t) = x_0 + \dot{x} \cdot t + \frac{1}{2} \ddot{x} \cdot t^2 + \dots \quad (2.30)$$

and inserted into (2.29).

$$\phi(x, t) = -\gamma \int x_0 G_x(t) dt - \gamma \int \dot{x} G_x(t) t dt - \gamma \int \ddot{x} \frac{1}{2} G_x(t) t^2 dt - \dots \quad (2.31)$$

The left product term on the right side of Eq.2.31 describes the phase accumulation of an isochromat of stationary spins. It is used for spatial encoding as described in section

*The influence of \mathbf{B}_0 has been eliminated by down-mixing the signal.

2.1.3.2. The second term contains the velocity dependent part of the phase and the third term specifies the part that is determined by acceleration.

In order to simplify the notation it is beneficial to introduce the gradient moments M_n .

$$M_n := \int G(t) t^n dt \quad (2.32)$$

The power in the time specifies the order n of the gradient moment. Eq.(2.31) can now be written as:

$$\phi = -\gamma x_0 M_0 - \gamma \dot{x} M_1 - \frac{\gamma}{2} \ddot{x} M_2 - \dots \quad (2.33)$$

$$= \phi_s + \phi_v + \phi_a + \dots \quad (2.34)$$

In the following, the influence of the velocity-dependent phase component ϕ_v shall be discussed. The influence of acceleration and higher order terms are neglected. Idealized boxcar switch curves of the gradients will be assumed. This means the gradients instantly switch to the specified value and remain constant until the next value is specified.

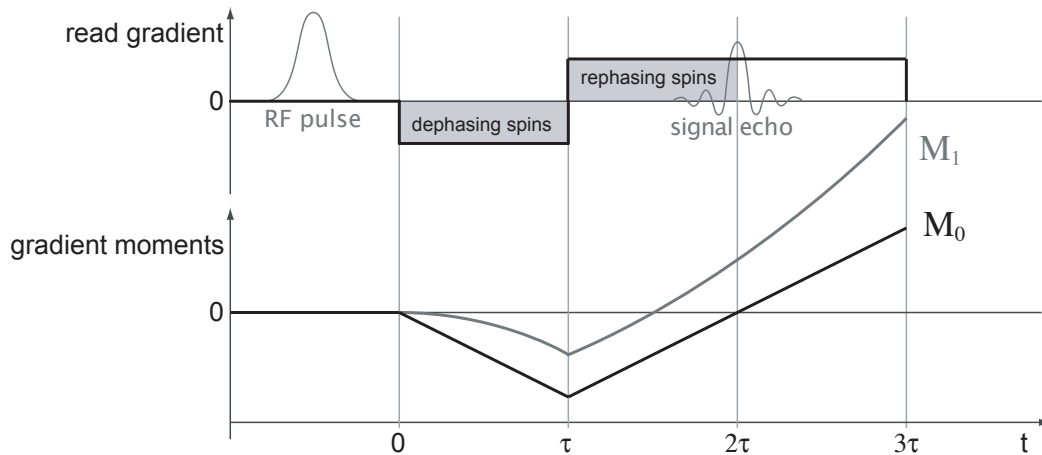


Figure 2.2: Spins moving with constant velocity under the influence of the read gradient fields of a gradient echo sequence. The gradient moment M_0 is zero at the echo time 2τ to form a signal echo. The gradient moment M_1 is not zero at the echo time 2τ . This means that the phase contributions due to motion of spins are not refocused at that time. The phases of stationary and moving spins are given by $\phi_s(t) = -\gamma x_0 M_0(t)$ and $\phi_v(t) = -\gamma \dot{x} M_1(t)$, respectively.

While the spins move they undergo a series of gradient fields. In a gradient echo sequence, the first gradient lobe in the read encoding direction dephases the spins and the following lobe is supposed to rephase them to generate the signal echo.

Fig.2.2 illustrates that this holds true only for stationary spins. Moving spins are not rephased at the echo time 2τ . After the time τ the phase is given by [37]:

$$\phi_{\text{Dephased}}(\tau) = -\gamma G x_0 \tau - \frac{1}{2} \gamma G v_x \tau^2, \quad (2.35)$$

and the accumulated phase during the rephasing is:

$$\phi_{\text{Rephasing}}(t) = -\gamma G x_0 (t - \tau) - \frac{1}{2} \gamma G v_x (t^2 - \tau^2) \quad \tau \leq t \leq 3\tau. \quad (2.36)$$

Setting the point of origin of time to the center of the echo $t' = t - 2\tau$ and addition of ϕ_{Dephased} and $\phi_{\text{Rephasing}}$ yields the total spin phase as:

$$\phi(t') = \phi_s(t') + \phi_v(t'), \quad (2.37)$$

$$\text{with } \phi_s(t') = -\gamma G x_0 t' \quad (2.38)$$

$$\text{and } \phi_v(t') = -\frac{1}{2} \gamma G v_x (t'^2 + 4\tau t' + 2\tau^2). \quad (2.39)$$

The terms within the brackets of Eq.(2.39) have different impacts on the signal. The contribution $-\frac{1}{2} \gamma G v_x t'^2$ acts as a filter on the signal and causes `blurring` and signal loss in the image [48, 49]. The expression $-\frac{1}{2} \gamma G v_x 4\tau t'$ can be rewritten as $-k_x 2v_x \tau$. It represents a `shift in position` from x_0 to $x_0 + v_x \tau$. The third term $-\frac{1}{2} \gamma G v_x 2\tau^2$ shows that, in contrast to stationary spins, the phase of moving spins will not be zero at the center of the echo.

Moving spins also generate artifacts in the image. `Intra-voxel dephasing` of spins occurs when flow velocity gradients exist inside a vessel, for example, when a parabolic flow profile exists in the case of laminar flow. In this case v_x varies along the radial direction of the vessel. For insufficient image resolutions, a non-negligible velocity gradient can exist within a voxel. In that case, the velocity-dependent phase values within the voxel will superpose and the signal intensity may be diminished. Under the assumptions that the velocity distribution is constant in time and that v_x varies linearly with the y -direction ($v_x(y) = v_x(x_0, y_0) + \alpha(y - y_0)$) within the voxel ($\Delta x, \Delta y$, slice thickness), the signal contribution of the moving spins is given by [37]:

$$\begin{aligned} \rho_v(x_0, y_0) &= \frac{\rho(x_0, y_0)}{\Delta y} \int_{y_0 - \frac{\Delta y}{2}}^{y_0 + \frac{\Delta y}{2}} dy e^{-i\gamma G v_x(x_0, y_0)\tau^2} e^{-i\gamma G \alpha(y - y_0)\tau^2} \\ &= \rho(x_0, y_0) e^{-i\gamma G v_x(x_0, y_0)\tau^2} \text{sinc}\left(\gamma \alpha G \tau^2 \frac{\Delta y}{2}\right). \end{aligned} \quad (2.40)$$

The exponent $-i\gamma G v_x(x_0, y_0)\tau^2$ specifies the phase in the center of the voxel and reflects the average velocity within the voxel. The `sinc`-term specifies the signal intensity which

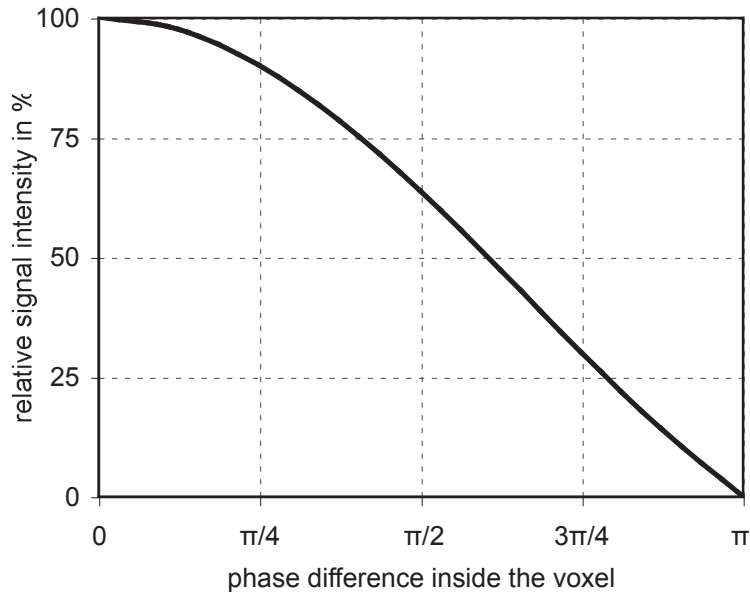


Figure 2.3: Signal extinction due to intra-voxel dephasing. The diagram shows the relative signal intensity depending on the phase difference between the center and the edge of the voxel.

is diminished due to intra-voxel dephasing. When $\gamma\alpha G\tau^2\frac{\Delta y}{2} = \pi$ the *sinc*-term becomes zero; viz. the signal will be completely extinct. Intra-voxel dephasing can be avoided by the application of velocity compensated gradient sequences which will be discussed later.

Without velocity compensation, the spins moving in the slice encoding direction undergo intra-voxel dephasing while the slice-select and slice-rephasing gradients are active. During signal acquisition no gradients are activated in the slice direction. Thus, the portion of the spin phase due to motion in the slice direction is constant during signal readout.

In the reconstructed image, spins do appear at the position where they were located during encoding by the corresponding gradient. In the slice-select direction, spins are encoded during RF excitation. Moving spins may leave the imaging slice after the RF excitation. The position in the read-direction is encoded during signal readout. In the reconstructed image, all spins are misleadingly displayed within the imaging slice although they were at different positions during the read and slice encoding steps. This causes a *d i s p l a c e m e n t a r t i f a c t* (Fig.2.4) which is especially noticeable in vascular blood flow when the vessel traverses the imaging slice in a non-perpendicular angulation or bends off after it traversed the slice [50, 51]. The echo time T_E must be kept as short as possible in order to minimize the displacement artifact [52].

Motion in the phase encoding direction induces a *m i s r e g i s t r a t i o n a r t i f a c t* that

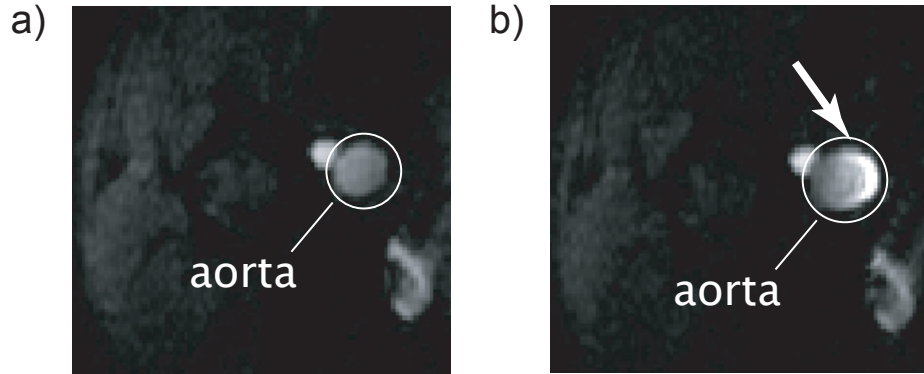


Figure 2.4: The displacement artifact occurs when blood flow traverses the imaging slice non-perpendicularly. Motion compensation does not eliminate the artifact. **a:** Diastolic cross-sectional image of the thoracic aorta of a mouse. Due to slow blood flow the artifact does not appear. **b:** The displacement artifact (indicated by the arrow) is prominent during systolic flow. In this image it presents itself as a bright margin. The artifact can appear as alternating bands of bright and dark contrast for cases where the angle between the slice and flow vectors is larger than in this imaging experiment.

has a cause similar to the displacement artifact in the slice encoding direction. The phase encoding gradient is active after the slice selection and before the read-direction encoding. Spins that moved between the different encoding steps will not be displayed at the correct position in the reconstructed image.

In Fig.2.5 a spin moves within the selected slice with an angle of 40° to the read-direction. During the phase encoding time t_p the spin's y coordinate is encoded. Subsequently it moves with the velocity \mathbf{v} . At the echo time T_E the x coordinate of its position is encoded. In the reconstructed image the spin appears at the coordinate $(x(T_E), y(t_p))$ where it physically never has been. For a constant velocity \mathbf{v} the misregistration in the phase encoding direction is:

$$\Delta y = -v_y (T_E - t_p). \quad (2.41)$$

The misregistration artifact can be explained mathematically when the phase is examined. In the following derivation it is crucial that the origin of time $t = 0$ is set to the center of the echo (see Fig.2.6). For the calculation of one specific gradient moment, the time scale can only be chosen freely when all gradient moments of lower order are zero at the center of the echo [37]. In phase encoding the zeroth gradient moment is not equal to zero. The phase contribution of motion under the phase encoding gradient is:

$$\phi_{v,p}(0) = -\gamma M_1^p(0) v_y \quad (2.42)$$

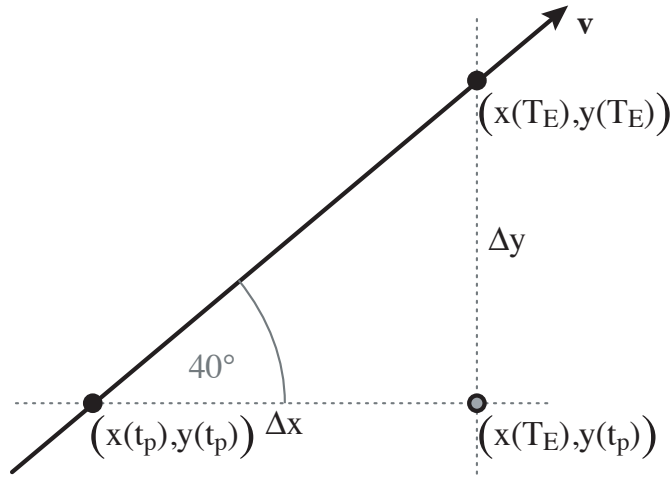


Figure 2.5: Misregistration artifact in the phase encoding direction. The spin is imaged in the position $(x(T_E), y(t_p))$ where it physically never has been.

$M_1^p(0)$ is the first gradient moment of the phase encoding direction at $t = 0$.

$$M_1^p(0) = \int_{-\infty}^0 G_p(t) t dt = \int_{-t_p - \frac{\tau_p}{2}}^{-t_p + \frac{\tau_p}{2}} G_p(t) t dt \quad (2.43)$$

$$= G_p \tau_p t_p \quad (2.44)$$

Insertion of (2.44) into (2.42) yields:

$$\phi_{v,p}(0) = -\gamma G_p \tau_p t_p v_y = -k_y v_y t_p, \quad (2.45)$$

with $k_y = \frac{\gamma}{2\pi} G_p \tau_p$. Neglecting intra-voxel dephasing, the measured signal has the same magnitude as when the spins were stationary. Due to the motion of the spins, the phase of the signal will be shifted linearly with k_y . The signal due to motion is given by:

$$S_v(k_y) = S(k_y) \cdot e^{i\phi_{v,p}}. \quad (2.46)$$

By Fourier transformation from k-space to position space the phase windup due to motion in (2.46) turns into a shift in position, as given in Eq.2.41.

$$\begin{aligned} \rho_v(y) &= \int_{-\infty}^{\infty} dk_y S_v(k_y) e^{ik_y y} \\ &= \int_{-\infty}^{\infty} dk_y S(k_y) e^{ik_y y} e^{-ik_y v_y t_p} \end{aligned}$$

$$\begin{aligned}
&= \int_{-\infty}^{\infty} dk_y S(k_y) e^{ik_y(y-v_y t_p)} \\
&= \rho(y - v_y t_p)
\end{aligned} \tag{2.47}$$

2.1.4.2 Motion Compensation

Motion compensating gradient switching sequences [53] reduce the motion induced errors in the phase values and intra-voxel dephasing. The displacement artifact in the slice direction will not be reduced by motion compensating sequences.

The goal of motion compensation is to prevent an additional phase accumulation due to the first gradient moments [54][†]. Therefore, the first order gradient moments must be zero at the echo center [48, 55]. Concurrently, the zeroth order gradient moments must remain unaltered, because they are responsible for the spatial encoding.

For the read and for the slice encoding gradients there are three constraints that must be fulfilled by the switching scheme:

- The gradient amplitudes are defined by the field of view, the sweep width, and the slice thickness Eqs. 2.25 & 2.17.

$$G_r = \frac{2\pi}{\gamma} \cdot \frac{SW}{FOV_r} \tag{2.48}$$

$$G_s = \frac{2\pi}{\gamma} \cdot \frac{\Delta\nu_{Pulse}}{STh} \tag{2.49}$$

- The zeroth order gradient moments must be zero at time $t = 0$ in order to form a signal echo.

$$M_0(0) = \int_{-\infty}^0 dt G(t) = 0 \tag{2.50}$$

- The first order gradient moments must be zero at time $t = 0$ in order to rephase the moving spins.

$$M_1(0) = \int_{-\infty}^0 dt t G(t) = 0 \tag{2.51}$$

Generally, two-lobed gradients, as in Fig.2.1 on page 14, only have two degrees of freedom and thus can not satisfy the three constraints. The third degree of freedom is obtained by the addition of a third gradient lobe to the read and slice gradients. Fig.2.6 shows a motion compensated switching scheme for the read gradient.

[†]Artifacts resulting from non-vanishing gradient moments of higher orders (such as the second order moment caused by acceleration) are neglected in the following considerations. The discussed motion compensation schemes only involve the first order gradient moment.

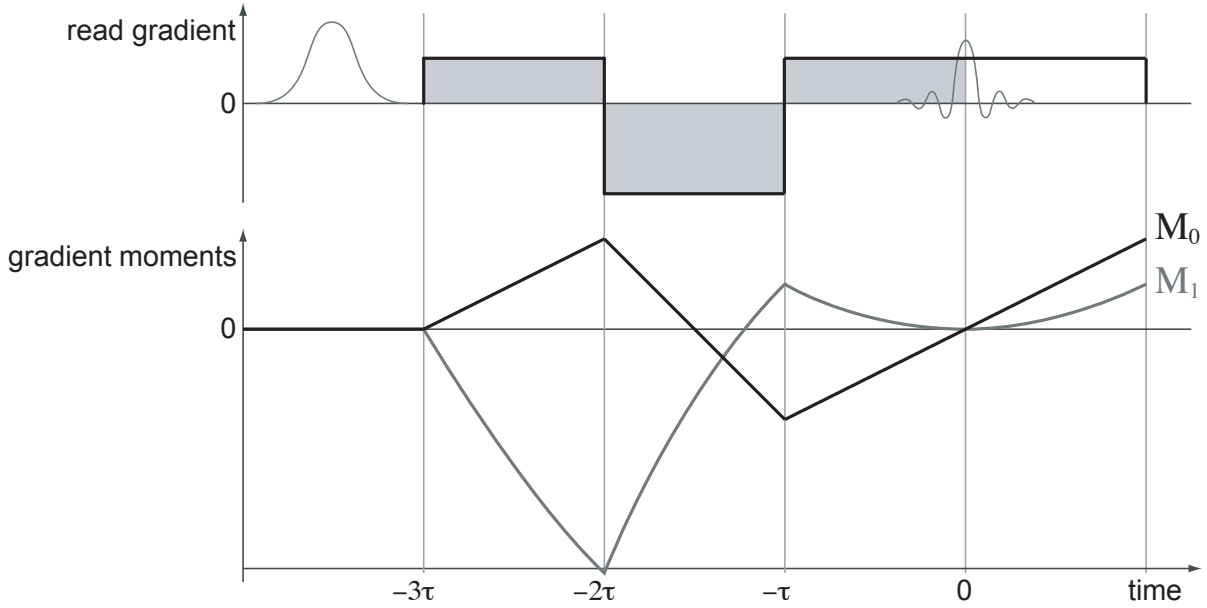


Figure 2.6: Motion compensated gradient switching scheme of the read encoding direction of a gradient echo experiment and the corresponding zeroth and first order gradient moments. At the echo time $t = 0$ both gradient moments are zero. Stationary and moving spins are rephased to form the echo.

Only two constraints must be considered for the switching scheme of the phase encoding gradient field in order to obtain motion compensation in the y -direction:

- The zeroth moment must have a specific, non-zero value C_i at the echo center. The value must change with every phase encoding step $k_{y,i}$ in order to achieve the spatial encoding (see Eq.2.22).

$$M_{0,i}(0) = \int_{-\infty}^0 dt G_{p,i}(t) = C_i \quad (2.52)$$

- For every phase encoding step the first gradient moment shall be zero at the center of the echo to rephase the moving spins.

$$M_{1,i}(0) = \int_{-\infty}^0 dt t G_{p,i}(t) = 0 \quad (2.53)$$

A gradient switching scheme with two degrees of freedom, i.e. a phase encoding gradient with two lobes, can provide a general solution to the two constraints. With motion compensation there is no motion-induced phase contribution at the echo center. Thus the misregistration artifact and intra-voxel dephasing are eliminated.

2.1.4.3 Motion Encoding

Motion encoding, or more precisely phase velocity encoding, uses the fact that part of the signal phase is induced by motion of the spins. The relation between velocity and its entailed phase contribution can be identified in Eq.2.34.

$$\phi_v = -\gamma M_1 v \quad (2.54)$$

The average velocity within a voxel can be calculated from ϕ_v and M_1 . The procedure of phase velocity encoding is very similar to motion compensation, with the exception that M_1 must be set to a non-zero value at the echo center in order to obtain a velocity dependent phase value.

The phase of complex MR signal is unequivocal in the range of $-\pi < \phi < \pi$ only. Therefore, velocity encoding can assign unambiguous velocities in the window $-1/2v_{max} < v < 1/2v_{max}$. Phase values accumulated due to velocities outside that velocity window are folded back into the unequivocal range. The effect is called `phase wrapping`. In order to avoid it, the magnitude of M_1 must be predetermined by the expected velocities within the sample:

$$M_{1,max} = \frac{\pi}{\gamma v_{max}}. \quad (2.55)$$

The accumulated phase shall utilize the complete phase range from $-\pi$ to π to minimize measurement errors. The signal to noise ratio of the phase map[‡] SNR_ϕ is proportional to the accumulated phase and the SNR_{mag} of the magnitude image [37].

$$SNR_\phi = \phi \cdot SNR_{mag} \quad (2.56)$$

The gradient switching scheme that produces the desired M_1 can be determined using the Eqs.2.48 to 2.53.

The phase is a scalar value whereas the velocity is a vectorial parameter. Thus, only the velocity component in one spatial dimension can be determined by one single phase velocity encoding experiment where the first gradient moments of the other dimensions must be set to zero at the echo center.

Only if the velocity is uniquely dedicated to the phase, a velocity component could be determined by one motion encoded experiment. In practice, phase effects of RF pulses

[‡]The recorded MRI data is complex. A phase map is generated when the arguments of the complex data are displayed as a grey scale image. To produce the regular image, the magnitude of the complex data is mapped.

and of field inhomogeneities also affect the signal phase so that a direct attribution of phase and velocity is not possible. Since the erroneous phase effects are systematic in every acquisition, they can be eliminated when two phase recordings with different first moments are subtracted. Then the velocity is given by:

$$\Delta\phi_v = -\gamma \Delta M_1 v. \quad (2.57)$$

To record velocities in three dimensions six experiments would be necessary if this procedure were applied independently to each dimension. A more advanced procedure is called four-point velocity vector extraction [37]. By using a certain linear combination of the Gradient moments only four experiments have to be recorded to obtain a velocity in three dimensions.

The influence of errors in the phase can be further minimized when a series of phase maps is recorded in which every phase map is recorded with a different gradient moment. Thereupon, for every voxel the recorded phase values can be plotted against their associated gradient moments. The slope of a linear regression line fitted to the data yields the velocity.

$$\gamma v = \frac{\Delta\phi}{\Delta M_1} \quad (2.58)$$

The above method of velocity determination is called the `phase difference method`.

Instead of only considering the phase information, the complete complex signals, i.e. magnitudes and arguments, are subtracted to perform phase contrast (PC) imaging. PC imaging is mainly used in angiography where the contrast of blood shall be enhanced over that of static tissue. PC imaging is unsuitable for the determination of velocities because the difference of the arguments of complex numbers is different to the argument resulting from complex subtraction.

2.1.4.4 Artifacts Not Eliminated by Motion Compensation

The `displacement artifact` caused by motion that is non-perpendicular to the imaging slice could not be eliminated by motion compensated gradient switching schemes. Other artifacts result when motion compensation and velocity encoding are implemented for constant velocities only. In practice, changes in velocity can occur and generate additional artifacts. Higher orders of motion generate a non-vanishing phase accumulation at the echo center which invalidates the attribution of velocity and phase.

The phase effects of `higher orders of motion` can be eliminated by the addition of motion compensating gradient lobes. An extra gradient lobe is needed

for every higher order of motion that shall be compensated. Therefore, the compensation of higher orders of motion extends the echo time and propels the phase effects of higher moments that were not compensated. For a gradient switching scheme as in Fig.2.6, the relation of a phase contribution due to acceleration and the phase due to constant velocity can be estimated by the following equation [56]:

$$\frac{\Delta\phi_a}{\Delta\phi_v} = \frac{a}{v}\tau, \quad (2.59)$$

where τ is the duration of a gradient lobe, in this work approximately 0.5 ms. Generally, the systolic flow velocity in the murine aorta does not exceed 1.2 m/s. This value is approached at the earliest 15 ms after the onset of the systole. A maximum acceleration of 80 m/s² is assumed. The expected phase contribution due to acceleration should be below 4% of the velocity-induced phase. Therefore, motion of orders higher than one were not compensated in this work. The short echo time was preferred for the following reasons.

Acquisition of the k -space lines of an image during different states of heart or breathing motion will cause ghost artifacts in the image [57]. A heart triggering of the data acquisition in combination with short acquisition or echo times allows for the reduction of ghost artifacts because every k -space line is acquired during the same motional phase. When necessary, breath gating can be implemented to inhibit data acquisition during breathing motion.

Turbulent blood flow generates very high orders of motion that cause phase shifts, intra-voxel dephasing, and ghost artifacts. Turbulence occurs randomly. Its effects cannot be eliminated by triggering; and higher order motion compensation is impractical. The only possibility to reduce the effects is a minimization of the echo time.

According to the Faraday-Henry law the rapid switching of magnetic gradient fields produces eddy currents in surrounding materials. The eddy currents generate magnetic fields that alter the magnetic gradient fields. The alteration of the gradient fields causes erroneous phase offsets in the detected MR signals that are proportional to the strengths of the local magnetic gradient fields. In phase velocity encoding, these phase offsets produce offsets in the measured flow velocities. The velocity offsets depend on the location of measurement and on the gradient field strength and are reproducible. The consequences of eddy currents can be minimized, but not eliminated, by the use of actively shielded gradient systems.

Velocity and position can be encoded simultaneously in a three-lobed gradient switching scheme for the read and slice directions, and a two-lobed scheme for the phase direction. The other option is to separate velocity encoding and velocity compensated spatial encoding. Velocity encoding by bipolar gradients leading

the spatial encoding was suggested by Moran in 1982 [58] and applied by van Dijk and Bryant two years later [59, 60]. Bipolar gradients have equal areas under the positive and negative gradient lobes. Their zeroth order gradient moment always is zero and the first order gradient moment is non-vanishing.

Velocity encoding with bipolar gradients is less prone to eddy currents due to the high symmetry of the switching scheme. A disadvantage is the extended echo time that aggravates the displacement artifact and artifacts due to acceleration and higher motional moments. In this work a short echo time was indispensable. Therefore, gradient switching schemes that encode velocity and position simultaneously were applied in this work.

In two-dimensional vascular imaging, blood does normally flow through the imaging slice. This causes the `inflow effect` that is applied in the time-of-flight method. In FLASH imaging of stationary samples, the magnetization reaches a steady state after a few RF pulses. When inflow is present, it disturbs the steady state. Depending on the flow velocity, two effects are prominent.

When blood flow is slow enough, most of the spins do not leave the imaging slice and they can be refocussed to form the signal echo. Additionally, the inflow provides fresh longitudinal magnetization which leads to a signal increase. In this work this effect was utilized to enhance the contrast between flowing blood and stationary tissue. When the effect is undesirable, it can be diminished by a saturation pulse that reduces the longitudinal magnetization of inflowing blood before the RF-excitation [61]. In contrast to slow flowing blood, the flow velocity can be so high that spins leave the imaging slice and are not refocussed, thus no echo will be formed. This effect is used in black blood methods where signal from flowing blood is purposely suppressed.

`Susceptibility artifacts` result because biologic tissue contains only diamagnetic atoms that possess no net angular momentum. The static \mathbf{B}_0 field perturbs the electron orbits and thus induces local magnetic dipoles. The phenomenon is called diamagnetic susceptibility and is responsible for the chemical shift. The induced dipoles locally alter the \mathbf{B}_0 field and accelerate the transversal relaxation. Residual magnetic polarities are induced at the boundaries of tissues with different magnetic susceptibilities. The boundary polarities can cause extensive image distortions. These distortions increase with the \mathbf{B}_0 field strength and can be reduced by the use of maximized magnetic field gradients for spatial encoding [39].

2.2 Biological Principles

2.2.1 The Arterial System

A major task of the arterial system is to supply organs with blood that carries nutrients and oxygen. Not every artery transports oxygenated blood, exceptions are the umbilical and the pulmonary arteries. But every artery transports blood away from the heart towards the smaller arterioles and to the capillary bed where oxygen and nutrients are exchanged with the tissue. Equally important are the mechanical properties of the arteries. Larger arteries, as the aorta, are elastic and attenuate the systolic pressure pulses, whereby the heart and the distal vascular system are protected from over-stressing. This property of the aorta is called the windkessel effect, in the style of the pressurized tank (in German "Windkessel") that was used to stabilize the water flow of historic fire pumps.

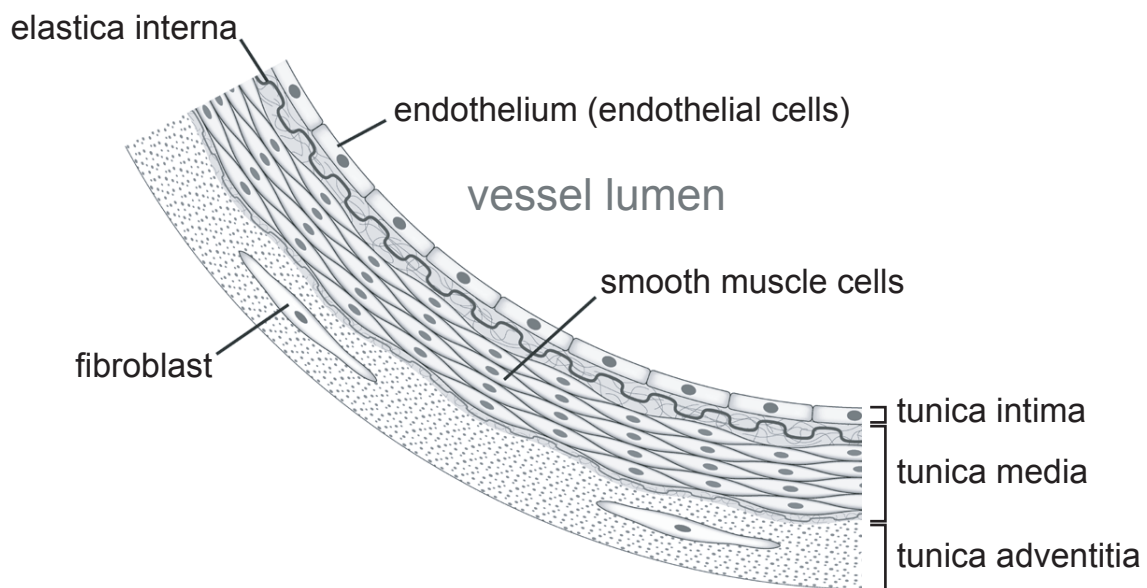


Figure 2.7: Anatomy of arteries. Image is an adapted version from Wikipedia commons.

Anatomically, arteries are structured in three functional, coaxial layers. The innermost layer that encloses the vessel lumen is the tunica intima. The intima consists of a layer of endothelial cells, the endothelium. Further outward adjoins the tunica media. The inner part of the media is formed by elastic connective tissue, the elastica interna; the other part is composed of smooth muscle cells. The outermost layer of an artery is the tunica externa, formerly known as the adventitia, which is formed by connective tissue.

The structure of the arterial wall shows that its composition is non-isotropic. It mainly

consists of elastin fibers, of collagen fibers that are almost inextensible, and of smooth muscle cells that can alter their tone due to neural mechanisms or circulating catecholamines. With increasing distance from the heart, the number of elastin laminae decreases and the number of muscular cells and the wall thickness increase. Therefore, the elasticity of the arteries decreases with increasing distance from the heart.

2.2.2 Atherosclerosis

Atherosclerosis is the major disease of large and medium sized arteries. In the course of the disease, endothelial dysfunction and inflammation of the vascular wall occur. The vessel stiffens and the arterial wall thickens as a result of incorporation of fatty materials into the endothelium and the tunica media (plaque formation). Vessel stiffening increases the load on the heart, causing diseases as hypertrophy and arrhythmia. For many years the plaque formation will not cause a reduction of the luminal cross section because the vessel expands to compensate the plaque growth. This is called positive remodeling. Positive remodeling may become uncontrolled so that an aneurysm is formed. Eventually vulnerable plaques may rupture and form clots that extend into the lumen. The clots will heal and may shrink, but generally they leave stenoses or even total closures of vessels. This causes insufficient blood supply of organs that depend on the artery. Another problem caused by the clots is thrombus formation due to disturbed blood flow. When a thrombus loosens from a clot and is washed away by the blood stream it may eventually get stuck in small vessels, cutting off the blood supply, whereupon the dependent part of tissue will die. When this happens in the brain or heart it is known as a stroke or cardiac infarction.

The processes of formation of atherosclerosis are not completely unraveled. Widely accepted is the `response to injury` hypothesis that was introduced by Ross and Glomset in 1973 [62] and assumes mechanical injuries of the endothelium to be the elicitor of atherosclerosis. These injuries can be caused by high blood pressure for example. A refined theory, the `lipoprotein induced hypothesis`, was presented by Brown and Goldstein in 1983 [63]. Low density lipoproteins (LDL) useful for the assembly of brain cells can be oxidized by free radicals. Oxidized LDLs cause defects in the endothelium. Monocytes (white blood cells) dock at these defects, transform to macrophages, and begin with phagocytosis of the oxidized LDLs. The macrophages can not remove the LDLs when there is a shortage of high density lipoproteins (HDL). The macrophages reside in the sub-endothelial region and turn into foam cells that store LDLs advancing plaque growth. Rupturing foam cells attract further monocytes. This closes a cycle that promotes plaque growth.

2.2.3 Hemodynamics

In fluid filled elastic tubes, pressure changes cause local movements of the fluid and of the vessel wall. The pressure and flow variations propagate along the elastic vessel in the form of a wave. The wave velocity is termed the pulse wave velocity (PWV) and depends amongst others on vascular elasticity. Parts of the wave are reflected when the impedance of the vessel changes. Impedance changes are caused, for example, by bifurcations.

Hemodynamics are a rather extensive subject area which is elaborately discussed in the dissertation by Volker Herold [64]. The following sections will only give a brief outline thereof, as far as the physical background is necessary to describe the later analytical methods of pulsatile flow in elastic vessels.

2.2.3.1 Empirical Hemodynamics

The relations between mechanical parameters of the vascular wall, the volume flow, blood pressure, and the PWV can be described by a simplified empirical approach. The vessel is modeled as an elastic, cylindrical tube. In 1920, Otto Frank et al. [65] developed an expression, known as Weber's equation, that describes the PWV:

$$c_0 = \sqrt{\frac{K}{\rho}}. \quad (2.60)$$

ρ is the fluid's density and K is the elastic modulus of volume distensibility per unit length of the arterial wall.

In order to understand equation 2.60, let the vessel be separated into two halves by a longitudinal plane of symmetry, as seen in Fig. 2.8. The tangential force onto the intraluminal cut surface is given by:

$$F_t = 2 \cdot R L p, \quad (2.61)$$

whereas p is intraluminal pressure. F_t is balanced by the force F_σ that results from the tangential wall stress σ_t .

$$F_\sigma = 2 \cdot h L \sigma_t \quad (2.62)$$

Equating Eq. 2.61 with Eq. 2.62 yields:

$$\sigma_t = \frac{p R}{h}, \quad (2.63)$$

and in differential form:

$$d\sigma_t = \frac{dp R}{h}. \quad (2.64)$$

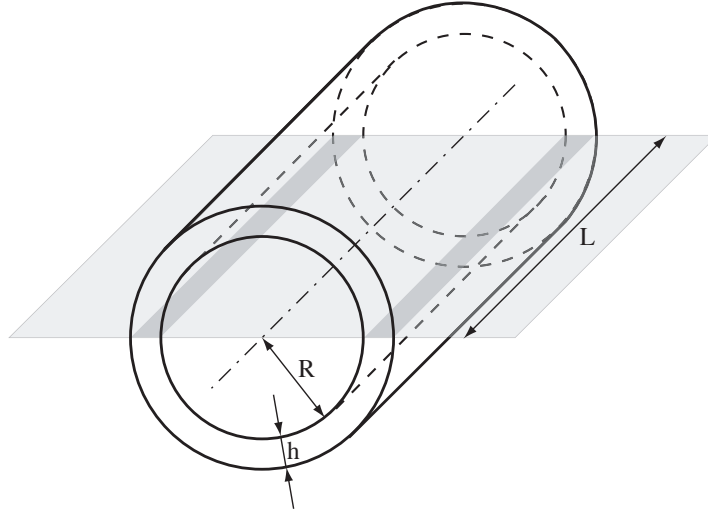


Figure 2.8: Vessel cut in halves by a longitudinal plane of symmetry. Illustration is an adapted version with kind permission from Volker Herold [64].

The elastic modulus of volume distensibility K can be derived from the elastic properties of the vascular wall:

$$K = \frac{dp}{dV/V} \stackrel{L \text{ const.}}{=} \frac{dp}{dA/A} = \frac{E_t \cdot h}{2R}. \quad (2.65)$$

E_t is the tangential elastic modulus, or Young's modulus of elasticity, that determines the relation between tangential wall stress σ_t and the relative change of the vascular circumference dl/l :

$$E_t = \frac{dp \cdot R^2}{dR \cdot h} \stackrel{\text{Eq. 2.64}}{=} \frac{d\sigma_t \cdot R}{dR} = \frac{d\sigma_t}{dl/l}. \quad (2.66)$$

Eq. 2.65 and Eq. 2.60 yield the Moens-Korteweg equation for the PWV in an elastic tube [66]:

$$c_0 = \sqrt{\frac{E_t h}{2\rho R}}. \quad (2.67)$$

The Moens-Korteweg equation delivers only an estimate of the PWV in arteries because it is based on several preconditions that apply to arteries with certain limitations:

- The wall thickness h can be neglected.
- Viscous effects of the fluid can be neglected.

- The fluid density is constant.
- The vessel wall is isotropically elastic and behaves according to Hooke's law; it is hookean.

In reality, the arterial wall is non-isotropic. It consists of elastin and collagen fibers with varying portions. The elastic modulus of collagen is approximately two orders of magnitude higher than that of elastin. Thus, the total elastic modulus is a nonlinear function of pressure and vessel distension. In humans, the elastic modulus of collagen becomes more determining at transmural pressures above 100 mmHg [12]. Therefore, the larger arteries are predominantly Hookean for pressures prevailing during the diastole and the early systole.

Stress-strain diagrams of arteries show hysteresis which identifies arteries to be visco-elastic [67]. The viscous component of the complex visco-elastic modulus contributes approximately 10% [68]. The wave propagation is subject to damping and the phase velocities of the pulse wave are frequency dependent. In humans, the phase velocities of the PWV approach a constant value above frequency components of 2 Hz [69]. A widely favored PWV measurement technique that mainly uses high frequency components of the pulse wave (i.e., it is frequency-independent) is the foot-to-foot method [5]. This method was applied in this work and is explained in section 2.2.4 on page 40.

2.2.3.2 Hemodynamics and the Navier-Stokes Equations

The empirical description of hemodynamics has its shortcomings. A more realistic approach to describe hemodynamics is based on the Navier-Stokes equations (Eqs. 2.68 ... 2.70) and the continuity equation (Eq. 2.71) [70]. The equations describe the physical interrelations of mass, momentum, and acceleration of infinitesimal fluid elements in elastic vessels. Blood vessels usually show cylindrical symmetry. Therefore, the cylindrical coordinates z, r, θ and the corresponding velocity components u, v, w are employed. ρ is the density of the fluid and μ is the viscosity.

$$\rho \left(\frac{\partial u}{\partial t} + u \frac{\partial u}{\partial z} + v \frac{\partial u}{\partial r} + \frac{w}{r} \frac{\partial u}{\partial \theta} \right) + \frac{\partial p}{\partial z} = \mu \left(\frac{\partial^2 u}{\partial z^2} + \frac{\partial^2 u}{\partial r^2} + \frac{1}{r} \frac{\partial u}{\partial r} + \frac{1}{r^2} \frac{\partial^2 u}{\partial \theta^2} \right) \quad (2.68)$$

$$\rho \left(\frac{\partial v}{\partial t} + u \frac{\partial v}{\partial z} + v \frac{\partial v}{\partial r} + \frac{w}{r} \frac{\partial v}{\partial \theta} - \frac{w^2}{r} \right) + \frac{\partial p}{\partial r} = \mu \left(\frac{\partial^2 v}{\partial z^2} + \frac{\partial^2 v}{\partial r^2} + \frac{1}{r} \frac{\partial v}{\partial r} - \frac{v}{r^2} + \frac{1}{r^2} \frac{\partial^2 v}{\partial \theta^2} - \frac{2}{r^2} \frac{\partial w}{\partial \theta} \right) \quad (2.69)$$

$$\rho \left(\frac{\partial w}{\partial t} + u \frac{\partial w}{\partial z} + v \frac{\partial w}{\partial r} + \frac{w}{r} \frac{\partial w}{\partial \theta} + \frac{vw}{r} \right) + \frac{1}{r} \frac{\partial p}{\partial \theta} =$$

$$\mu \left(\frac{\partial^2 w}{\partial z^2} + \frac{\partial^2 w}{\partial r^2} + \frac{1}{r} \frac{\partial w}{\partial r} - \frac{w}{r^2} + \frac{1}{r^2} \frac{\partial^2 w}{\partial \theta^2} - \frac{2}{r^2} \frac{\partial v}{\partial \theta} \right) \quad (2.70)$$

$$\frac{\partial u}{\partial t} + \frac{\partial v}{\partial r} + \frac{v}{r} + \frac{1}{r} \frac{\partial w}{\partial \theta} = 0 \quad (2.71)$$

These equations are valid under certain assumptions only:

- No external forces act upon the mass elements of fluid and vessel.

Gravitational forces can be neglected. In vivo, connective tissue may have effects on the vessel wall that are neglected in the following.

- The vessel wall is hookean.

For mice it is assumed that the vessel wall is hookean during the diastole and early systole.

- Mass is conserved, the vessel wall and the fluid are incompressible, the fluid density is constant.

The Poisson ratio (σ_P) is defined to assess the compressibility of materials. It is the ratio of radial strain to longitudinal strain. $\sigma_P = 0.5$ for incompressible materials. Blood and aortas ($\sigma_P = 0.48$) are considered to be incompressible [69].

- The fluid is Newtonian. For a Newtonian fluid the shear stress is equal to the product of the coefficient of viscosity and the radial velocity gradient.

Despite its corpuscular nature blood behaves like a Newtonian fluid in large arteries [69]. Blood shows non-Newtonian behavior in small vessels, such as the capillaries, where vessel diameters are comparable to the corpuscles.

- The no-slip boundary condition is assumed to hold true in the flow field and at the vessel wall. This means that there is no step change in the radial velocity gradient of the flow field.

In NMR, only velocities can be observed initially. In this work, the longitudinal flow velocities along the axis of the vessel (the z -direction) were of interest exclusively. Therefore the Navier-Stokes equations can be reduced to one dimension and their solutions can be simplified with the following assumptions which apply to larger arteries with certain constraints:

- The vessels have axial symmetry and run straight. This approximately holds in the carotids and the descending aorta but not so in the aortic arch.
- The vessel wall is very thin with respect to the vessel diameter ($k = h/R \ll 1$).
In the murine aorta, the wall is relatively thick for that approximation. The thickness is approximately one tenth of the vessel radius $k = 0.1$.
- The wave length (λ) is much larger than the vessel diameter (d), $d/\lambda \ll 1$. In mice with an approximate PWV of $c_0 = 3$ m/s and a heart period of 120 ms and a vessel diameter of 1 mm, the ratio is $d/\lambda = 2.8 \cdot 10^{-3}$.
- The PWV is much larger than the average flow velocity (\bar{u}), $\bar{u}/c_0 \ll 1$. $\bar{u}/c_0 \approx 0.14$ for mice with a heart stroke volume of $40 \mu\text{l}$. The precondition is not fulfilled in mice for the complete heart cycle. It holds for the diastolic and early systolic part of the wave.

A detailed derivation of the solutions for pressure and flow velocities can be found in [70]. Here only the results of importance for the following work will be given. The volume flow ($Q(z, t)$) for input pressures ($p(z, t)$) in the form of complex exponentials is given as:

$$p(z, t) = p_0 \exp(i\omega(t - z/c_0)), \quad (2.72)$$

$$Q(z, t) = Q_0 \exp(i\omega(t - z/c_0)) = Y_0 p_0 \exp(i\omega(t - z/c_0)), \quad (2.73)$$

with the characteristic admittance:

$$Y_0 = \frac{\pi R^2}{\rho c_0} \quad (2.74)$$

or rather the characteristic impedance:

$$Z_0 = \frac{1}{Y_0} = \frac{\rho c_0}{\pi R^2}. \quad (2.75)$$

c_0 is the PWV as it is given by Eq. 2.67, the Moens-Korteweg equation:

$$c_0 = \sqrt{\frac{Eh}{\rho 2R}}. \quad (2.76)$$

The simplifications that are applied in the one-dimensional solution of the Navier-Stokes equations neglect effects of the viscosity μ . To overcome this limitation, Womersley et al. developed the solutions for two-dimensional radial flow profiles [71]. Duan et al. simplified Womersley's two-dimensional problem to a one-dimensional problem that considers fluid viscosity [72]. The resulting PWV c turns out to be a complex parameter that shows

frequency dependence. Deviations between c and c_0 are shown in dependence of a dimensionless frequency parameter α for an exemplary murine aorta in Fig.2.9. $\alpha = R_0\sqrt{\omega\rho/\mu}$ is the Womersley parameter. It describes the proportion of motion that is dominated by viscous effects to motion that is dominated by inertial effects. Exemplary Womersley parameters for a murine aorta are listed in Tab.2.1.

harmonic	1-st	2-nd	3-rd	4-th	5-th	6-th	7-th	8-th	9-th	10-th
α	1.8	2.5	3.0	3.5	3.9	4.3	4.6	5.0	5.3	5.5

Table 2.1: Exemplary Womersley parameters of a murine aorta ($\rho = 1.055 \text{ g/cm}^3$, $R = 0.5 \text{ mm}$, $\mu = 4.5 \text{ mPa}$, $\omega = n 2\pi/\tau_{\text{heart}}$, $\tau_{\text{heart}} = 120 \text{ ms}$).

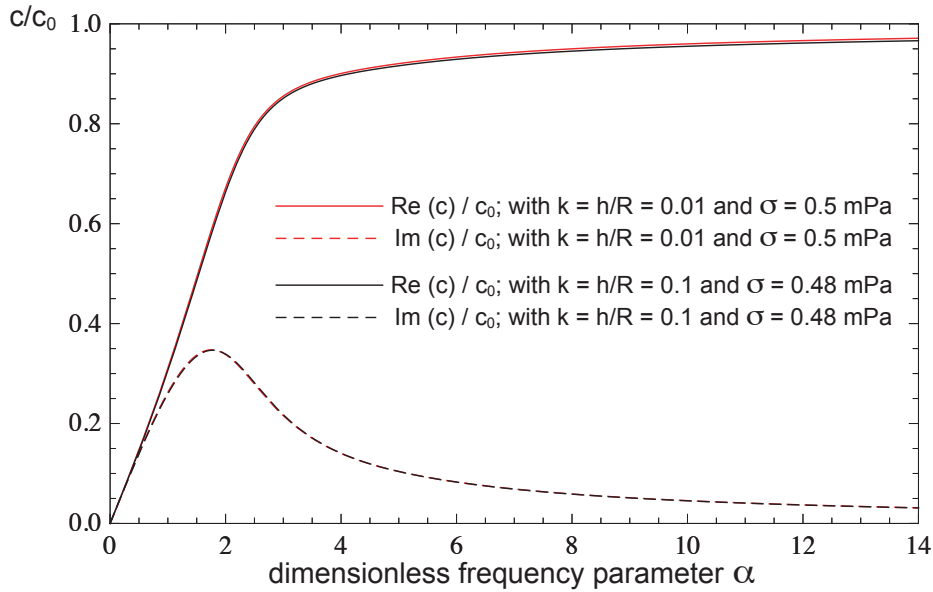


Figure 2.9: Dispersion of normalized pulse wave phase velocities. The red curves present the real and imaginary parts of the normalized PWV with fulfilled preconditions for Duan’s approximation to the solution of the Navier-Stokes equations. The black curves represent the normalized PWV of an exemplary murine aorta with a Poisson number $\sigma = 0.48$ (vessel wall is almost incompressible) and ratio of vessel wall to radius of 0.1 (thin-wall approximation is not fulfilled). Duan’s approximation delineates the murine aorta very well even though not all preconditions for this model are fulfilled in the mouse.

Fig. 2.9 shows that the non-compliance to the thin-wall approximation does not have a significant effect on c . Therefore, Duan’s one-dimensional solution of the Navier-Stokes

equations delivers a good approximation for hemodynamics in the murine aorta. Fig.2.9 and Tab.2.1 also show that the phase velocity of the fourth harmonic of the pulse wave deviates from c_0 by approximately 10%. For higher harmonics of the pulse wave, viscous effects can be neglected and the Moens-Korteweg-Equation provides a sufficient approximation of the PWV in the murine aorta.

2.2.3.3 Clinical Parameters Describing Hemodynamics

According to the Moens-Korteweg equation, the PWV depends on Young's modulus of elasticity E_t . Therefore, it can be used as a surrogate marker for vascular elasticity. Methods that determine the PWV are, for example, the transit time method (section 2.2.4 on page 40) or the QA method that uses the relation of volume flow Q (Eq. 2.73) to vessel cross-sectional area A (section 2.2.5 on page 42).

Other parameters that describe vascular elasticity are for example:

- The vascular distensibility D :

$$D = \frac{d_d}{\Delta p / \Delta d}. \quad (2.77)$$

Distensibility and PWV are related by the following expression:

$$D = \frac{\text{PWV}^2}{2\rho}. \quad (2.78)$$

The distensibility depends on the diastolic diameter d_d that can be altered by a variation of the diastolic pressure. In arteries the ratio $\Delta p / \Delta d$ is also pressure dependent.

- The compliance C :

$$C = \frac{\Delta d}{\Delta p} \quad (2.79)$$

or alternatively:

$$C = \frac{\Delta V}{\Delta p}. \quad (2.80)$$

Whereas the distensibility is based on relative changes in volume or diameter according to a pressure change, the arterial compliance is based on an absolute change in vascular diameter or volume over pressure. It also depends on diastolic pressure.

Besides the above mentioned markers of arterial elasticity there is a perplexing amount of measures that describe arterial elasticity which often are not even defined uniquely. A list can be found in [73]. Even though the PWV often is viewed as a surrogate for other markers of vascular elasticity, it still is probably the best measure of arterial stiffness because it can determine when pressure waves reflected by the periphery arrive at the heart and increase cardiac load. Another advantage is that it can be determined without the invasive measurements of intraluminal pressure. Intraluminal pressure measurements are necessary for the direct determination of the distensibility or the compliance and should be performed in the same location as the diameter or volume measurements. Because the PWV measurements can be performed without invasive intra-luminal pressure measurements, the PWV is the marker of choice in the following work.

2.2.4 The Transit Time Method to Determine the Regional PWV

A standard method to measure a regional average of the PWV in humans applies the transit time (TT) method. A major goal in this work was the transfer of an MRI TT method to mice. First rudimentary approaches in humans appraised the transit times of the pulse waves between two locations by palpation. Later, approaches applied manometry [9], arterial tonometry [10], Doppler ultrasound measurements of vessel wall motion [11], and Doppler ultrasound measurements of blood flow velocity [12]. Age related changes of the PWV, distensibility and morphology were discovered [10, 74]. Mohiaddin et al. used MRI to affirm the age related increase of the PWV in humans [13]. Today, MR methods assessing PWVs in humans have been refined by many workgroups [15, 16]; and they constitute a comprehensive technique for the characterization of morphologic and functional arterial systemic parameters.

The principle to measure arterial PWV with the TT method is as follows. As Fig.2.10 shows, at least two measurement sites, imaging slices I and II, are to be selected on the aorta at a mutual distance, Δx . The transit time, Δt , which the pulse needs to travel from location I to II is to be measured. The PWV is calculated as:

$$PWV = \frac{\Delta x}{\Delta t}. \quad (2.81)$$

This procedure is called the two-point TT method.

The generalization of the two-point TT method is the multi-point TT method. It measures the transit times of the pulse waves in multiple locations along the path of wave propagation. The larger the distances between the measurement locations, the longer are the transit times of the pulses (see Fig.3.5.b on page 55). The PWV is the constant

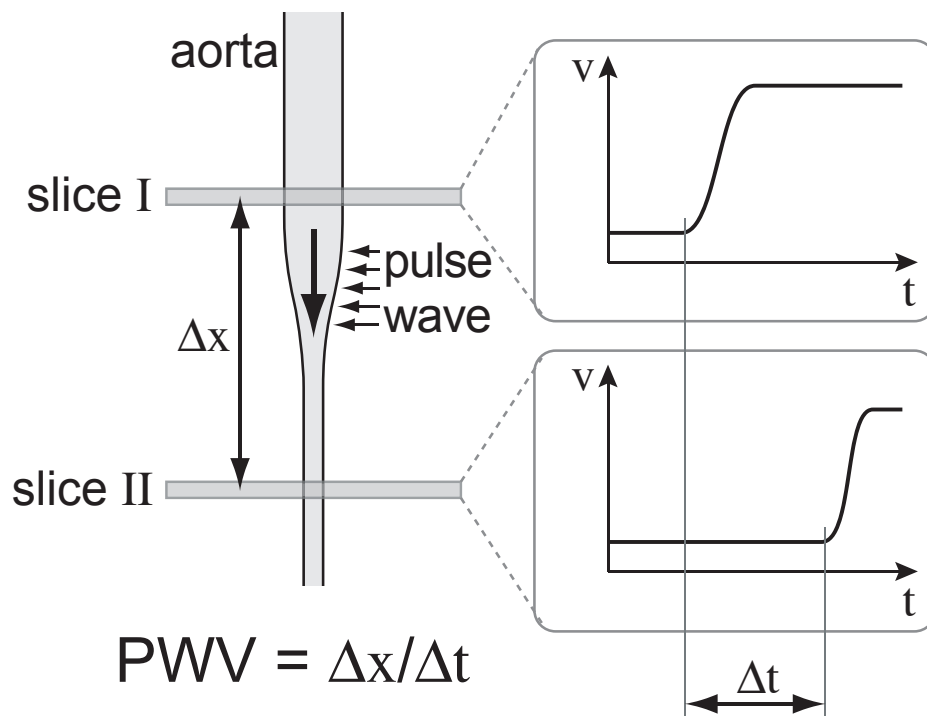


Figure 2.10: Two-point transit time (TT) method. The time courses of, e.g., arterial flow velocities are recorded at two measurement positions. The pulse wave velocity (PWV) is the ratio of the distance between the measurement locations and the transit time of the pulse wave.

of proportionality between the distances and the corresponding transit times. The TT method delivers a regional PWV averaged over the measurement range.

Fig.3.5.a,b, and Fig.4.5.b on the pages 55 and 71 present pressure and flow curves recorded on a vessel phantom and on mice. They reveal that flow and pressure pulse curves show a gradual rather than an instantaneous increase. However, a distinctive feature of the pulse shape is necessary to determine the transit time. In order to generate a distinctive feature, an abstract pulse onset time was appointed to every pulse curve. The abstract onset time of the pulse was defined as the intersection point of a line fitted to the velocity or pressure values before the pulse, i.e. the pressure baseline, and another line fitted to the early increasing values. This method is called the foot-to-foot method. Its advantage is that it uses high order harmonics of the flow or pressure curve for which the phase velocities do not show significant amounts of dispersion.

The two-point TT method was applied for all MR measurements of the PWV in this

work, i.e. on mice and on the pulsatile, elastic vessel phantom. The multi-point TT method was used for the reference measurements which acquired the pressure waves on the vessel phantom.

2.2.5 The QA Method to Determine the Local PWV

The PWV of an artery can be estimated locally from the relation of the change in flow (dQ) and the change in luminal area (dA) during the early part of the systole under the precondition that the pulse wave is reflection-free. The precondition is fulfilled for humans [75, 69] and ultrasonic studies [76, 32, 34] indicate that it applies for mice, too.

High frequency components of the pulse wave prevail during the early part of the systolic pulse wave and viscosity effects can be neglected in the description by the Navier-Stokes equations. The frequency dependent vascular impedance can be approximated by the characteristic impedance Z_0 that is obtained from the one-dimensional solution of the Navier-Stokes equations (Eq. 2.75):

$$Z_0 = \frac{\rho c_0}{A}. \quad (2.82)$$

The characteristic impedance can also be determined in the time domain by measurements of pressure (p) and volume flow (Q) during the reflection free part of the systole [77]:

$$Z_0 = \frac{dp}{dQ}. \quad (2.83)$$

With the local area compliance of the vessel, $C_A = dA/dp$, follows:

$$Z_0 = \frac{dp}{dA} \frac{dA}{dQ} = \frac{1}{C_A} \frac{dA}{dQ}. \quad (2.84)$$

A relation for the pressure and the cross-sectional area follows from the definition of Young's modulus (Eq. 2.66) and the Moens-Korteweg equation (Eq. 2.67):

$$\frac{dp}{dA} = \frac{c_0^2 \rho}{A} = \frac{1}{C_A}. \quad (2.85)$$

With this and the previous equation, the characteristic impedance can be written as:

$$Z_0 = \frac{c_0^2 \rho}{A} \frac{dA}{dQ}. \quad (2.86)$$

Equating the two definitions of the characteristic impedance (Eqs. 2.82 & 2.86) yields the PWV as the ratio of changes in volume flow and cross-sectional area:

$$c_0 = \frac{dQ}{dA}. \quad (2.87)$$

This is the basis of the QA method that allows the local measurement of the PWV. It was introduced as a diagnostic MR method on humans by Vulliemoz et al. in 2002 [16]. In this work, the QA method was transferred to mice to determine local PWVs in the descending aorta.

2.3 Animals & Experimental Equipment

2.3.1 ApoE^(-/-) Mice

Today the mouse is an indispensable animal model for the study of atherosclerosis and its risk factors. Conveniences of mice are their short generation times and the relatively low costs for animal housing. The mouse is the only mammal whose genome is completely characterized. Its genetic material is concordant with the human genome to 97% [78]. Techniques exist that allow for an increased expression of genes, or the modification and deletion of the genes themselves. With these methods animal models that exhibit genetic variations relevant to lipoprotein metabolism and atherosclerosis were generated [79, 24].

A transgenic mouse model that is deficient in apolipoprotein E is the ApoE^(-/-) mouse. It is prominent in the study of atherosclerosis. ApoE^(-/-) mice provide insight into the vascular biology of atherogenesis and vascular dysfunction. These mice spontaneously develop severe hyperlipidemia and atheromatous lesions at the arterial wall [22]. The lesions have distribution patterns, structures, and compositions, which resemble human lesions throughout the course of the disease [23].

Ultrasound and pressure catheter measurements were utilized to characterize functional parameters of the murine arterial system. Hartley et al. presented a Doppler ultrasound TT method to measure PWV in living, transgenic mice non-invasively [30]. Wang et al. found that the PWV is significantly increased in ApoE^(-/-) mice compared to wild type mice for ages 13 months and older [31]. PWV, vascular input impedance, and augmentation index also increase with age [32].

2.3.2 The Magnetic Resonance Tomograph

The MR system that was used for the measurements was a Bruker AVANCE 750 spectrometer (Bruker Biospin, Rheinstetten, Germany) with a vertical main magnetic field of 17.6 T and a bore size of 89 mm. The self-shielded gradient insert, a Bruker Micro 2.5, had a maximum gradient strength of 993 mT/m and an inner diameter of 40 mm. An external tempering unit controlled the temperature of the gradient system. The tempering unit was applied to maintain a temperature of 37°C within the gradient system during in vivo experiments. The transversal electromagnetic mode radio frequency resonator built by Daniel Gareis [80] had an accessible inner diameter of 25 mm. The diameter allowed for measurements of mice with a body mass below 35 g. The limited space within the resonator prevented the use of an animal positioning system. The mice were affixed inside the resonator by means of a tape flap attached to the front legs.

2.3.3 Heart Triggering & Breath Gating

The setup that was used for heart triggering / breath gating is illustrated in Fig.2.11. A pressure sensitive pneumatic balloon (Graseby Medical Limited, Watford, United Kingdom) was placed between the inner RF resonator wall and thoraces of mice to detect cardiac trigger and respiratory gating signals. Outside of the gradient insert a pressure transducer (24PCEFA6D, Honeywell S&C, Golden Valley, MN, USA) transformed the pressure signal from the balloon into an electrical signal that was amplified and processed in real-time by a triggering unit that was homebuilt by Dr. Eberhard Rommel at this department [81]. Thus electrical interference between the trigger signal and gradient fields oscillating in the same frequency domain was avoided.

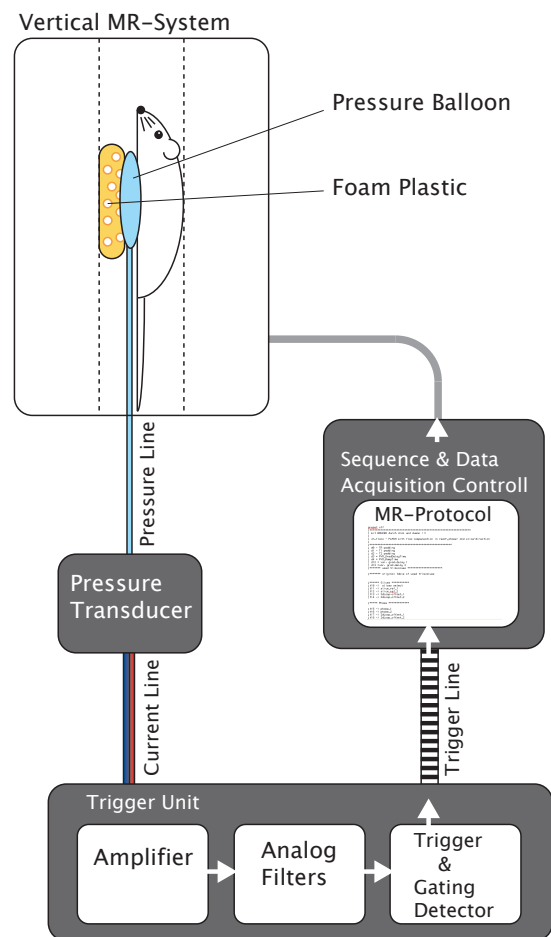


Figure 2.11: Setup used for heart triggering / breath gating the MR data acquisition. The pneumatic tap of the heart signals avoids electrical interference with switching magnetic gradient fields.

The trigger signal from the pneumatic pressure balloon represented mechanical motion of the thorax and the heart. To locate the onset time of systolic blood flow, a time resolved 2D FLASH sequence without motion compensation was applied. The systolic blood flow was identified by intra-voxel dephasing artifacts. An appropriate temporal

delay was inserted between the heart trigger signals and the initiations of data acquisition so that flow velocities were recorded in the late diastolic and early systolic parts of the heart cycle. The trigger unit averages previous respiratory timings and predicts the one to follow. In this way a high-quality respiratory gating is achieved. However, irregular respiration could vitiate the prediction of the respiratory gating signal in some cases. If so, the onset of respiratory motion gated the data acquisition directly.

The high quality of the heart trigger signals is of vital importance for the outcome of the measurements. Therefore, the pneumatic balloon was attached to another tape flap which also extended to the exterior of the resonator. This allowed for a precise placement of the balloon in between resonator wall and mouse. The optimum position of the balloon was reached when the amplitude of the pressure curve on the display of the heart triggering unit was maximal.

Chapter 3

The Pulsatile Elastic Vessel Phantom

In this work, MR methods to assess the PWVs of the descending murine aorta were developed. The validity of these measurement techniques was analyzed under standardized conditions on a pulsatile elastic vessel phantom. An elastic phantom vessel and a flow pulse generator were developed for this purpose. The phantom allowed for the determination of flow velocity waves and vessel cross sections using the developed MR methods. The phantom also allowed for measurements of pressure waves utilizing a pressure catheter. The resulting PWVs of the pressure measurements were assigned as the standard. The PWVs obtained by MR measurements were compared in order to give evidence of the accuracy of the MR methods. Three different MR-Methods were developed and tested:

- A TT method that analyzes the transit of the flow pulse waveforms,
- a TT method that analyzes the transit of cross-sectional luminal area distension, i.e. distension waveforms,
- and a QA method that analyzes the relation of local volume flow and cross-sectional luminal areas.

Elastic phantom vessels that shall be used to test the quality of methods measuring vascular systemic parameters must have appropriate physical properties. Such as: mechanical strength, uniformity, long-term stability, and a modulus of elasticity resembling animal tissue. In this work different construction materials were tested.

Agar and latex proved to be not suitable. The findings accord with literature. Simple hydrogels as gelatin [82], agar [83], agarose [84], and polysaccharides [85] were used for MR quality control phantoms in the past but they have poor breaking strengths. It was found that thin-walled latex tubes disintegrate after a few days and their PWVs exceed physiological values by a factor of 10. Literature states that flexible materials as

latex rubber and silicones have elastic moduli ranging from 10 to 100 MPa which are not physiologic. Excised rat aortas were tested for suitability as vessel phantoms and proved to be not manageable in experiment. They broke when they were affixed to the mounting support or pressurized. In addition they decomposed.

The material that proved appropriate is poly(vinyl alcohol) cryogel (PVA-C). It has high breaking strengths and physiologic elastic moduli ranging from 0.1 to 1.0 MPa [86]. Peppas et al. and Nambu et al. independently discovered that a gel is formed due to the crystalline behavior of aqueous solutions of poly(vinyl alcohol) upon freezing and thawing [87, 88]. The elastic modulus depends amongst others on the number of freeze-thaw cycles, the concentration of the aqueous solution, and essentially on the thaw rate [86, 89].

The properties of the pulsatile elastic vessel phantom and of several manufactured PVA-C vessels are presented in this chapter. The comparison of the MR and pressure measurements of the PWVs will be given in the chapters of the measurement methods (chapters 4, 5, 6).

3.1 Methods

3.1.1 Fabrication of the Phantom Vessel

A process to manufacture the phantom vessels was developed. PVA granules (MowiolTM20-98, Sigma-Aldrich Chemie GmbH, Steinheim, Germany) were dissolved in demineralized water at 100°C using a boiling water bath on a magnetic stirrer. The granules dissolved in approximately 30 to 60 min. A hydrogel of 15% w/w PVA was produced. It was stored in a sealed container at room temperature for at least 24 hours to allow air bubbles to rise to the surface. Bubble free PVA hydrogel was extracted from below the surface with the aid of a syringe and was then injected into a mold made of acrylic glass. The mold was flushed with PVA hydrogel until it was free of any air bubbles.

The mold was designed to produce a PVA-C tube with an inner diameter of 6 mm, a wall thickness of 0.25 mm, and a length of 8 cm. Assumed the produced PVA-C had an elastic modulus of approximately 0.1 to 1.0 MPa and according to Eq.2.67, the Moens-Korteweg equation [90], the PWV of the tube should have been in the range of 2.0 to 6.5 m/s*.

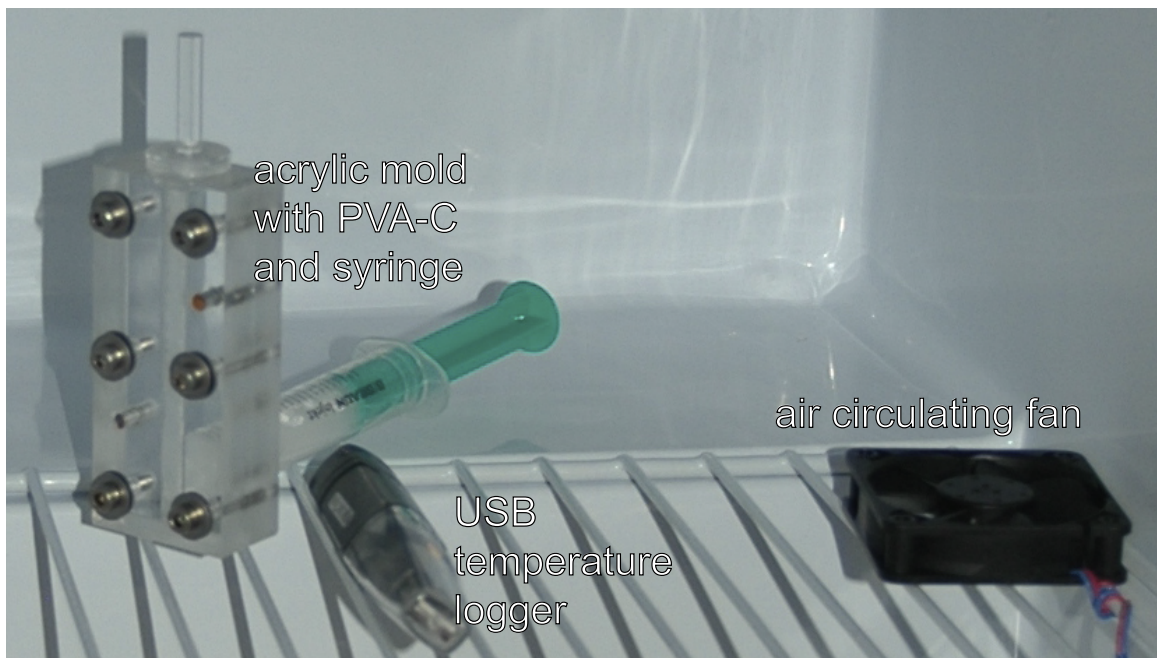


Figure 3.1: Equipment used to fabricate the PVA-C vessel inside the freezer.

*The density of water was used for the estimation.

To cross-link the PVA solution it had to undergo repeated freeze-thaw cycles. A commercial freezer connected to a clock timer was used to repeatedly freeze and thaw the mold with the PVA. An air-circulating fan with a power of 1 W was used to homogenize the temperature distribution inside the freezer. The temperatures inside the freezer were recorded every minute by a USB temperature logger (Voltcraft DL-100T, Conrad Electronic SE, Hirschau, Germany) to control the correct run of the cross-linking process. The mold was cooled down from 24°C to -37°C in 1.7 hours and kept at that temperature for another 10.3 hours. Thereafter the freezer was turned off for 12 hours to warm up to 24°C by heat conducted through the freezers insulation plus heat produced by the air circulating fan. The warming rate was 0.2°C/min between -10°C and 0°C, between 0°C and 10°C it was 0.1°C/min. The vessel phantoms underwent five to 14 freeze-thaw cycles. PVA-C proved to be non-sticky to acrylic glass which allowed for an unproblematic removal of the fabricated vessel from the mold.

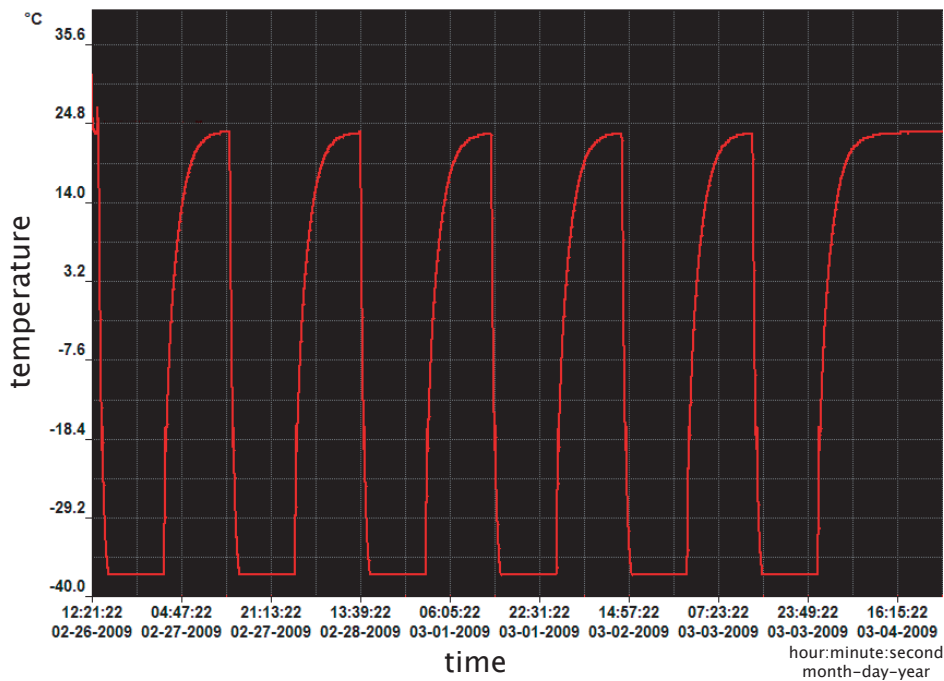


Figure 3.2: Temperature log of the freeze-thaw cycles of the phantom vessel.

After the freeze-thawing cycles, PVA-C is subject to an aging process due to further crystallization that can affect its elasticity [89]. Therefore the tube was stored in a water bath at room temperature to stabilize for at least 14 days after it had been removed from the mold.

3.1.2 Experimental Setup of the Vessel Phantom

The PVA-C vessel was affixed in a homemade mounting suspension (see Fig.3.3). A water reservoir was connected to the outgoing end of the vessel. A catheter to measure the time responses of intra-luminal pressure in different positions could be inserted into the outlet end of the vessel through the mounting suspension. Pressure and flow pulses were generated by a homemade pulse generator (Fig.3.4) and were fed to the intake side of the PVA-C vessel. The pulse generator was located outside the strong magnetic field of the MR-system and was driven by a function generator (F34, Interstate Electronics Corporation, Anaheim, CA, USA) in order to produce periodical pulses. The function generator also triggered the data acquisitions of the MR system and of the setup that was used to record the pressure waves inside the PVA-C vessel.

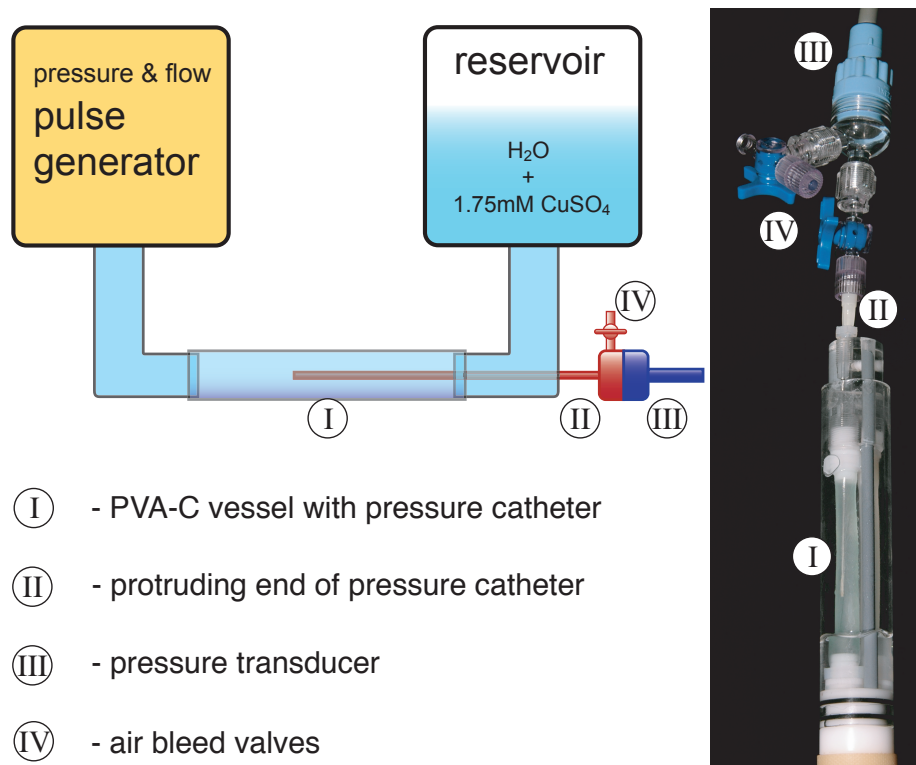


Figure 3.3: Simplified scheme and photograph of the elastic vessel phantom used to investigate the accuracy of the MR TT method.

The setup to record pressure waves comprised a pressure catheter, a signal amplifier, and a storage oscilloscope. The catheter was inserted into the outlet end of the vessel. In order to limit the effects of the catheter on the PWV of the vessel, the diameter of the

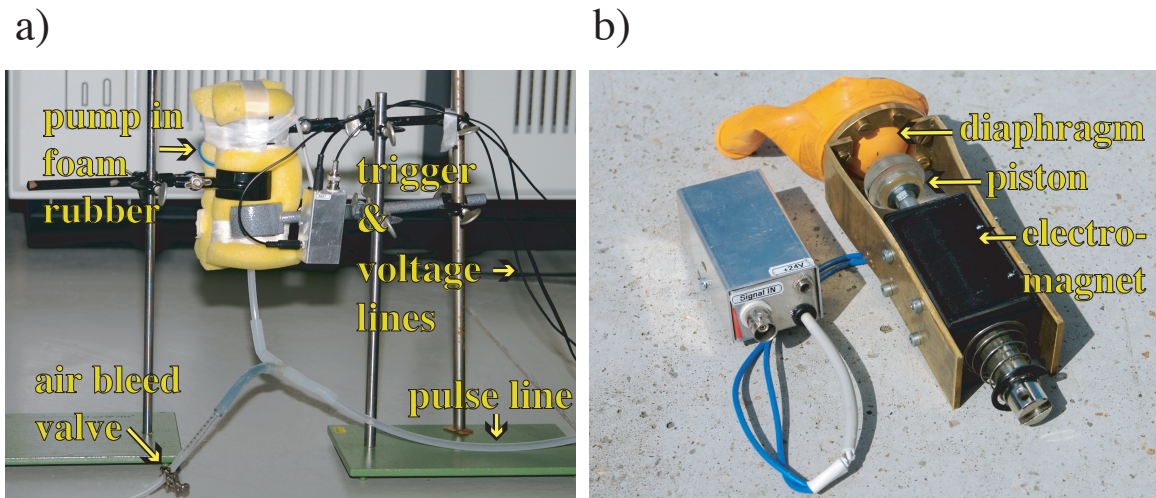


Figure 3.4: Images of the pulse generator. In image **a** the pulse generator is shown in operational configuration. The foam rubber padding encloses it for shock absorption. In image **b** the diaphragm pump is dismantled so that the diaphragm (an air balloon), the piston and the electric magnet are visible. The outlet connector of the pump is hidden behind the balloon.

catheter is one seventh of the pressurized vessel diameter. The measurement positions of the pressure catheter were determined at its protruding end with a caliper gauge. The catheter was compounded of a blunted stainless steel canula (TSK-Supra, Ebhardt-Söhne GmbH, Geislingen, Germany) and a Statham P23XL pressure transducer (Viggo-Spectramed, Inc., Oxnard, CA, USA). The canula has a diameter of 1 mm and a length of 100 mm. The signal amplifier was an MBS STAT ZAK (ZAK Psychologische und Physiologische Instrumente GmbH, Simbach, Germany). The storage oscilloscope was a TDS 3032 (Tektronix Inc., Beaverton, OR, USA).

The outlet end of the vessel was connected to a reservoir filled with an aqueous solution of 1.75 mM CuSO_4 . The height of the reservoir was adjusted to set the static pressure in the vessel in order that it did not collapse or bloat excessively. The hydrostatic head above the middle of the vessel was approximately 15 cm. The cross-sectional magnitude images of the MR flow measurements showed that the pressurized PVA-C vessel had a minimum inner diameter of 7 mm. Two plastic rods supported the vessel on one side to prevent it from swinging in the transversal direction but allowing it to expand during the transit of the pulse.

Stronger pressure and flow pulses frequently caused pressure oscillations in the vessel phantom with a frequency of approximately 100 Hz. These oscillations corrupted or deteriorated the pressure measurements. This increased the uncertainty in the determined

pressure wave velocity when stronger pressure pulses were used. Fixing the vessel could not reduce these oscillations unless it was tethered indefensibly. Reduction of the pulse pressure, accompanied by a lower maximum flow velocity, greatly reduced these oscillations but did not eliminate them. The search for remaining sources uncovered impact noise of the ground floor. During some measurements the impact noise was not present at all. During others, it was predominant over the pulse wave. The disturbances were, for example, generated by people walking in the spectrometer control room, the magnet room, or by an occasionally active air compressor mounted in the story above the magnet room. The whole vessel phantom was thereafter mounted on a wooden board loaded with 20 kg of lead bricks. The board rested on a foam rubber mattress. This successfully eliminated impact noise from the floor.

The through-slice flow velocity curves that were acquired by the MR method were free of the 100 Hz oscillations. This indicates that there is no longitudinal velocity component to the oscillations. The oscillations are assumed to be transversal vibrations of the vessel wall initiated by pressure pulses or external disturbances. The same type of oscillations also had been observed on elastic vessel phantoms by Dineley et al. [91].

3.1.3 Performance Tests on the Vessel Phantom

Before the vessel phantom was used to validate the MR method, it was tested to determine how unsusceptible the pressure pulse wave is to vessel age, temperature changes, static pressure offsets, and the pressure pulse period and amplitude. For each PWV measurement, pressure time courses were recorded at on average 13 different measurement positions to evaluate the PWV using the multi-point TT method. The minimum number of pressure measurement locations was 10. The pressure data was analyzed in MATLAB to determine the onset times of the pressure waves for each measurement position of the pressure catheter. The measurement positions were plotted versus the corresponding pressure pulse onset times; the slope of the linear regression yielded the PWV. Representative records of pressure time courses and a position vs. time plot are shown in Fig.3.5.

The test for a dependence of the PWV on vessel age was performed over a time span of 64 days starting 14 days after the completion of the controlled cross-linking. Literature states that the aging process ends approximately 10 days after the cross-linking by freeze-thaw cycles [89].

The dependence of the PWV on the static pressure was analyzed because deviations in the installation height of the vessel phantom will cause changes in the static intra-luminal pressure which may affect the PWV. For the test, a variation in height of 25 mm was

considered sufficient to describe the PWV dependence because the uncertainty in vessel phantom position inside the MR magnet is only ± 1 mm.

The PWV's susceptibility to temperature changes in the range of 16 to 29°C was tested because the precision of the temperature control within the magnet is limited. During MR experiments the observed temperature deviation between the gradient system and room temperature ($\vartheta_{room} = 16^\circ\text{C}$) was below $+1^\circ\text{C}$. The temperature of the phantom was not measurable, e.g., by using thermocouples, due to the switching of strong magnetic gradient fields. Optical temperature measurements were prevented, because the phantom vessel was not visible after installation inside the magnet. Due to the close contact of vessel phantom, RF resonator, and gradient insert it was assumed that the temperature of the phantom should deviate from the gradient insert temperature by less than two degrees. For the test measurements, the vessel phantom was placed in the air stream of a heat gun to temper the vessel and the fluid. The temperature was measured with an infrared thermometer (Thermo-Hunter BA-30TV, Optex Co. LTD, Shiga, Japan).

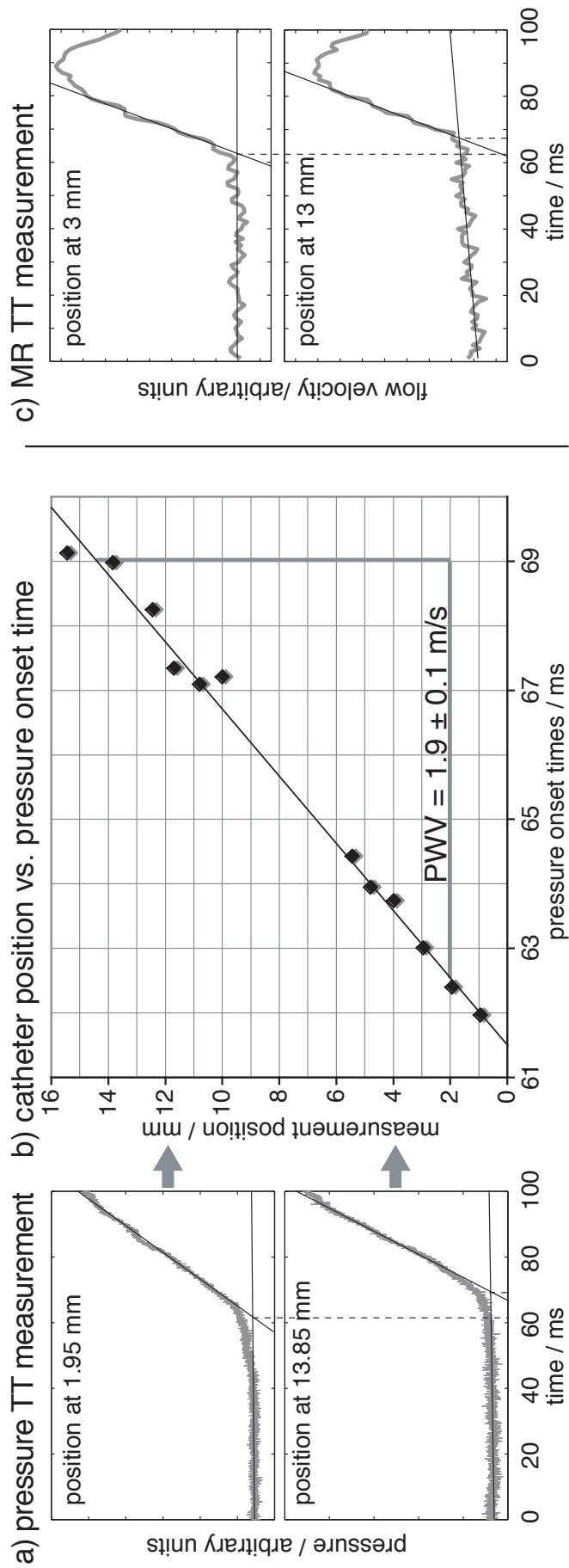


Figure 3.5: Representative pressure and flow PWV measurements on the phantom vessel. **a)** Two representative time courses of the pressure wave measured in the phantom vessel (sampling rate = 100 ms^{-1}). **b)** Transit of the pressure wave as it was acquired by the multi-point TT method. The pressure onset time is defined by the foot of the pressure wave. The measurement position indicates the location of the pressure catheter. For easier exemplification the independent parameter, the pressure onset time is exceptionally assigned to the abscissa. Therefore, the slope of the linear regression line determines the PWV. The $PWV = 1.9 \pm 0.1 \text{ m/s}$ is given as mean \pm standard error (SE). **c)** Representative flow velocity time courses in the phantom vessel measured with the MR protocol.

3.2 Results

The PVA-C vessels proved to be mechanically relatively stable. With some user experience, they can be handled well. However, they are not unbreakable, and therefore, data of several vessels is presented in the following. The PWV of the phantom vessel showed no dependence on age or pressure pulse amplitude over the time period of 64 days. Fig.3.6 shows, that the deviations of the PWV are within the standard deviation of the multi-point TT method ($SD = \pm 0.1 \text{ m/s}^*$), except for one data point that was acquired on 09.12.2008. The deviation was caused by errors in the determination of the feet of the pulse waves due to transversal oscillations of the vessel wall (Fig.3.7). The error mechanism was identified and eliminated for later measurements (chapter 3.1.2, page 52).

*The specified SD results from the linear regression through the position-time data points that is performed in the multi-point TT method.

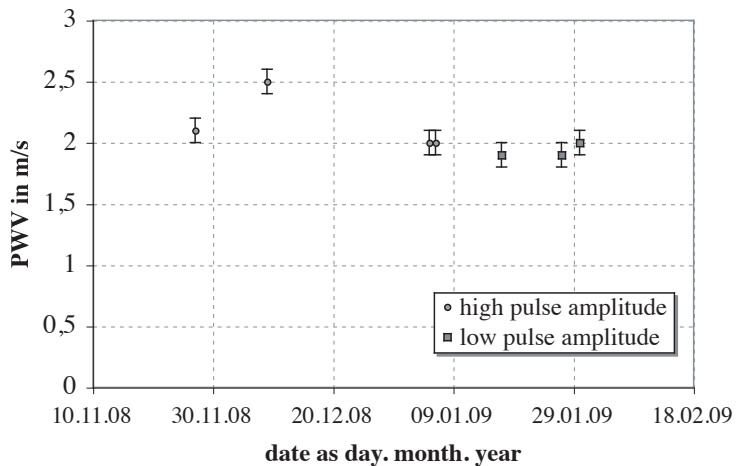
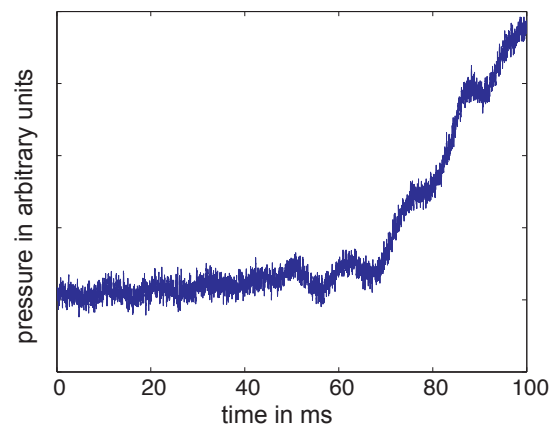


Figure 3.6: PWV of the phantom vessel acquired over a time period of 64 days beginning 14 days after the completion of the freeze-thaw cycling. The PWV appears to be independent of vessel age and of pressure pulse amplitude. The deviating data point is caused by a measurement error due to transversal vessel wall oscillations.

Figure 3.7: Pressure wave recorded on the phantom vessel with a high pulse amplitude that caused pressure oscillations with a frequency of approximately 100 Hz.



The influence of a deviating installation height on the PWV is plotted in Fig.3.8.a. The data points reveal that the PWV decreases by 0.026 m/s for each Millimeter that the phantom is installed too high in the MR system. The PWV of the phantom vessel decreases by 0.01 m/s per degree increasing temperature (Fig.3.8.b).

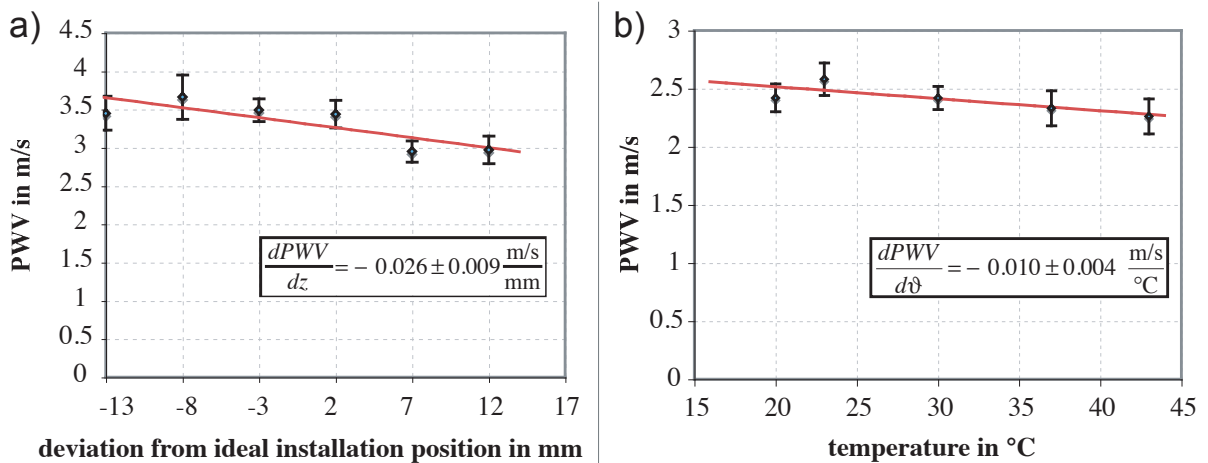


Figure 3.8: PWV of phantom vessels plotted versus a) the installation height of the vessel phantom with respect to the iso-center of the MR system and b) temperature. The standard room temperature was 19°C.

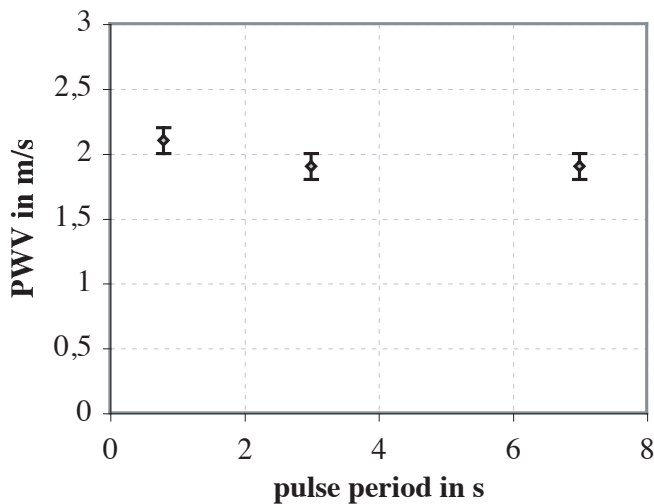


Figure 3.9: PWV of the phantom vessel plotted versus the pressure pulse period.

Fig.3.9 indicates that there is no dependence of the PWV on the pulse period. The data points lie within the standard deviation of the multi-point TT regression. The pressure curves of pulses with periods of 0.8 s showed the presence of wave reflections of previous pulses (for an example see Fig.3.10). Even though the wave reflections did not have adverse

effects on the PWV of the phantom vessel, the pulse period was set to values above 1s for the validation experiments in order to avoid previously reflected waves.

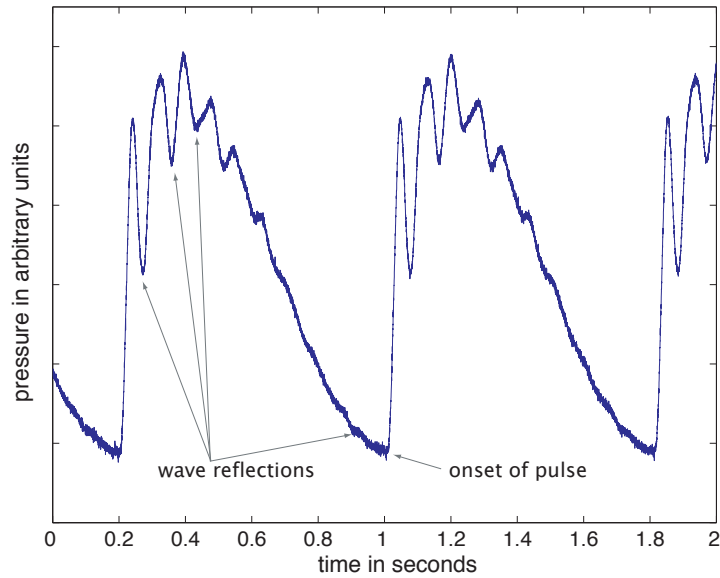


Figure 3.10: Pressure waves for a pressure pulse period of 0.8 s. Wave reflections of the previous pulse are still present when the following pressure pulse is initiated.

3.3 Discussion

A pulsatile elastic vessel phantom and several PVA-C vessels that have PWVs in the physiological range were developed and manufactured.

PVA-C proved itself to be a mechanically stable phantom material. A PWV change due to aging of the material was not observed over a time period of 64 days. Changes in pressure pulse amplitude and pulse period did not have measurable effects on the PWV. Reflected pulse waves of previous pressure pulses were observed in recorded pressure time courses when the pulse period is below 1 s. Although the standard deviation of the PWV did not increase for a pulse period below 1 s, it can be assumed that, in individual cases, reflected waves could increase the uncertainty in the PWV determination. To avoid reflected wave contributions to the pressure time courses of the pulse wave, pulse periods above 1 s were used for the validation measurements of the MR methods.

The PWV depends on static intra-luminal pressure, this is due to a non-hookean elasticity of the vessel wall. In the vessel that was used to validate the MR methods, the PWV decreases by approximately 0.03 m/s for a pressure drop of 10 Pa.

A raise in temperature by 1°C causes the PWV to decrease by 0.01 m/s, due to a decrease of Young's elastic modulus of the PVA-C. An accompanying decrease in fluid density contributes to a rise in the PWV which in the case of the present vessel is superposed by the effects of the softening of the vessel.

Deviations of the PWV of the vessel phantom under expected fluctuations of ambient parameters are well below 2%. It can be concluded that the vessel phantom is well suited for the validation of MR methods to measure the PWV.

Chapter 4

Transit Time Measurements of Flow Waveforms

Long term in vivo studies of the PWV of the major arteries on intact mice are necessary for the comprehensive characterization of atherosclerosis. Today MRI is routinely used to measure the PWV in humans [92]. The objective of this part of the work was to apply a flow encoding MRI method and the TT method to measure the regional PWV of the blood flow pulse in the descending murine aorta.

The transfer of the TT MRI method from humans to mice implies challenges that must be met. The physical sizes of organs in mice are approximately 20 times smaller than in humans. The PWVs in mice and humans are comparable. Selecting analogous anatomical measurement positions in mice and humans, the TT in mice is approximately one twentieth of the TT in humans. Mice's hearts beat approximately eight to ten times per second. Therefore, very high temporal and spatial resolutions are indispensable for PWV measurements in mice. The signal-to-noise ratio (SNR) limits the image resolution which is achievable in an experiment time that is reasonable for the animals. High temporal resolution relies on a precise heart triggering method and on heart rates that are stable throughout the course of the experiment.

A high-field MRI system with a main magnetic field strength of 17.6 T was used for the TT MRI measurements because it provides an intrinsically high SNR. An MR method to perform the PWV measurements was developed. The method is based on a CINE FLASH sequence. It features a minimized echo time in order to maximize the SNR. Phase velocity encoding is applied to record the time courses of blood flow velocities in two imaging slices. The developed data acquisition scheme of the method provides the necessary temporal resolution of one millisecond. To precisely trigger the data acquisition, a heart triggering / breath gating method that was developed in house was applied. A

program with a graphical user interface to determine the PWVs from the recorded MR data was developed.

The accuracy of the developed MRI method was verified on the pulsatile elastic vessel phantom that was described in chapter 3 (pages 47 ff.).

Finally the MRI method was applied to determine the mean PWVs of groups of atherosclerotic ApoE^(-/-) and healthy wild type mice in order to see if the method can distinguish between these animal groups on the basis of the PWV.

4.1 Methods

4.1.1 The MR Sequence

A dedicated MR sequence for PWV measurements in mice was developed for the Bruker Avance 750 system in the PVM-C++ programming environment[†] in the scope of this work.

The MR sequence applied phase velocity encoding to record the time courses of the blood flow velocities. The sequence was based on a two-dimensional CINE FLASH sequence. Velocity compensation is incorporated in all three gradient directions (see Fig.4.1). Acceleration and higher orders of motion were not compensated by the gradient switching scheme because the phase contribution of accelerated blood was estimated* to be below 4% of the phase contribution from blood flowing with constant velocity (see section 2.1.4.4 on page 28). The gradient switching scheme was optimized in favor of the shortest possible echo time in order to maximize the SNR and to minimize higher order motional artifacts.

Bipolar velocity encoding gradients were superposed onto the velocity compensating gradients in the slice direction to encode through-slice flow velocities. Three flow encoding steps were applied to each scan. The quality of the linear fit through the phase values by which the flow velocity is determined can be appraised when more than two velocity encoding steps are used. Velocity values of pixels with phase values that highly deviate from the fit can be substituted by the mean velocity of surrounding pixels. An increased number of flow encoding steps increases the precision of the determinable velocity and the acquisition time. Three flow encoding steps proved to be sufficient to measure the high blood flow velocities in the murine aorta [51].

Only velocities within the velocity window $\pm 1/2 v_{max}$ will be encoded with an unambiguous phase value (chapter 2.1.4.3). To accommodate the maximum flow velocities in the murine aorta the velocity window was set to $1/2 v_{max} = 1.66$ m/s.

The transit times of the pulse waves are in the range of a few milliseconds. Therefore, a temporal resolution of 1 ms was necessary to be able to obtain the PWV from the time courses of arterial blood flow velocities. The intrinsic temporal resolution of the MR sequence, equivalent to its repetition time, was 5 ms. Hence, the time courses of the flow velocities had to be sampled in an interleaved fashion. The sequence was initiated five times, every time with an additional delay of 1 ms between the trigger signal and the initiation of the sequence. The resulting five data streams were interleaved in the post

[†]PVM stands for Para Vision Method Manager.

*The estimation neglected higher orders of motion that are caused by turbulent blood flow.

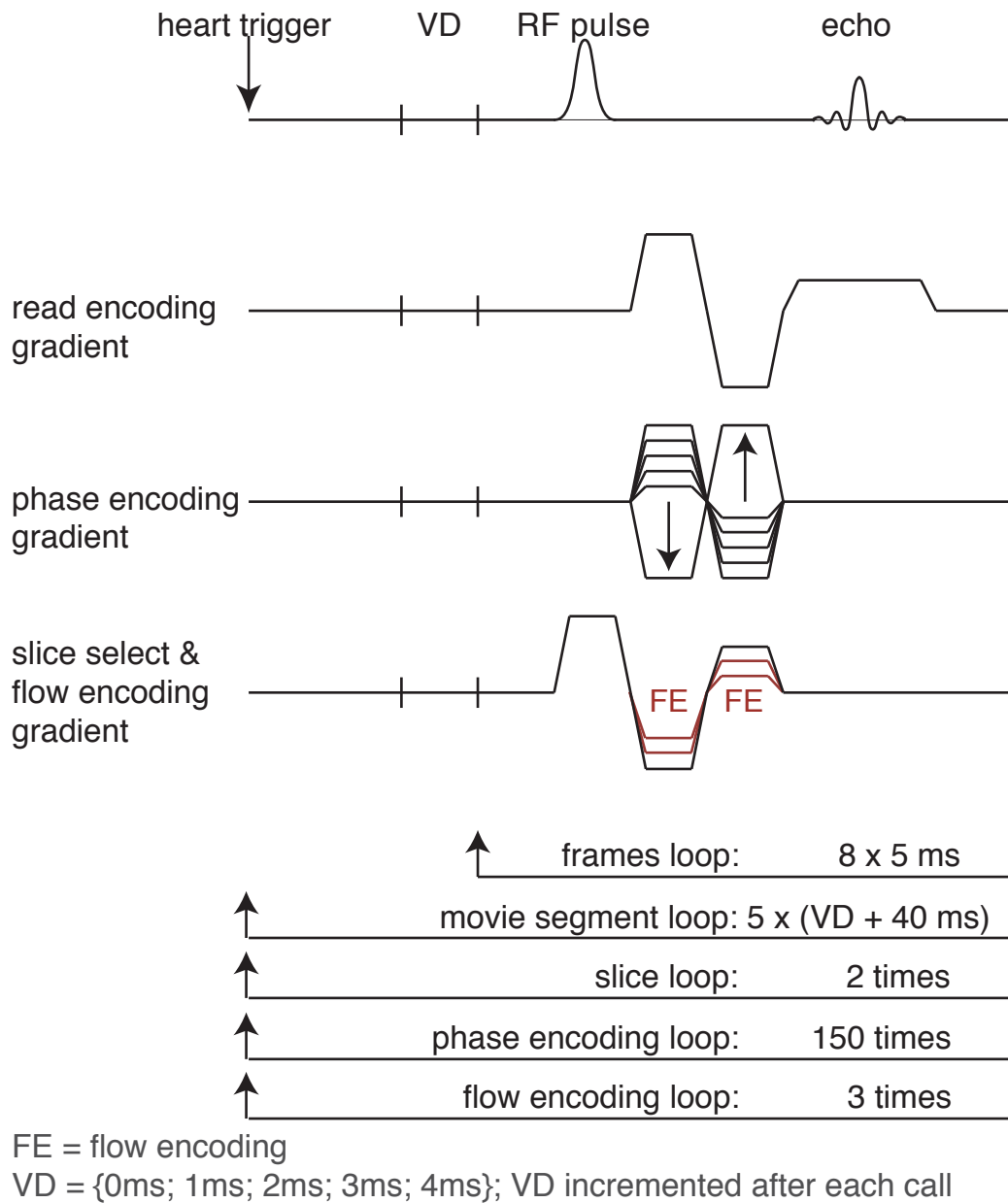


Figure 4.1: Scheme of the flow encoding MR method. Three different flow encoding steps are applied in the slice encoding direction for every k -space line. A fivefold repetition of the frames loop with interjacent incrementation of the variable delay (VD) produces an effective temporal resolution of 1000 time frames per second.

processing by custom software to generate a recording of flow velocities with an effective temporal resolution of 1 ms.

The phase encoding steps of the two imaging slices are acquired in an interleaved

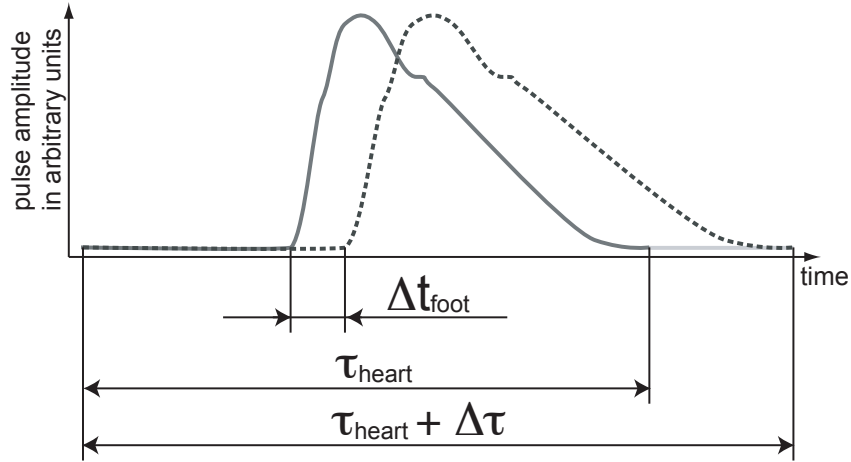


Figure 4.2: Change in the heart period and entailed registration time of the foot of the pulse wave. The two curves originate from the same imaging slice but the heart period differs. This causes a shifted registration time of the foot of the pulse wave.

fashion in order that variations in the heart period of the animals will not have an effect on the measured transit times of the pulse waves. To illustrate the effects of a changing heart period on the registered transit time, consider the case where the imaging slices are acquired consecutively. The transit time of the pulse wave (TT) is measured correctly when the heart period τ_{heart} is constant during the acquisition of the imaging slices I and II. When instead the heart period changes after the acquisition of slice I and has the value $\tau_{heart} + \Delta\tau$ during the acquisition of slice II, the apparent transit time is $TT_{app} = TT + \Delta t_{foot}$, with $|\Delta t_{foot}| \leq |\Delta\tau|$ and $sign(\Delta t_{foot}) = sign(\Delta\tau)$ (Fig.4.2). Generally the transit time is independent of the pulse period and the deviation of TT_{app} from TT indicates a potential shortcoming of consecutive slice acquisition. To avoid this effect, heart periods of mice were held stable within a range of 5 ms and the k -space lines of the two slices were acquired in an interleaved fashion.

The spatial in-plane resolution was $147 \times 147 \mu\text{m}^2$ and the slice thickness was 1 mm. The field of view (FOV) was $22 \times 22 \text{ mm}^2$. The matrix size was 150×150 pixels. The echo time was 1.6 ms. The signal echo was formed when 25% of the readout gradient cycle time had passed in order to minimize the echo time. The Gauss RF excitation pulse had a length of $200 \mu\text{s}$ and an excitation angle of 20° . Signal averaging was not applied.

4.1.2 Data Analyzing Software

The order of the MR data packets that were recorded with the developed MR sequence was highly interlaced due to the interleaved temporal data acquisition, the flow encoding, and the interleaved slice acquisition. The software of the MRI system was not able to reconstruct the data correctly. A software program for data analysis that runs under MATLAB (The Mathworks, Inc., Natick, MA, USA) was programmed in the scope of this work. The software has a graphical user interface in order that users who are not familiar with the basic modules of data analysis can evaluate data as a matter of routine in future animal studies.

The workflow of the program is illustrated in Fig.4.3. The recorded data includes a longitudinal scan of the aorta that is used to determine the distance between the measurement locations of the two-point TT method. The data set also comprises the set of velocity encoded scans as k -space data and the associated gradient moments (M_1) that were used for velocity encoding.

Before the data will be converted to complex position space data by the fast Fourier transform (FFT) the signal echoes are centered, the baseline is corrected, and the data packets are arranged in the correct order.

Velocity information is computed for pixels inside the vessel lumen by fitting a line to the phase values of the complex MR data (the arguments) as a function of the first moments of the velocity encoding gradients (phase difference method) for every time frame. Velocity values of pixels where the fit through phase values and first gradient moments had a quality below $R^2 = 0.85$ were substituted by the mean velocity value of the eight surrounding pixels.

Velocity offsets due to eddy currents and concomitant gradient fields were corrected by fitting a two dimensional second order polynomial surface to the time averaged velocity values of stationary tissue* which was subtracted from the velocity values of every time frame [93].

The velocities of each time frame were averaged over the luminal area. The "foot-to-foot" method is used to determine the transit times of the pulse wave. The PWV is calculated according to the TT method.

*Tissue was considered stationary when the time standard deviation of the velocity values was within the 25% percentile.

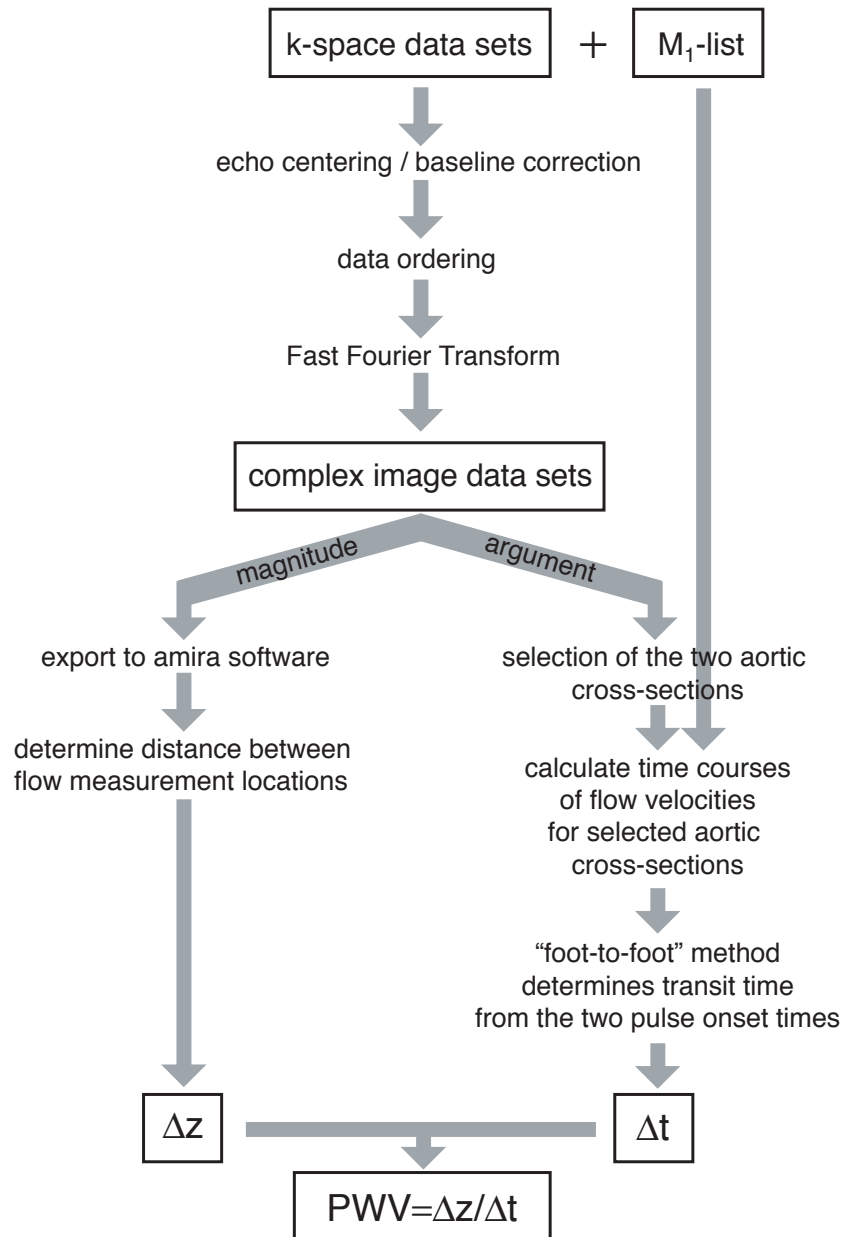


Figure 4.3: Workflow of the data analyzing software. The raw data set contains the flow velocity time courses in phase encoded complex k-space data sets, the list of applied flow encoding moments, and axial scans for the determination of the displacement between the measurement locations of the flow velocities.

4.1.3 Validation Experiments

The MR method was validated under standardized conditions on the pulsatile elastic vessel phantom that was developed in the scope of this work (chapter 3 on page 47).

The phantom allowed for the determination of flow velocity waves using the developed MR method and for measurements of pressure waves utilizing the pressure catheter. The PWVs obtained by the two different measurement methods were compared to each other by a two-sided t-test for unpaired samples in order to give evidence of the accuracy of the MR method.

The multi-point TT method was used to determine the PWV of the PVA-C vessel by pressure measurements. In order to obtain a statistically sufficient number of data points, 64 pressure time courses were recorded at different catheter positions. The pulse period was 2.4 s. The pressure data was analyzed in MATLAB to determine the onset times of the pressure waves for each measurement position of the pressure catheter. The measurement positions were plotted versus the corresponding pressure pulse onset times; the slope of the linear regression yielded the PWV (see chapter 3.1.3 on page 53).

The multi-point TT method was also applied to determine the PWV of the vessel phantom by the flow encoded TT MR method[†]. Ten flow velocity curves were recorded at each of the eight MR imaging slices. The slices were positioned perpendicularly to the vessel at the positions given in Tab.4.1. A set of two-dimensional FLASH experiments was leading the measurement protocol to localize the measurement positions on the vessel phantom. A perpendicular slice orientation was crucial to avoid displacement artifacts which are caused by flow traversing the imaging slice in a non-perpendicular angulation (section 2.1.4.1 on page 19). The pulse period again was set to 2.4 s. The stainless steel catheter that was used for pressure measurements had to be removed for the MR measurements. MR data were interleaved and processed with the developed data analysis routine that runs under MATLAB.

imaging slice	1	2	3	4	5	6	7	8
slice position in mm	-10.0	-7.5	-5.0	-2.5	2.5	5.0	7.5	10.0

Table 4.1: Slice positions of the multi-point MR validation measurements. The position 0 mm corresponds to the iso-center of the MR system.

In order to assess the precisions of the two-point TT method, MR data recorded for the multi-point TT method were also utilized to determine the PWV values by the two-point TT method at imaging slices ± 10.0 mm, ± 7.5 mm, ± 5.0 mm, and ± 2.5 mm.

[†]In living mice, only two imaging slices could be acquired due to the limited experiment time. Therefore, the two-point TT method had to be applied in mice.

4.1.4 In Vivo Experiments

4.1.4.1 Animal Handling

The proposed MR method was designed to utilize the two-point TT method in vivo in the descending murine aorta. MR measurements were performed on a group of five female eight-month-old ApoE^(-/-) mice and a group of four age-matched female C57Bl/6J mice. The ApoE^(-/-) mice were fed a western type diet (TD 88137, Harlan Laboratories, Inc., Indianapolis, IN, USA) 10 weeks prior to MR measurements.

During the examinations the mice were anesthetized with an isoflurane inhalation (1.5 - 2.0 Vol.%) in O₂ (1.5 - 2.0 L/min) applied by means of a nose cone. It is recognized that isoflurane is a nonspecific sympathetic antagonist and can cause vasodilation and a decrease of the PWV [30]. Anyhow, the decision was made to use isoflurane because the animals had to be immobilized for the experiments and an inhalation anesthesia was preferred over an infusion anesthesia due to the limited access in the MR system. The isoflurane concentration was held as close to 1.7% as the animals allowed in order to minimize anesthetic induced deviations in the PWV measurements.

Mice were placed vertically (head up) in the RF resonator. The accessible diameter of the RF resonator (25 mm) did not allow for the use of an animal positioning system. The mice were hung in the resonator by means of a flap of tape that was attached to their forelimbs. The flap extended to the outside of the resonator and was affixed there. This allowed for adaptations of the animal position in the resonator without the need to remove the nose cone. Due to the small diameters of the gradient insert and the RF resonator, mice's body temperature could be kept constant at 37°C by adjusting the temperature on the gradient insert temperature control unit. The temperature of the unit was set to 37°C before mice were placed in the MR system and was lowered one minute prior to PWV measurements to 32°C to remove heat that is dissipated by the gradient insert to prevent a temperature change of the mouse. The temperature was reset to 37°C with the completion of the MR PWV measurement.

All experimental procedures were in accordance with institutional guidelines and were approved by local authorities.

4.1.4.2 Data Acquisition on Mice

At least one PWV measurement was performed on every animal. Four of the ApoE^(-/-) mice and all of the C57Bl/6J mice were sufficiently stable under anesthesia so that a second PWV measurement was accomplished. One ApoE^(-/-) mouse allowed only one PWV

measurement because eventually she developed non-periodic breathing patterns during the second PWV measurement. The causes of the arrhythmic breathing are not understood but are assumed to be a dispositional reaction to isoflurane because these breathing patterns reproducibly occur only in certain animals and alleviate with the concentration of the anesthetic.

Two imaging slices were positioned perpendicularly to the thoracic and the abdominal aorta to measure the PWV with the two-point TT method. A perpendicular slice orientation was crucial to avoid displacement artifacts in the flow measurements. A set of two-dimensional FLASH experiments which is illustrated in Fig.4.4 was acquired and used to position the flow measurement slices.

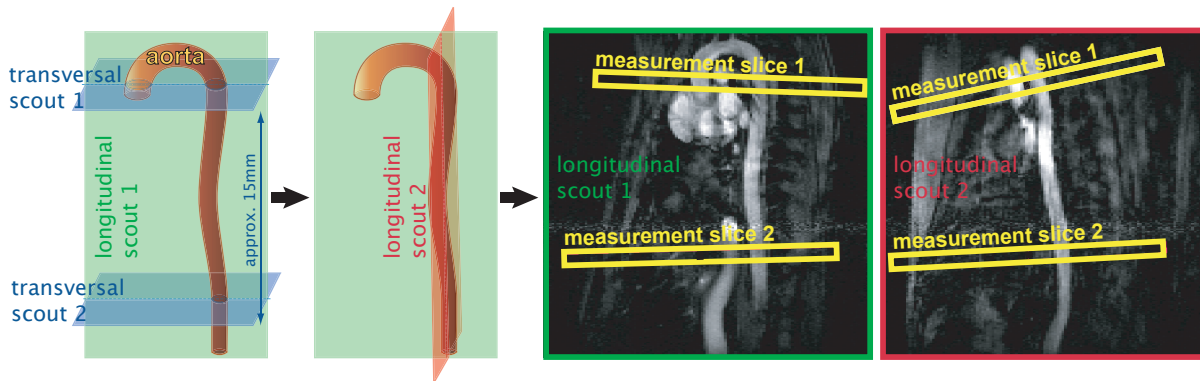


Figure 4.4: In vivo positioning of the image slices for the PWV TT measurements. First step: Two parallel transversal scouts are recorded (transversal scouts 1 & 2). Second step: A longitudinal scout imaging slice that runs through the three intra-luminal cross sections of the transversal scouts is arranged and recorded (longitudinal scout 1). Third step: A second longitudinal slice (longitudinal scout 2) that is perpendicular to longitudinal scout 1 and runs through the image of the aorta in longitudinal scout 1 is arranged and recorded. Fourth step: The two PWV measurement slices are arranged perpendicularly to the images of the aorta in both longitudinal scouts by visual judgment. It is absolutely sufficient to arrange the slices by visual judgment.

The flow velocity window was set to $1/2 v_{max} = 1.66$ m/s to accommodate the maximal blood flow velocities in the murine aorta. The excitation angle of the RF pulse was empirically set to 40° so that the signal intensity of intravascular blood flowing through the measurement slices was maximized. The mice had a heart period of approximately 115 ms. A time window of 40 ms was sufficient to sample the late diastole and early systole. All other parameters of the measurement protocol were set as in the measurements on the vessel phantom. The total acquisition times ranged from 15 to 20 min.

The program AMIRA (Visage Imaging, Inc., San Diego, CA, USA) was applied to gauge

the distance between the two measurement locations. Therefore straight-line segments were drawn along the luminal midline in a longitudinal reference scan of the aorta (see Fig.4.5.a).

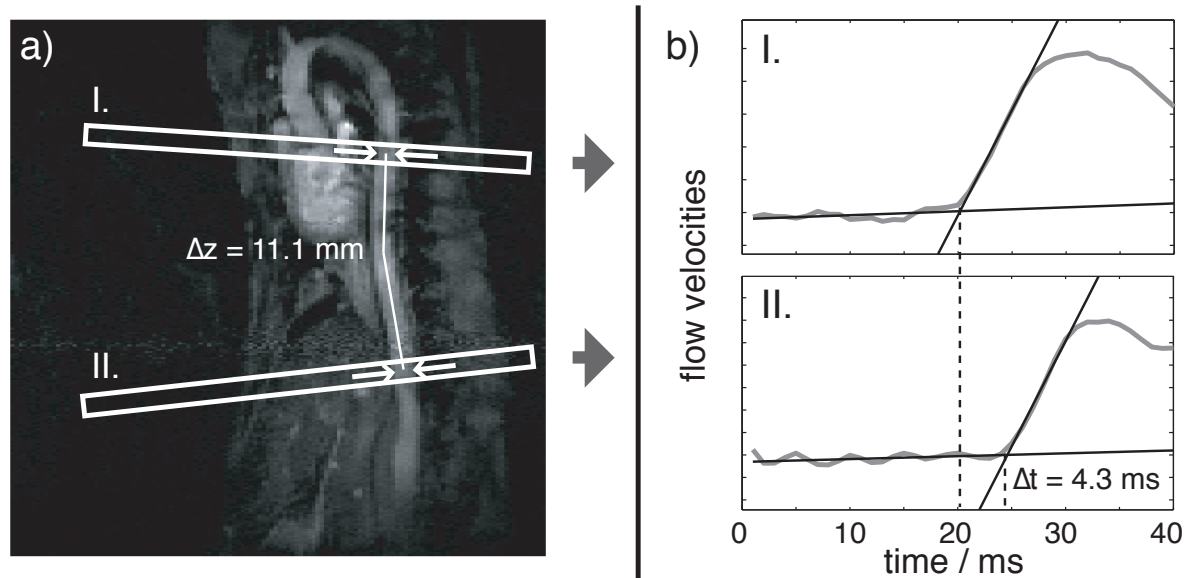


Figure 4.5: **a)** Reference scan of the murine aorta with indicated velocity measurement slices (I: thoracic aorta, II: abdominal aorta). The arrows indicate the regions where velocities were evaluated to determine the PWV (two-point transit time (TT) method). **b)** Representative flow velocity time courses of an ApoE^(-/-) mouse. The linear regression lines determine the abstract onset times of pulsatile flow. Only the late diastole and early systole were recorded to determine the PWV, which in this case resulted to be $PWV = \Delta z / \Delta t = 2.6 \text{ m/s}$.

The flow encoded MR data were processed using the MATLAB routine that was also used for the analysis of the data acquired on the vessel phantom. The flow velocity curves in the velocity-time diagrams showed sharp bends between the sections before and during the pulse (see Fig.4.5.b). This allowed for a semi automatic selection of the fit ranges that defined the onset times of the flow pulse. The fit range before the pulse was selected manually, including data points on an approximate horizontal line. The beginning of the pulse fit region was set automatically as a series of three consecutive data points with velocity values at least two standard deviations above the extrapolated fit line of the section before the pulse. The end point was selected manually as the last data point on the first straight portion of the flow pulse section.

Occasionally trigger signals started the data acquisition during the breathing movement and motional artifacts in the MR images were the result. Some of the motional

artifacts altered the signal amplitude and phase information in the vessel lumen. Altered regions were excluded from the calculation of the flow velocities when the artifacts could be assigned visually to extraluminal topologies.

Differences in the mean PWV values of the two animal groups were tested by a single sided t-test for the hypothesis of equality against the alternative of a higher value for the ApoE^(-/-) group. A p-value < 0.05 was considered significant. In this work all PWV values are given as mean \pm standard error (SE) unless otherwise noted.

4.2 Results

4.2.1 Validation Experiments

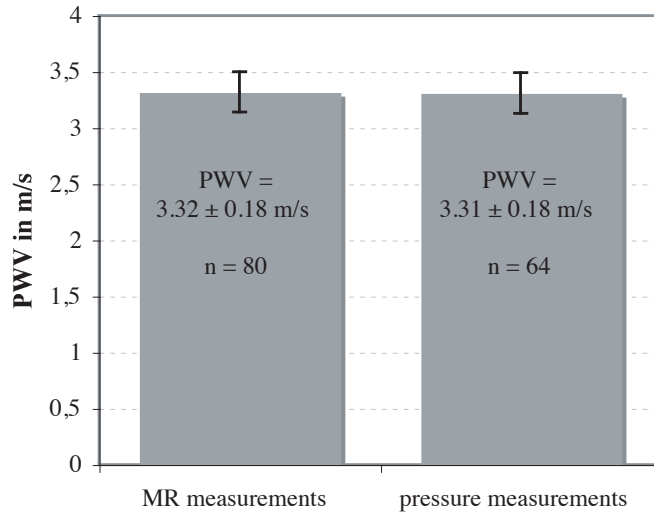


Figure 4.6: PWVs in the phantom vessel measured with the MR method and the pressure catheter. Values are given as mean \pm SE. **n** indicates the number of MR measurements and pressure measurements used for the multi-point TT method.

In the vessel phantom that was used for validation of the MR method, a $\text{PWV} = 3.31 \pm 0.18$ m/s was obtained by the pressure catheter measurements (Fig.4.6). The MR flow measurements determined a $\text{PWV} = 3.32 \pm 0.18$ m/s. Comparison of the PWV values of the pressure and MR measurements resulted in no significant difference ($p \leq 0.99$). The parameters and results of the validation measurements are summarized in Tab.4.2.

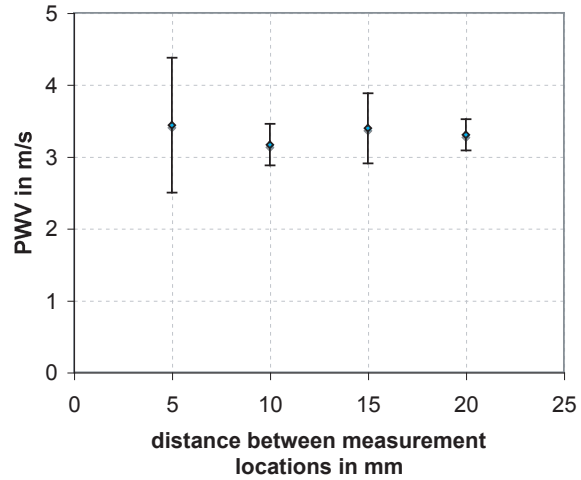
The analysis of the precision of the two-point TT method confirmed that the standard error of the PWV increases with decreasing separation of the measurement locations (Fig.4.7, Tab.4.2).

4.2.2 In Vivo Experiments

Representative flow profiles recorded in the thoracic and abdominal aorta of an $\text{ApoE}^{(-/-)}$ mouse are displayed in Fig.4.8. Similar flow profiles were observed in C57Bl/6J mice. High acceleration and flow velocities in the upper thoracic aorta cause turbulent blood flow and prevent the formation of a parabolic flow profile. The damping effect of the upper aorta provides for the development of parabolic flow profiles for at least the later phases of systolic flow. These observations accord with a publication about hemodynamics in the aortic arch and upper thoracic aorta of mice by Feintuch et al. [94].

Fig.4.5.b shows representative time courses of flow velocities which were recorded on an $\text{ApoE}^{(-/-)}$ mouse. The measured PWV values ranged from 1.9 m/s in a C57Bl/6J

Figure 4.7: Standard errors of the PWV, determined by the two-point TT method, decrease with increased separation of the measurement locations.



pressure TT measurements		
number of data points	measurement positions	PWV
64	multi-point	3.31 ± 0.18 m/s*
flow velocity TT measurements		
number of data points	measurement positions	PWV
80	multi-point	3.32 ± 0.18 m/s*
20	two-point at ± 10.0 mm	3.30 ± 0.22 m/s
20	two-point at ± 7.5 mm	3.39 ± 0.49 m/s
20	two-point at ± 5.0 mm	3.17 ± 0.29 m/s
20	two-point at ± 2.5 mm	3.44 ± 0.94 m/s

Table 4.2: Parameters and results of the validation PWV measurements. PWV values are given as mean \pm standard error. *The mean PWV values of the pressure and MR measurements show no statistically significant difference ($P \leq 0.99$).

mouse to 3.8 m/s in an ApoE^(-/-) mouse. The average values of each animal group are PWV = 3.0 ± 0.2 m/s for ApoE^(-/-) mice and PWV = 2.4 ± 0.2 m/s for C57Bl/6J mice (Fig.4.9). The mean value of the ApoE^(-/-) group was significantly higher than that of the C57Bl/6J group ($p \geq 0.007$).

An overview of the experiment parameters and the results for both animal groups is given in Tab.4.3.

PWV values of mice with a body mass above 34 g showed a high uncertainty (Fig.4.10).

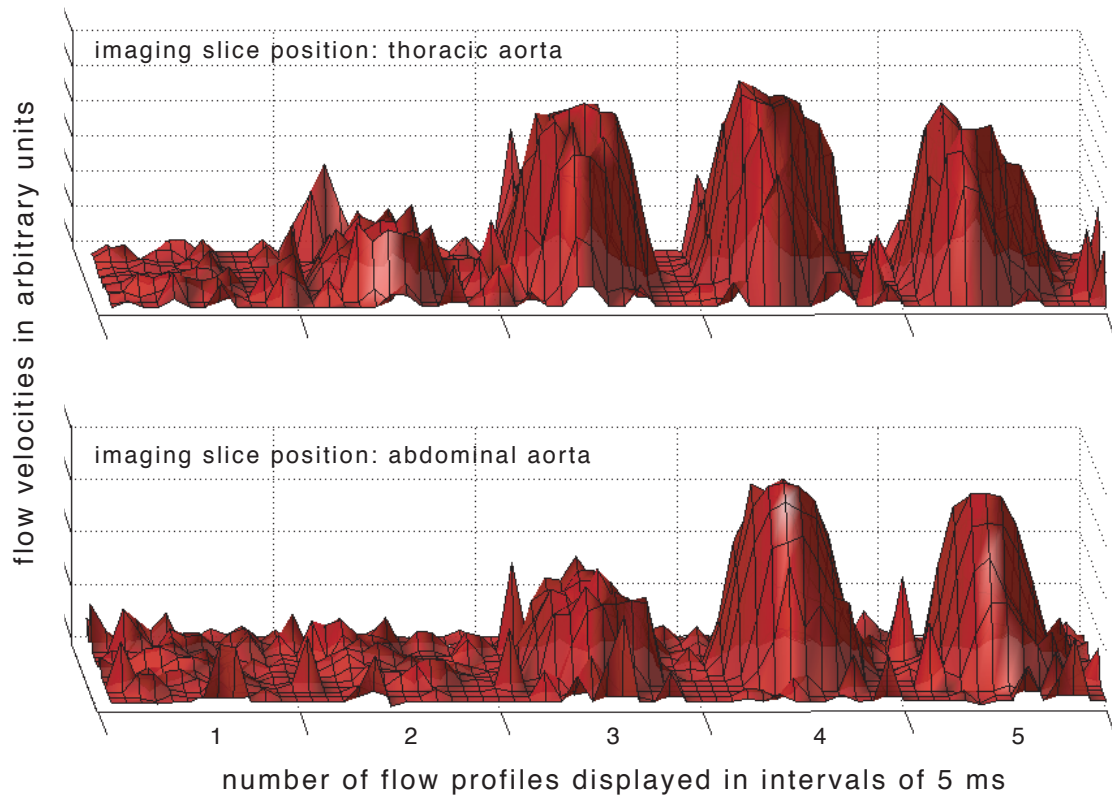


Figure 4.8: Flow profiles of an eight-month-old $\text{ApoE}^{(-/-)}$ mouse. The profiles are displayed for 5 ms intervals from the end diastole to the mid systole. Parabolic flow profiles develop due to laminar flow in the abdominal aorta whereas the flow profiles of the upper thoracic aorta clearly exhibit turbulent flow. Spikes surrounding the flow profiles are caused by pixels of low signal intensity.

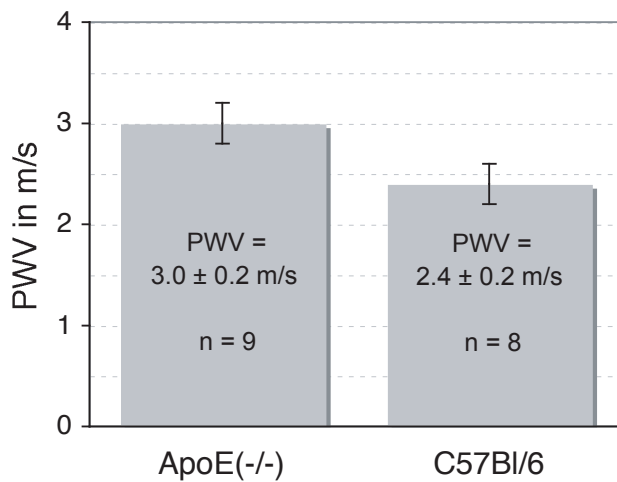


Figure 4.9: PWVs of groups of eight-month-old $\text{ApoE}^{(-/-)}$ and C57Bl/6J mice. The $\text{ApoE}^{(-/-)}$ mice received a western type diet 10 weeks prior to the measurements. The PWV values are given as mean \pm SE. The number of experiments per group is indicated by **n**.

parameter (mean \pm SD)	ApoE ^(-/-) group	C57Bl/6J group
age of animals (mo.)	8	8
number of animals	5	4
number of measurements	9	8
body mass (g)	28.4 \pm 4.5	30.4 \pm 0.9
anesthetic		
isoflurane (%)	1.8 \pm 0.2	1.7 \pm 0.2
in O ₂ (l/min)	1.5 \pm 0.0	1.8 \pm 0.4
avg. heart period (ms)	109 \pm 9	112 \pm 4
change in heart period of single experiments (ms)	2.0 \pm 1.6	2.2 \pm 1.5
distance between measurement locations (mm)	12.2 \pm 1.1	9.8 \pm 1.3
PWV* (m/s) (mean \pm SE)	3.0 \pm 0.2	2.4 \pm 0.2

Table 4.3: Parameters and results of the in vivo MR PWV measurements. * The mean PWV of the ApoE^(-/-) group is higher than the mean PWV of the C57Bl/6J group with statistical significance ($p \geq 0.007$).

The principle to this phenomenon is unknown. These mice tightly filled the RF resonator. The constriction might have induced stress and alterations of blood pressure or vascular tone which have effects on the PWV. Mice with a body mass below 34 g still had little room in the resonator and a soft foam rubber pad was needed to lightly push the pneumatic balloon against their thorax. These mice did not exhibit large variations in the PWV. Therefore, only mice with a body mass below 34 g were included in the study.

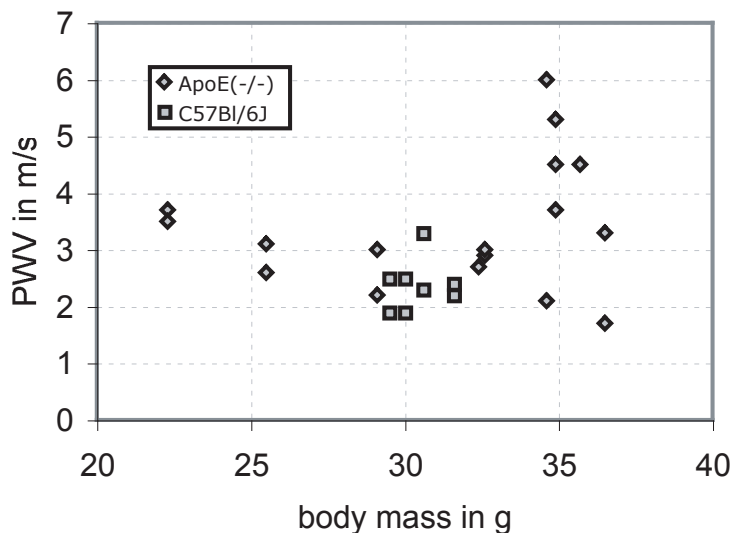


Figure 4.10: Individually measured PWVs of ApoE^(-/-) and C57Bl/6J mice plotted against the animal's body masses. Above 34 g the PWV values show a strong scatter. Vertically aligned data points belong to the same animal.

The determination of the PWV from the MR data was only possible when the heart period of the mice did not change by more than 5 ms throughout the experiment time. Due to the empirically developed tempering and anesthetic protocol the heart period could be held sufficiently stable.

4.3 Discussion

4.3.1 The MR Sequence

An MR sequence using phase velocity encoding, temporally interleaved data acquisition, and the TT method was developed and successfully applied to measure the PWV in a phantom vessel and in the descending aortas of mice using high-field MRI at 17.6 T.

The measurements are made possible by the high SNR intrinsic to high-field MRI and the large filling factor of the used RF resonator. The interleaved acquisition scheme of the time frames and the pneumatic triggering technique provide the necessary temporal resolution. Flow compensation and the short echo time of the MR sequence greatly reduce flow artifacts. Flow artifacts due to turbulent blood flow in the proximal aorta are omnipresent but do not impair PWV measurements in the descending aorta. The short echo time also alleviates susceptibility artifacts which are usually caused by boundaries of tissues with differing magnetic susceptibilities in high-field MRI.

4.3.2 Validation Experiments

PWV values of the vessel phantom were investigated by multi-point TT MR and pressure measurements. The PWV values do not differ with statistical significance ($p \leq 0.99$). The relative standard errors of both methods are 5%.

With the two-point TT method, the relative error ranges from 7% to 27% for different measurement slice separations. The smaller the separation between the two measurement positions the higher is the relative uncertainty of the TT. In the phantom measurements, the slice positions were known, but in the in vivo experiments, they must be determined. Therefore, in the in vivo measurements, the relative error in the PWV will increase even more for decreasing slice separations. Consequently, the slice separation has to be as large as possible in the in vivo experiments where due to limited acquisition time only the two-point TT method can be applied. The mean PWV values are independent of the separation of the measurement positions.

4.3.3 In Vivo Experiments

The precision of the MR method is high enough to distinguish between a group of five eight-month-old ApoE^(-/-) mice and a group of four age matched C57Bl/6J mice. The PWV measured on the group of eight-month-old ApoE^(-/-) mice was 25% above the PWV in the age-matched wild-type group. The difference is significant ($p \geq 0.007$). The method

cannot distinguish between single animals because the SD of single measurements is too large. Fig.4.10 illustrates the variations of different measurements on same animals.

The PWV values measured in mice in this study range from 7% above to 37% below the values previously stated in literature for mice of similar age [32, 95, 31, 96]. The different results of ultrasound and pressure measurements on alike animal groups by Hartley and Wang suggest that the deviations between the findings of this study and literature might be caused by systematic deviations inherent to the different methods of measurement. Or deviations to the findings were possibly caused by the differences in age of the animals or resulted because different animal strains were used. Another cause can be the use of the anesthetic isoflurane in this study which may stimulate the sympathetic nervous system and, thus, can cause vasodilation and a decrease of the PWV. Isoflurane was used in this study because an inhalation anesthetic was preferred over an injection anesthetic due to the limited access in the MR system. Mice were placed head up in the vertical magnet which might also have an influence on the PWV. The fact that mice were placed vertically in the RF resonator might also have an effect on the PWV. Wang et al. found no significant differences in PWV values between ApoE^(-/-) and C57Bl/6J mice that were younger than 13 months [31]. In this study a significant difference was observed at eight months of age already. In the current work, ApoE^(-/-) mice received a different, western type diet which accelerates aortic wall remodeling and increases elastic destruction and thus the PWV [97].

A recent MR study at 7 T by Zhao et al. [98] presented PWV values for nine-month-old ApoE^(-/-) and C57Bl/6J mice that exceed the values that were determined in this and other studies. The group applied the TT method but due to a lack of temporal resolution they did not apply the foot-to-foot method. In their approach the systole was scanned for 40 ms, interpolated by sixth order polynomials, and the transit times were defined by the arrival times of the half-values of the interpolated flow velocities. This approach is extruded to wave reflections and its accuracy must be questioned.

Wave reflections, mainly generated by the microvascular bed, i.e. the arterioles, will change the shape of the flow wave and might affect the estimation of pulse wave velocities [99]. Assuming a hypothetical PWV of 5 m/s and a distance of 20 mm between the abdominal measurement position and the microvascular bed, the reflected pulse wave needs 8 ms to return to the abdominal aorta. In this study, at most the first 7 ms of the flow velocity upstroke were used for the calculation of the PWV, therewith wave reflections do not impose an impediment.

Changes in the heart period that are larger than 5 ms do generate “ghost” artifacts in the phase maps and vitiate an accurate determination of the PWV. Heart periods were

held sufficiently steady throughout the experiments due to the developed protocol for anesthesia and body temperature control.

A part of the errors in PWV measurements are intrinsic to the MR method itself. Another contribution can be attributed to in vivo effects[‡]. The standard errors of the phantom and mouse MR measurements are approximately equal. Therefore, the main portion of the error can be attributed to the MR method.

[‡]Arteries contain muscle cells and can actively change their elasticity and PWV.

Chapter 5

Transit Time Measurements of Distension Waveforms

In this part of the work, the motivation was to determine the regional arterial PWV within a reduced acquisition time. The method again must work without pressure measurements. With pulsatile flow in elastic vessels, the flow, the pressure, and the circumferential strain are interrelated. Using Doppler ultrasound on humans, Hoeks et al. showed that the phase delay between two arterial distension waveforms can be used to determine the PWV by the TT method [100].

In this chapter, the determination of the arterial PWV by a TT method that uses the time courses of intra-luminal areas is presented. Magnitude data is analyzed to determine the cross-sectional areas. The presented approach uses the 17.6 T MR system with its high SNR and the MRI method that was described in chapter 4 but this time without the flow encoding. This reduces the acquisition time to one third of that of the flow encoded method, i.e., to approximately five to eight minutes.

Again, the challenges are the physical sizes of the organs in mice (approx. one twentieth of the sizes in humans) and the high heart rates (eight to ten beats per second) that require high spatial and temporal resolutions. The heart triggering / breath gating method described in section 2.3.3 on page 45 provided the precise trigger signals that the temporal resolution relies on.

A data evaluating software with a graphical user interface to manually segment intra-luminal areas and to determine the PWV by the transit time of areal distension waveforms was developed.

The accuracy of the developed MRI method and the data evaluation procedure was verified on the pulsatile elastic vessel phantom that was described in chapter 3 (pages 47 ff.).

Finally, the MRI method was applied to determine the mean PWVs of groups of atherosclerotic ApoE^(-/-) and healthy wild type mice. The applied measurements determined if the image contrast and the achievable spatial resolution suffice for the accurate identification of the wall-lumen interface of the artery and if, therefore, the method can distinguish between the animal groups.

5.1 Methods

5.1.1 Partial Volume Effect and Zero-Filling

The detection of the intra-luminal boundaries is the central task in the determination of PWVs by planimetry. MR images of the thoracic aorta of an eight-month-old ApoE^(-/-) mouse revealed that the luminal diameter expands by 180 μm during the early 20 milliseconds of the systole, i.e., 9 $\mu\text{m}/\text{ms}$ (assuming a linear relation between time and diameter). The native resolution of the MR sequence is 147 x 147 μm^2 . The resolution was limited by the acquisition time that was reasonable to the animals. It seems that the MR method is not suited for the measurement of luminal diameter changes within five to ten milliseconds because the nominal resolution does not meet the demands of the Nyquist-Shannon sampling theorem.

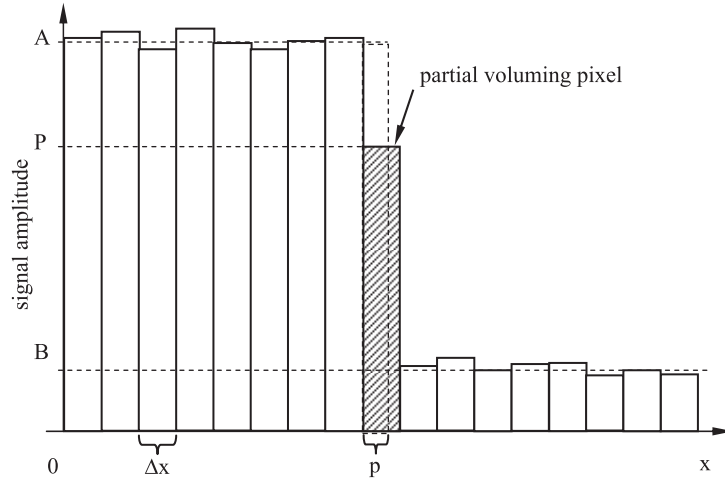
Olga Tymofiyeva et al. showed that the precision of the localization of boundaries can surpass the nominal resolution by almost an order of magnitude when *a priori information* about the objects to be imaged is used and the acquired MR time signals are *zero-filled* prior to image reconstruction [101, 102]. The *a priori information* is: the objects are *uniform objects*, i.e., they extend over several voxels and have a uniform distribution of their properties, such as spin density and relaxation rates. In addition the objects are separated by *sharp boundaries*. In an NMR experiment, the continuous distribution of object properties is acquired and represented in a discretized fashion, that is, in an image that consists of pixels. A *partial voluming effect* occurs, when the boundary between objects lies within one pixel.

The following considerations, made by Olga Tymofiyeva in her dissertation [102], demonstrate how this partial voluming effect can increase the precision of the boundary localization. Consider the sharp boundary between a one dimensional extended uniform object of mean signal amplitude A and a background of non-zero mean amplitude B (Fig.5.1). The signal amplitudes of both compartments are superimposed by noise of the standard deviation σ_0 . The pixel that contains the border between the object and the background has the signal amplitude P . Assuming that the signal of the partially filled voxel proportionally relates to the fraction that is occupied by the object yields a relation to identify the actual object boundary:

$$\frac{p}{\Delta x} = \frac{P - B}{A - B}. \quad (5.1)$$

Here Δx is the nominal image resolution and p is the part of the pixel that belongs to the object.

Figure 5.1: One-dimensional discretized image of the boundary between an extended uniform object and the background. The nominal image resolution is Δx . The heights of the bars represent the image signal amplitude in the presence of noise. The true object contours are represented by the dashed lines at the levels A and B and through the partial voluming pixel. Illustration with kind permission from Olga Tymofiyeva [102].



The uncertainties in the amplitudes A and B are $\sigma_0/\sqrt{N_1}$ and $\sigma_0/\sqrt{N_2}$ where N_1 and N_2 are the numbers of pixels in the object and the background, respectively, excluding the partially volumed pixel. The error in the precision of the boundary determination σ_p is derived by the error propagation law and can be approximated for large N_1 and N_2 :

$$\sigma_p \approx \frac{\Delta x \cdot \sigma_0}{A - B} = \frac{\Delta x}{CNR_{AB}} \quad (5.2)$$

where CNR_{AB} is the contrast-to-noise ratio as it is defined by:

$$CNR_{AB} = \frac{A}{\sigma_0} - \frac{B}{\sigma_0} = SNR_A - SNR_B. \quad (5.3)$$

Eq.5.2 shows that the achievable precision in the boundary detection surpasses the nominal resolution by a factor that is equal to CNR_{AB} .

In this work, it was tested if the CNR is sufficient and if the assumption that the image signal intensities of intra-luminal areas and surrounding tissue are sufficiently uniform and the object boundaries are sharp enough to apply the above method of boundary detection is valid. The images of the murine aortas were interpolated by zero-filling the k -space data from the original 150 by 150 data points to 512 by 512 data points. This yielded an image resolution of $43 \times 43 \mu\text{m}^2$. In the interpolated image, the number of pixels of the smaller object, i.e., the lumen, was approximately 1000 and increases by approximately ten pixels per millisecond during the early systole.

5.1.2 Validation Experiments

The MR method was validated under standardized conditions on the pulsatile elastic vessel phantom that was presented in chapter 3 on page 47. The phantom allowed for the determination of areal distension waveforms using the developed MR method. Catheter measurements of pressure waves again provided the reference PWV value. The PWVs obtained by the two different measurement methods were compared to each other by a two-sided t-test for unpaired samples in order to give evidence of the accuracy of the MR method.

The multi-point TT method was used for the pressure measurements. Thirty-six pressure time courses were recorded at different catheter positions. The pulse period was 1.8 s. The pressure data was analyzed in MATLAB to determine the PWV as described in chapter 3.1.3 on page 53.

For MR measurements, the two-point TT method was applied. The MR sequence that was dedicated for the flow-encoded PWV TT measurements (described in section 4.1.1 on page 63) was applied for the luminal area measurements. Velocity compensation was active in all three spatial directions but the bipolar flow encoding gradients were deactivated. Higher orders of motion were not compensated in favor of a minimal echo time that increases the SNR.

The transit times of the distension waves are in the range of a few milliseconds and, therefore, the interleaved acquisition scheme recorded sequences of magnitude images at the two measurement slices with an effective temporal resolution of 1 ms.

The measurements were performed on the 17.6 T MR system using the same hardware as in chapter 4. Again, the spatial in-plane resolution was $147 \times 147 \mu\text{m}^2$ and the slice thickness was 1mm. The field of view (FOV) was $22 \times 22 \text{ mm}^2$. The matrix size was 150×150 pixels. The echo time was 1.6 ms and the signal echo was brought forward to 25 % of the readout gradient cycle time. The Gauss RF excitation pulse had a length of $200 \mu\text{s}$ and an excitation angle of 20° . Signal averaging was not applied.

Eight MR measurements were performed. The slices were positioned perpendicularly to the vessel at the $\pm 7 \text{ mm}$ positions (measured from the MR iso-center in the longitudinal direction). A set of two-dimensional FLASH experiments was leading the measurement protocol to localize the measurement positions on the vessel phantom. MR data were interleaved, zero-filled to 512×512 pixels and processed with a developed data analysis routine that runs under MATLAB. Details about the zero-filling and the data processing are given in the sections 5.1.1 and 5.1.4.

5.1.3 In Vivo Experiments

MR measurements were performed on the same animal groups as in chapter 4. The group of five female eight-month-old ApoE^(-/-) mice received a western type diet (TD 88137, Harlan Laboratories, Inc., Indianapolis, IN, USA) 10 weeks prior to MR measurements. The group of the four age-matched female C57Bl/6J mice were fed a regular diet.

Anesthetic was an isoflurane inhalation (1.5 - 2.0 Vol.%) in O₂ (1.5 - 2.0 L/min) applied by means of a nose cone. The isoflurane concentration was held as close to 1.7% as the animals allowed in order to minimize anesthetic induced deviations in the PWV measurements.

Mice were hung vertically (head up) in the TEM RF resonator (25mm inner diameter) by means of a flap of tape that was attached to their forelimbs. Mice's body temperature was maintained by regulating the gradient insert temperature control unit. The temperature of the unit was set to 37°C before mice were placed in the MR system and was lowered one minute prior to PWV measurements to 32°C to remove the heat that is produced by the active gradient insert. The temperature was set to 37°C at the end of the measurements.

All experimental procedures were in accordance with institutional guidelines and were approved by local authorities.

Nine two-point TT measurements were performed on the ApoE^(-/-) mice and eight on the C57Bl/6J mice. Two-dimensional FLASH experiments were leading the PWV measurements in order to position the imaging slices perpendicularly to the thoracic and the abdominal aorta (see Fig.4.4 on page 70).

The excitation angle of the RF pulse was empirically set to 40° so that the contrast between intravascular blood and stationary tissue was maximized (inflow effect). The time window to sample the late diastole and early systole was set to 40 ms. All other parameters of the measurement protocol were set as in the measurements on the vessel phantom.

The MR data were processed using the same MATLAB routine that was used for the analysis of the data acquired on the vessel phantom (section 5.1.4).

Differences in the mean PWV values of the two animal groups were tested by a single sided t-test for the hypothesis of equality against the alternative of a higher value for the ApoE^(-/-) group. A p-value < 0.05 was considered significant. In this work all PWV values are given as mean ± standard error (SE) unless otherwise noted.

5.1.4 Data Processing

The recorded MR data were interleaved to bring the data to the correct sequential order by the algorithm that was developed for the data analyzing software used for the PWV determination by flow wave measurements (section 4.1.2, page 66). Image interpolation and luminal area segmentation were performed using a graphical software running under MATLAB (The Mathworks, Inc., Natick, MA, USA) that was developed in the scope of this work. The workflow of the program is illustrated in Fig.5.2.

Besides the cross-sectional magnitude images of the descending murine aorta, the recorded data included a longitudinal scan of the aorta that was used to gauge the distance between the measurement locations. Therefore, straight-line interpolation along the luminal midline was performed in AMIRA (Visage Imaging, Inc., San Diego, CA, USA).

The k -space data of the cross-sectional aortic images were arranged in the correct temporal order, zero-filled, and fast Fourier transformed to form the interpolated images in position space.

In the magnitude images, luminal cross-sections were segmented manually in a time window of a length of 20 to 30 ms that spanned the late diastole and the early systole. In order to minimize the user error every segmentation was performed four times. After the segmentation, the software determined the distension waves and the standard deviation of the segmented areas. The distension waveforms were smoothed by repeated application of a moving average of width three. The number of repetitions varied from one to three, depending on the quality of the distension waves.

The TT of the distension waves was determined by the foot-to-foot method (section 2.2.4, page 40). The fit through the diastolic areas was selected manually. The start of the systolic fit region was determined automatically as the first data point of a series of three consecutive points that deviated from the diastolic fit by two standard deviations. The end of the systolic fit region was automatically determined when the magnitude of the first derivative of the area curve fell below one third of its maximum value. The systolic fit range could be corrected manually to exclude wave reflections and blurred feet (due to smoothing) of the distension waveform.

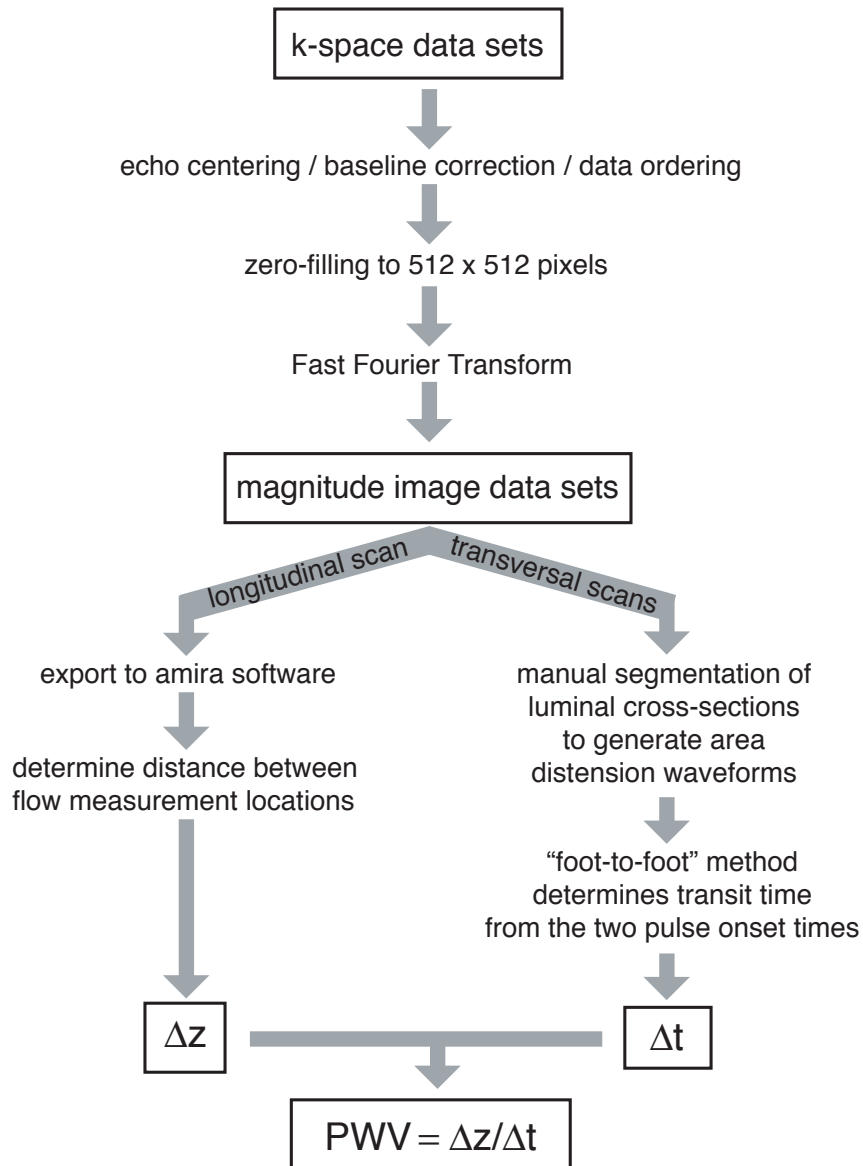


Figure 5.2: Workflow of the data analyzing software used to determine the PWV from arterial distension waveforms.

5.2 Results

5.2.1 Validation Experiments

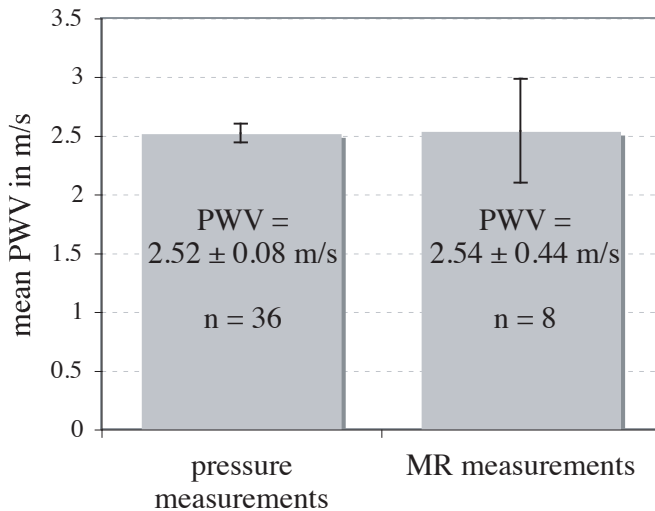


Figure 5.3: Mean distension waveform PWV in the phantom vessel measured with the MR method and the reference obtained by pressure catheter measurements. Values are given as mean \pm SE. **n** indicates the number of pressure measurements used for the multi-point TT method and the number of two-point TT MR measurements.

In the vessel phantom, the pressure catheter measurements yielded a $PWV = 2.52 \pm 0.08$ m/s (Fig.5.3). The MR distension waveform measurements determined a $PWV = 2.54 \pm 0.44$ m/s. Comparison of the PWV values of the pressure and MR measurements resulted in no significant difference ($p \leq 0.99$).

In order to assess the precision of the manual area segmentation, four segmentations were performed for every time frame and the standard deviation (SD) of the segmented areas normalized to the mean area was determined. This relative SD, averaged over all time frames and experiments, was 0.56%. The maximum relative SD of one experiment was 0.71% and the minimum was 0.41%. The variation of the segmentation depended on the effort that was put into the segmentation. The precision was highest when at least ten seconds were taken to encircle every luminal area.

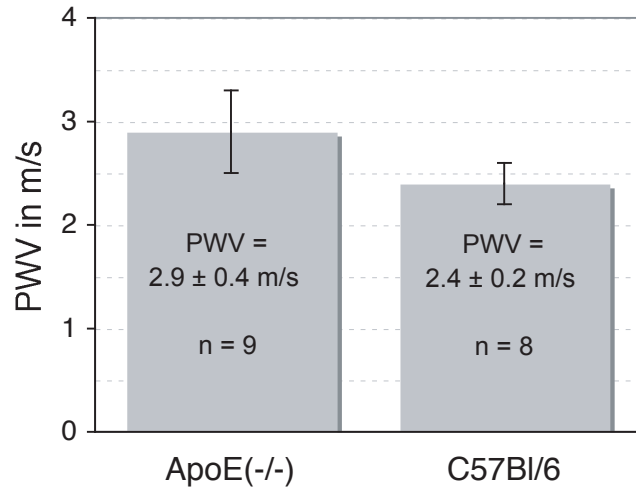
The area segmentation of all time frames in both imaging slices took approximately 27 minutes when 20 ms of the distension waveform had to be estimated by averaging four segmentations. Often a time window of 30 ms was used. This extended the segmentation time to 40 minutes.

5.2.2 In Vivo Experiments

The measured PWV values ranged from 1.5 m/s in a C57Bl/6J mouse to 4.9 m/s in an ApoE^(-/-) mouse. The average values of each animal group are $PWV = 2.9 \pm 0.4$ m/s

for ApoE^(-/-) mice and PWV = 2.4 ± 0.2 m/s for C57Bl/6J mice (Fig.5.4). The mean value of the ApoE^(-/-) group was significantly higher than that of the C57Bl/6J group only for p ≥ 0.09. For smaller p values a significant difference is not ascertainable.

Figure 5.4: PWVs of groups of eight-month-old ApoE^(-/-) and C57Bl/6J mice determined from distension waveforms. The ApoE^(-/-) mice received a western type diet 10 weeks prior to the measurements. The PWV values are given as mean ± SE. The number of measurements on each group is indicated by **n**.



Representative cross-sectional images of the thoracic and the abdominal aorta of an ApoE^(-/-) mouse are displayed in Fig.4.8. The images are clippings of the zero-filled cross-sectional images. The vessel distension is visible even though the distension is smaller than the nominal image resolution. Motion of the first order (constant velocity) was compensated by the MR sequence. In the upper thoracic aorta, turbulent blood flow and higher orders of motion, e.g., acceleration, cause motional artifacts. Due to the damping effect of the upper aorta these effects vanish in the images of the abdominal aorta.

The segmentation of luminal areas sometimes was complicated by displacement artifacts (section 2.1.4.1 on page 19) that result from non-perpendicular vessel angulation even though the imaging slices were positioned perpendicularly to the aorta by the use of a longitudinal reference scan. This is because the aorta moves with the beating heart. Also, intra-voxel dephasing artifacts (section 2.1.4.4 on page 28) that were caused by turbulent blood flow in the thoracic aorta made the segmentation of the lumen more difficult. Examples of the artifacts are shown in Fig.5.6.

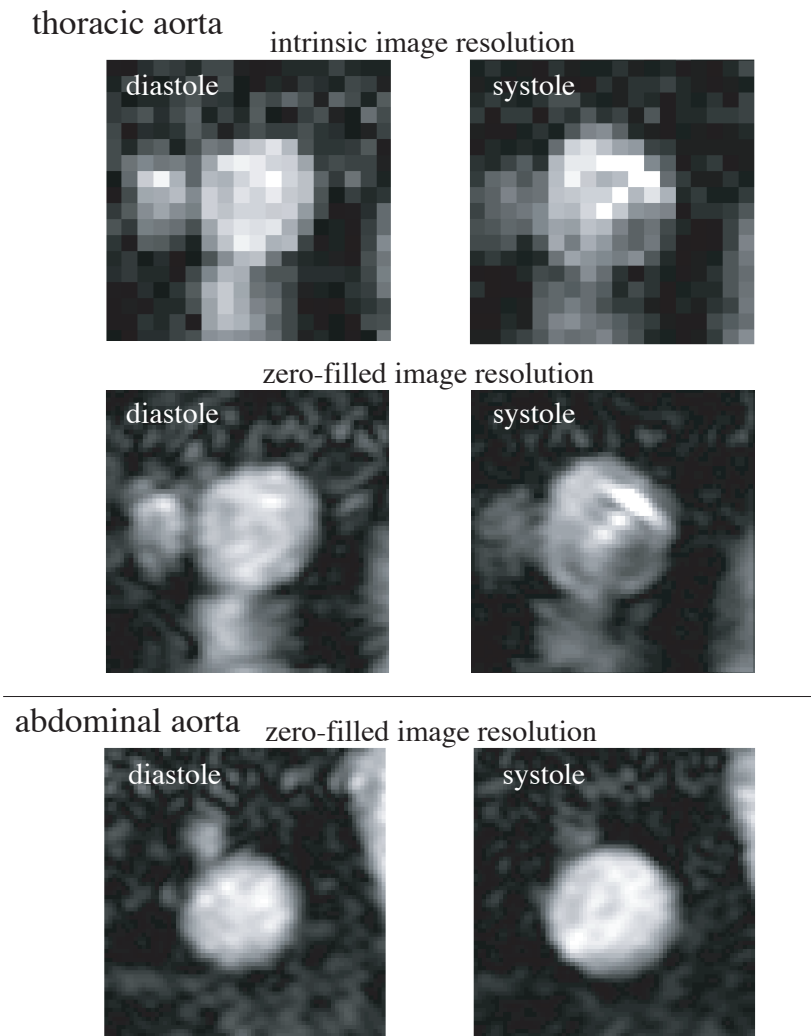


Figure 5.5: Clippings of axial scans of the aorta of an eight-month-old ApoE^(-/-) mouse. The scans are recorded at the end of the diastole and 20 ms later during the early systole at the locations of the descending thoracic aorta and the abdominal aorta. The vessel distension is visible in the zero-filled images even though the vessel distension is below the intrinsic image resolution. Artifacts due to higher orders of motion are visible in the systolic image of the thoracic aorta (the MR sequence compensates only motion of first order).

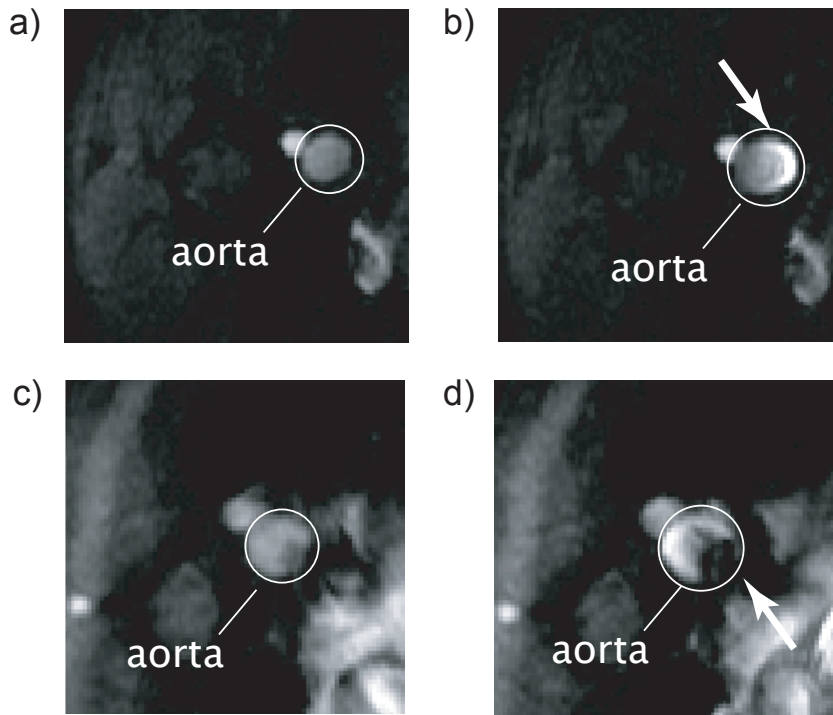


Figure 5.6: **a:** Diastolic cross-sectional image of the thoracic aorta of a mouse. Due to slow blood flow the displacement artifact does not appear. **b:** The displacement artifact (indicated by the arrow) is prominent during systolic flow. In this image it presents itself as a bright margin. The artifact can appear as alternating bands of bright and dark contrast for cases where the angle between the slice and flow vectors is larger than in this imaging experiment. **c:** Cross-sectional images of the descending aorta of a mouse show intra-voxel dephasing due to orders of motion that are higher than first order (higher than constant velocity). In the diastolic image the artifact does barely appear due to the slow blood flow. **d:** Strong turbulence causes intra-voxel dephasing during the systole. The signal intensity is diminished. The artifact is indicated by the arrow. The increased signal intensity on the left margin of the vessel is another example of the displacement artifact.

5.3 Discussion

5.3.1 Validation Experiments

The PWV of the vessel phantom was determined from transit times from distension waveforms and from pressure waveforms. The PWV values do not differ with statistical significance ($p \leq 0.99$).

The relative standard error of the pressure measurements is 3%. The precision corresponds to the precision of the reference measurements on the vessel phantom in chapter 4.

The relative standard error of the PWV that was obtained by the MR measurements in combination with the manual planimetry of intra-luminal areas is 17%. The precision of the single flow waveform PWV measurements from chapter 4 exceeds the precision of the distension waveform method by a factor of 1.4*. This suggests that the segmentation of intra-luminal areas is more prone to errors than the flow encoding and the determination of pulse onset times.

5.3.2 In Vivo Experiments

The precision of the distension waveform MR method was sufficient to distinguish between a group of five eight-month-old ApoE^(-/-) mice and a group of four age matched C57Bl/6J mice for $p \geq 0.09$ only. For $p = 0.05$ the difference of the mean PWV values is not significant. The flow waveform method from chapter 4 distinguished between animal groups with a p-value ≥ 0.007 . The precision of the flow waveform TT method surpasses that of the distension waveform TT method. The relative standard errors of both methods were 8% for the C57Bl/6J group but the relative standard error of the ApoE^(-/-) group was almost doubled when distension waveforms were analyzed. This is a result of the manual area segmentation that was complicated by stronger flow artifacts in the thoracic aorta of the ApoE^(-/-) mice.

As in the flow waveform TT method, the standard deviation of single experiments prevented the classification of single animals into one of the two animal groups.

The accuracies of the flow and distension waveform TT methods are the same because the mean PWV values determined by both methods agree. The difference lies within the precision of the methods. The correlation of the two MR measurement methods is shown in Fig.5.7.

*The relative standard deviations are considered.

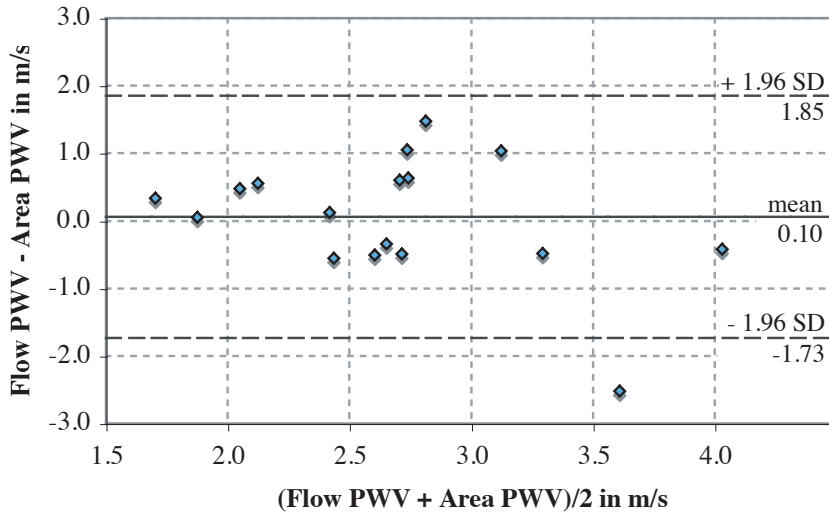


Figure 5.7: Bland-Altman plot [103] of the flow waveform PWV values and the distension waveform PWV values of all mice. The higher the PWV, i.e., shorter transit times, the larger are the deviations.

Summarizing the findings of the distension waveform TT measurements it can be concluded that the determination of the arterial PWV in mice by luminal area segmentation in zero-filled magnitude images is possible. This is due to the image contrast of the developed method. The contrast is sufficiently high and allows for a zero-filling to an image resolution where the motion of the luminal boundary could be detected. The phantom measurements showed that the method is accurate. The in vivo experiments showed that the accuracy of the method is equivalent to the flow waveform TT MR method. In comparison to the flow waveform TT method, the distension waveform method allowed for reduced in vivo experiment times of five to eight minutes. One drawback of the distension waveform TT method is the reduced precision. The standard error was so high that no significant difference between animal groups could be determined for $p < 0.05$. Another drawback is the lengthy manual post-processing, i.e., the area segmentation. Per animal, the segmentation time could be as high as one hour.

Chapter 6

The QA-Method

The TT method delivers a regional PWV value which is averaged over the propagation pathway in between the measurement locations. In early stages of atherosclerosis, diminutive vascular lesions are scattered along the aorta which affect the PWV locally. Therefore, interest of research is also on the local elastic properties of the murine aorta.

The QA method [16] was applied to mice [29] to determine local PWVs. The QA method uses the volume flow (Q) to cross-sectional area (A) relation during the early systole to calculate the PWV (section 2.2.5 on page 42). The QA method is unrivaled in local estimation of the PWV. However, in humans, Ibrahim et al. found that the flow encoded TT method is more robust and requires less user interpretation because it operates without the determination of cross-sectional areas [104].

In this chapter, the accuracy and the precision of the QA-method are tested on the vessel phantom that was presented in chapter 3 and on the same animal groups as in the chapters 4 and 5. The results of the in vivo measurements are compared to those of the TT methods.

6.1 Methods

In this part of the work, the flow encoding MR method that was developed for flow waveform measurements (chapter 4) was applied in combination with the zero-filling during the image data reconstruction and the consecutive planimetry of intra-luminal areas (chapter 5). Thus, the flow and distension waveforms of the early systole were obtained and estimates of local PWVs were determined.

6.1.1 Validation Experiments

Again, the MR method was validated under standardized conditions on the pulsatile elastic vessel phantom that was presented in chapter 3 on page 47. This time, flow and areal distension waveforms were recorded with the MR method. Multi-point TT catheter measurements of pressure waves provided the reference PWV value. The PWVs obtained by the two different measurement methods were compared to each other by a two-sided t-test for unpaired samples in order to give evidence of the accuracy of the MR method.

The reference data of the multi-point TT method is the same as in section 5.1.2 on page 87. That is thirty-six pressure time courses recorded with a pulse period of 1.8 s. The data was analyzed in MATLAB with the routine from section 3.1.3 on page 53.

The settings of the MR measurements are equivalent to those from section 5.1.2 on page 87, except for the active flow encoding gradients. The maximum first gradient moment was set to accommodate a flow-encoding window of $1/2 v_{max} = 0.20$ m/s. The bipolar flow encoding gradients were stepped from zero to maximum in three encoding steps. Thereto, the quality of the obtained velocity values could be assessed. Velocity values of pixels with an $R^2 < 0.85$ were replaced by the average velocity of the eight surrounding pixels.

Sixteen MR measurements were performed at measurement positions ± 7 mm in the longitudinal direction from the MR iso-center. MR data were timely interleaved, zero-filled to 512×512 pixels, areal distension waveforms were segmented, and the volume flow was determined. Data analysis was performed with a customly developed routine that runs under MATLAB (section 6.1.3).

6.1.2 In Vivo Experiments

The in vivo data from chapters 4 were analyzed to obtain the local PWVs. Eighteen QA measurements were performed at the thoracic and the abdominal aortas of the five female eight-month-old ApoE^(-/-) mice on the western type diet and sixteen measurements were performed on the four sex- and age-matched C57Bl/6J mice.

The MR data were processed using the same MATLAB routine that was used for the analysis of the MR data acquired on the vessel phantom (section 6.1.3).

Differences in the mean PWV values of the two animal groups were tested by a single sided t-test for the hypothesis of equality against the alternative of a higher value for the ApoE^(-/-) group. A p-value < 0.05 was considered significant. In this work all PWV values are given as mean \pm standard error (SE) unless otherwise noted.

6.1.3 Data Analysis

The recorded MR data were interleaved to bring the data to the correct sequential order by the algorithm that was developed for the data analyzing software used for the PWV determination by flow wave measurements (section 4.1.2, page 66). Image interpolation, i.e., the zero-filling to 512 by 512 pixels and luminal area segmentation were performed using a graphical software running under MATLAB (The Mathworks, Inc., Natick, MA, USA) that was developed in the scope of this work. The segmentation was performed in two ways; one was the manual segmentation that was applied in chapter 5, the other was an automated segmentation that used the 50% threshold of the maximal signal magnitude to assign pixels above that level to the lumen. The workflow of the program is illustrated in Fig.6.1.

The same time windows of the pulse wave of 20 to 30 ms length spanning the late diastole and early systole were utilized for the manual and automatic luminal area segmentations. After the segmentations, the distension waveforms were smoothed by repeated application of moving averages of width three. The number of the applied smoothing cycles varied from one to three, depending on the quality of the distension waves.

The volume flow was calculated inside the intra-luminal areas and plotted versus the intra-luminal areas. The fit through the early systolic region was selected manually. The slope yielded the local PWV.

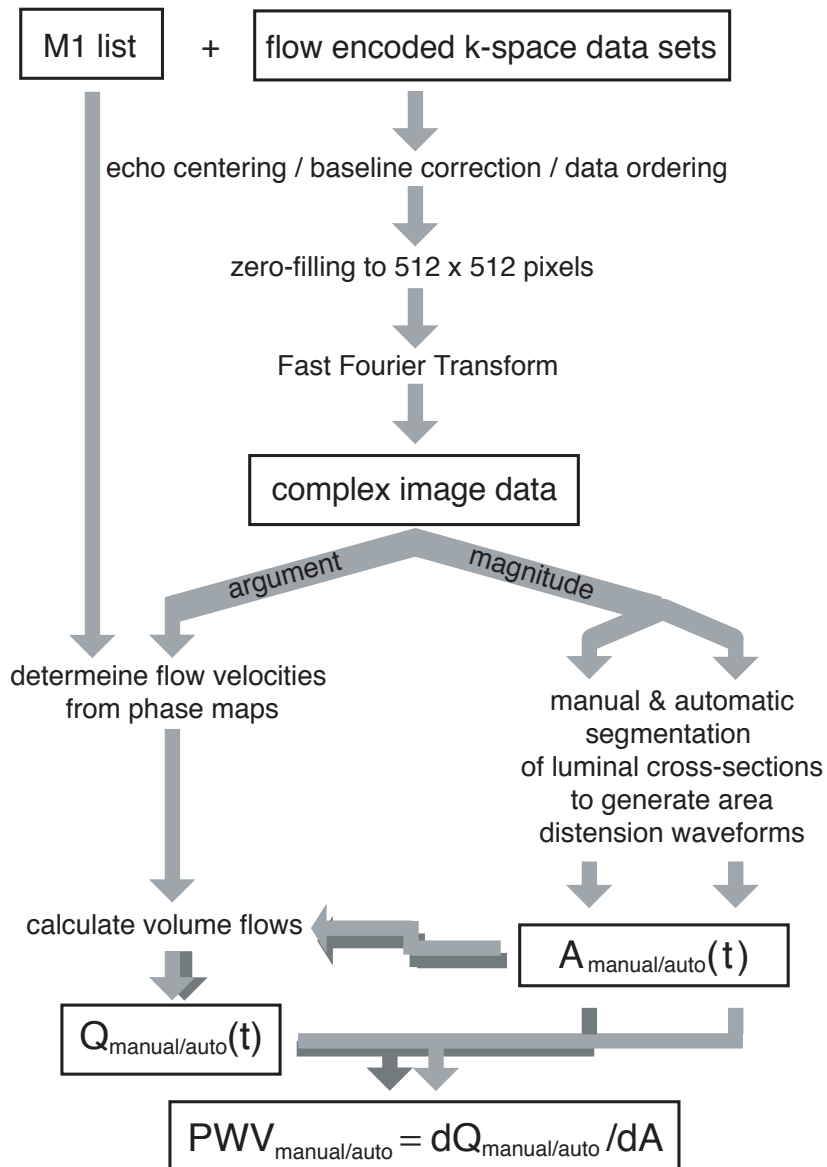


Figure 6.1: Workflow of the data analyzing software used to determine the PWV by the QA method.

6.2 Results

6.2.1 Validation Experiments

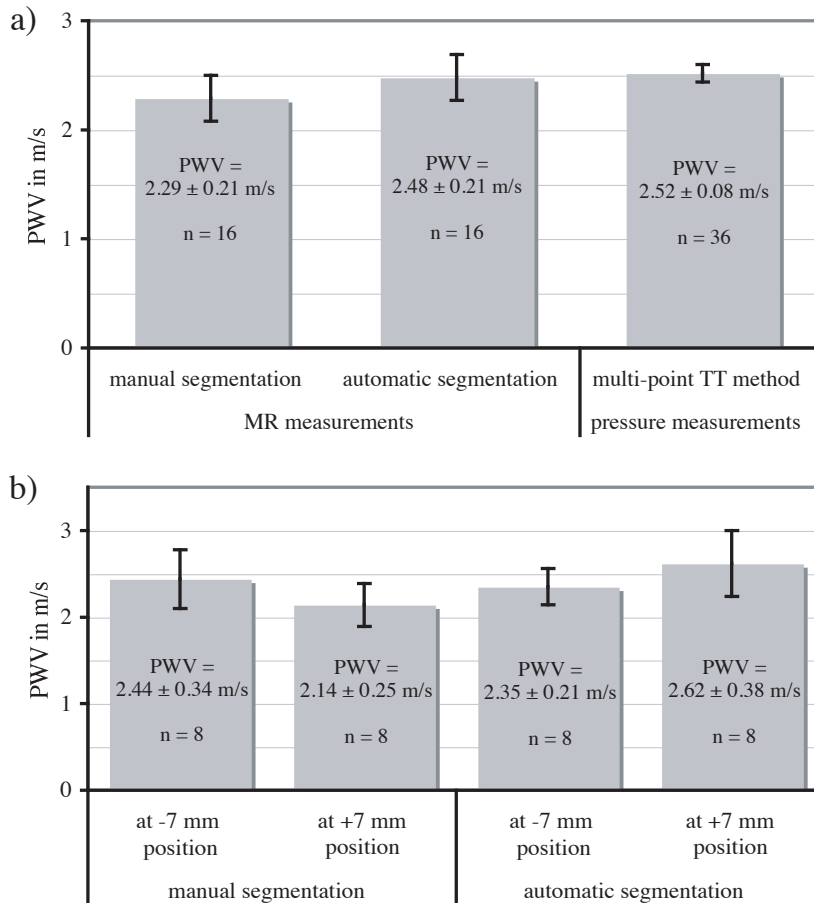


Figure 6.2: PWVs measured in the vessel phantom. **a)** For the MR measurements, local PWVs from the ± 7 mm positions from the iso-center are averaged and compared to the reference value that was obtained from multi-point TT pressure catheter measurements. Values are given as mean \pm SE. **n** indicates the number of pressure measurements and QA measurements. **b)** The local PWV values determined by the MR method at the ± 7 mm positions are shown for both segmentation methods.

In the vessel phantom, the pressure catheter measurements yielded a $\text{PWV} = 2.52 \pm 0.08$ m/s (Fig.6.2). The automatically segmented QA measurements (Fig.6.3) determined an averaged* $\text{PWV} = 2.48 \pm 0.21$ m/s. Comparison of the PWV values of the pressure and MR measurements resulted in no significant difference ($p \leq 0.99$).

The manually segmented QA measurements yielded a slightly lower averaged value: $\text{PWV} = 2.29 \pm 0.21$ m/s. Comparison to the reference value shows no significant difference for $p \leq 0.1$. For larger p-values the difference becomes significant.

Manual and automatic segmentation deliver approximately the same PWV at the lower measurement position (-7 mm). The difference is not statistically significant for $p \leq 0.99$.

*All 16 PWV values from the measurement locations ± 7 mm from the iso-center were averaged.

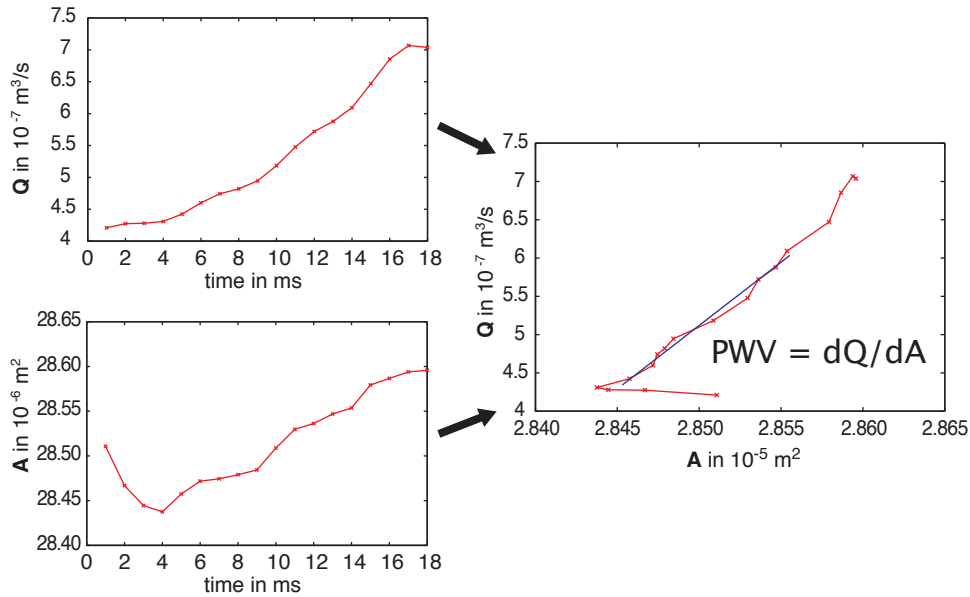


Figure 6.3: Measurements of volume flow Q and intra-luminal area A on the vessel phantom. The volume flow is plotted against the cross-sectional areas of the lumen. The flow and distension waves set in at approximately 4 ms. The slope of the linear regression through the early, reflection-free flow wave data points yields the PWV. This particular measurement is one of the eight automatically segmented measurements at the -7 mm position. It determined a $\text{PWV} = 1.64 \text{ m/s}$. The first four milliseconds of the area plot show the vessel contraction after the previous pulse.

At the +7 mm position, the automatic segmentation determines a higher PWV with statistical significance ($p \geq 0.004$).

The vessel material, PVA-C, is a gel and imposes no strict barrier for water. During the measurements the aqueous CuSO_4 solution slowly permeated the vessel wall. Subsequently, droplets formed on the outside of the vessel and rolled off after they reached a critical size. The droplets caused susceptibility artifacts in the images which affected the planimetry of luminal areas (Fig.6.4).

6.2.2 In Vivo Experiments

In vivo, only the manual luminal area segmentation was applicable due to a signal contrast between lumen and surrounding tissue that changes along the circumference of the artery and due to higher order motional artifacts in the magnitude images (Figs. 5.5 & 5.6 on pages 93 & 94).

For the $\text{ApoE}^{(-/-)}$ group, the QA method delivered the $\text{PWV}_{\text{thoracic}} = 2.3 \pm 0.3 \text{ m/s}$

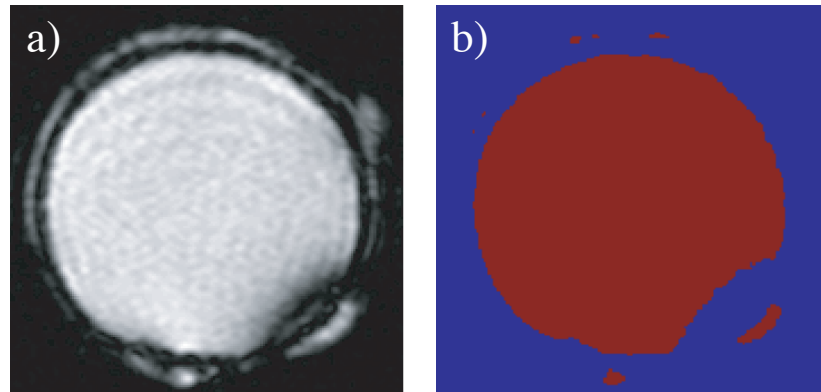


Figure 6.4: **a)** Cross-section of the vessel phantom with artifacts caused by droplets on the outside of the vessel wall. Droplets can form on the outside of the wall because the poly(vinyl-alcohol) cryogel allows fluid diffusion. The droplets provide signal and cause susceptibility artifacts. The wall by itself does not deliver signal. **b)** Example of an automatically generated areal segmentation of the lumen (signal intensity threshold was 50% of maximum) with deficits due to signal and susceptibility artifacts of droplets. The example shows the strongest artifacts that were encountered; in other MR scans they were less marked.

and $PWV_{abdominal} = 2.7 \pm 0.2$ m/s. For the C57Bl/6J group the local PWV values were: $PWV_{thoracic} = 2.0 \pm 0.2$ m/s and $PWV_{abdominal} = 1.8 \pm 0.2$ m/s. For the ApoE^(-/-) group, the $PWV_{thoracic}$ is lower than $PWV_{abdominal}$. For the C57Bl/6J group the relation is inverted. In general, the PWV is lower in the proximal aorta than in the distal aorta due to the windkessel function of intact aortas. The PWVs measured on the C57Bl/6J group did not confirm this fact.

At the thoracic aorta, the mean PWV value of the ApoE^(-/-) group is higher than that of the C57Bl/6J group but the values do not differ with statistical significance for $p \leq 0.23$. At the abdominal aorta, the PWV of the ApoE^(-/-) group is significantly higher than that of the C57Bl/6J group ($p \geq 0.006$).

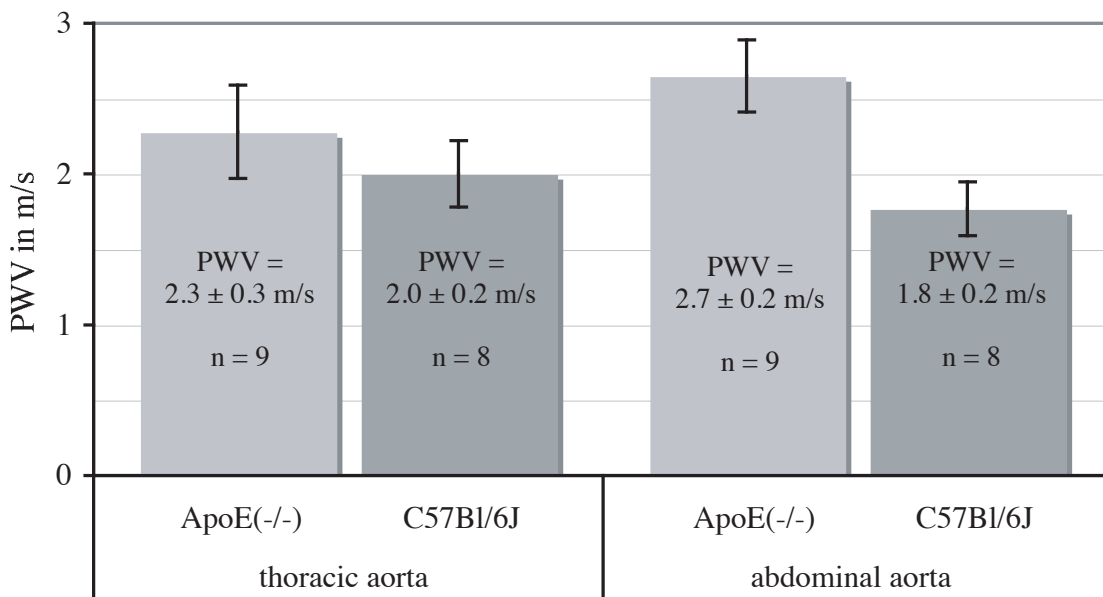


Figure 6.5: Mean PWVs of groups of eight-month-old ApoE^(-/-) and C57Bl/6J mice determined from distension waveforms. The ApoE^(-/-) mice received a western type diet 10 weeks prior to the measurements. The PWV values are given as mean \pm SE. **n** indicates the number of measurements. At the abdominal aorta, the PWV values of the two animal groups differ with statistical significance for $p \geq 0.006$. The difference is not significant at the thoracic aorta ($p \leq 0.23$).

6.3 Discussion

6.3.1 Validation Experiments

The PWV of the vessel phantom was determined locally by the QA MR method using automated and manual planimetry of the vessel lumen. Comparison of the PWV values obtained by the MR method and automatic segmentation with the value obtained by pressure catheter measurements showed no statistically significant difference ($p \leq 0.99$). The mean PWV value obtained by the manually segmented QA measurements is 9% below the reference. The difference is insignificant only for $p \leq 0.10$.

It can be concluded that the accuracy of the automatic segmentation method is sufficient despite the segmentation errors that are sometimes caused by droplets that formed on the outside of the vessel wall. The areal contribution of the droplets is constant and the velocity contribution of the droplets is zero. In theory, the droplets only cause an offset of the QA plot but they do not cause a change in slope and, accordingly, the PWV.

The accuracy of the manual segmentation method lies below that of the automatic segmentation. This is probably due to operator errors in the areal segmentation. Image artifacts that were caused by droplets could be compensated by the operator during the area segmentation but in turn other human errors were made in the segmentation.

The relative standard error of the PWV that was obtained by the MR measurements in combination with the manual planimetry of intra-luminal areas ranges from 12 to 14%. The relative standard error of the automatically segmented QA MR measurements ranges from 9 to 15%. Therefore the precisions of the two methods are comparable.

The precisions of the QA method (35% relative SD)[†] and of the flow waveform PWV measurements from chapter 4 (34% rel. SD) are approximately equal. This suggests that the flow encoding in combination with the segmentation of intra-luminal areas and volume flow determination is not more prone to errors than the flow encoding in combination with the determination of pulse onset times. This conclusion is in contradiction with the one in chapter 5 on page 95. There it is stated that the segmentation of intra-luminal areas were more prone to errors than the flow encoding and the determination of pulse onset times. Therefore, it is concluded that more than eight QA and distension waveform TT measurements are needed to compare the precisions of the two methods.

In chapter 3 it was found that the PWV increases by 0.026 m/s per additional mil-

[†]Relative standard deviations (SD) are considered. The rel. SD of the two segmentation methods and the two measurement locations are averaged.

limeter water column above the measurement location (Fig.3.8a on page 57). The QA measurements were performed with a slice separation of 14 mm and, therefore, the PWV at the + 7 mm position should be 0.36 m/s lower than at the - 7 mm position. This offset is in the range of the standard errors of the QA methods. The automatically segmented QA method measured a difference of 0.30 m/s. The manually segmented QA measurements were not able to resolve this difference; the measured offset was -0.27 m/s.

In general, it can be said that the precisions of all three developed MR methods (flow waveform TT, distension waveform TT, and QA) are roughly the same. The accuracy of the manually segmented QA method is lower than that of the other methods because the mean PWV values are 9% lower than the reference, whereas, the other methods agree well with the reference values. The automatically segmented QA method also has the advantage over the manually segmented method that the data analysis is a lot faster.

6.3.2 In Vivo Experiments

The in vivo experiments show that the local determination of the PWV in the descending murine aorta is possible when the intra-luminal areas are segmented manually. The automatic segmentation method that is based on the image contrast was not applicable due to anatomical features surrounding the aorta and due to higher order motional artifacts (Figs. 5.5 & 5.6 on pages 93 & 94). The extended data analysis duration (up to one hour per data set) due to the manual area segmentation has to be accepted for in vivo experiments.

In the abdominal aorta, the measured PWV of the ApoE^(-/-) group is higher than that of the C57Bl/6J group with a statistical significance of $p \geq 0.006$. The precision is comparable to the flow waveform TT method.

In the thoracic aorta, i.e., in proximity to the heart, the pulsatile blood flow has not been sufficiently moderated by the windkessel effect of the proximal aorta. Turbulence, i.e., randomly varying acceleration and higher orders of motion, caused flow artifacts that falsified the velocity information of afflicted pixels and complicated the manual area segmentation. The use of three flow encoding steps allowed for the identification of pixels with erroneous velocity information. Pixel velocity was replaced by the average of the surrounding eight pixels when the R^2 of the linear regression through the three phase values was below 0.85. Still, at the thoracic aorta the precision of the QA method was insufficient to distinguish between the group of five eight-month-old ApoE^(-/-) mice and the age matched group of four C57Bl/6J mice. The difference is statistically significant for $p \geq 0.24$ only. The results show that higher order motional artifacts were minimized

but not eliminated by the application of the shortest possible echo time.

The accuracy of the QA method is affected by uncertainties in the volume flow determination due to partial volume effects. For non-symmetric phase distributions and varying signal intensities from spins within a voxel, the average voxel phase is no more proportional to the mean voxel velocity. Errors in volume flow due to partial volume effects in phase difference MR measurements were quantified by Wolf et al. [105]. For radially symmetric parabolic flow profiles, the following equation describes the error in measured volume flow:

$$\epsilon_{flow} = 2\pi(f \Delta x)^2 v_p \left[\frac{g}{1 + f(g - 1)} - 1 \right] \left[1 - \frac{2f \Delta x}{2D} \right] \quad (6.1)$$

with $g = \frac{M_v}{M_s}$ and $f = \frac{N_v}{N_v + N_s}$.

The error depends on the peak flow velocity in the center of the flow profile v_p , the vessel diameter D , the image resolution Δx , the magnetizations and numbers of moving and static isochromats within an edge voxel M_v , M_s , and N_v , N_s .

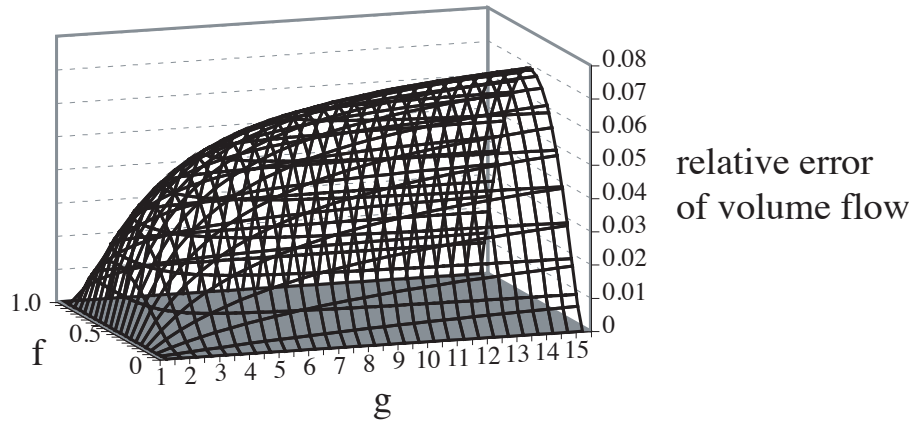


Figure 6.6: Relative error of volume flow due to the partial voluming effects on isochromat magnetization when measured with a phase difference MR method (according to [105]). The parameters used here are: $\Delta x = 0.147$ mm and $D = 1.0$ mm.

With the parameters $\Delta x = 0.147$ mm and $D \approx 1$ mm as they were in this study, the relative error of volume flow can be estimated to stay below 7% (Fig.6.6). The maximum overestimation of the volume flow is reached when the major contribution to the magnetization of edge pixels is made by moving isochromats and the edge pixels contain equal amounts of stationary and moving isochromats.

Another systematic error source is non-perpendicular vessel intersection. Theoretically, it has no effect on the volume flow because measured flow velocities decrease with $\cos(\theta)$

and cross-sectional areas increase with $1/\cos(\theta)$, where θ is the angle between the vessel axis and the perpendicular to the imaging slice. However, because the cross-sectional area depends on θ the measured PWV will be underestimated by $\cos(\theta)$. Theoretically, for a misalignment of 5° the deviation is below 0.4%. Numerical analysis by Wolf et al. showed that the relative error in volume flow is less than 1% for $\theta = 5^\circ$ when vessel diameter and imaging slice thickness are comparable, as it is the case in the in vivo measurements of this work.

A third error source is human error in the area segmentation. For example, an underestimation of one pixel around the lumen (zero-filled image resolution) results in a 17% underestimation of luminal areas. So if, for example, the systolic luminal area is segmented correctly but the diastolic luminal area is underestimated due to a lack in signal contrast (the inflow effect has not set in), the measured PWV will be underestimated, too.

Regionally averaged local PWV values (averages of the local thoracic and abdominal PWV values) deviate from the results obtained by the flow and distension waveform measurements by -16% and -21% for the ApoE^(-/-) and C57Bl/6J groups, respectively. The manually segmented QA measurements on the vessel phantom underestimated the reference value by 9%. The automatically segmented QA method did not show this deviation to the reference value on the phantom. Therefore, the offsets of the manually segmented QA method are assumed to be a result of systematic human errors in the manual segmentation.

Although the accuracy of the local PWV measurements in mice is limited, the values measured at the abdominal aorta can distinguish between animal groups. Therefore, the local PWV that is determined by the QA method can be used as a parameter to describe local vascular function despite the limited accuracy.

The manual area segmentation and higher order flow artifacts contribute to the statistical error of the local PWV. The flow waveform TT method sufficed without planimetry and without volume flow determination. There, the flow velocity measurements were relatively insensitive to accelerated blood flow and higher orders of motion because only the time points of the feet of the flow waveforms had to be determined. The experiments showed that in comparison to the results of the flow waveform TT method, the additional error sources of the QA method were not noticeable at the abdominal aorta. The standard errors were almost equal. However, flow artifacts and a more difficult area segmentation were noticeable in the thoracic aorta and showed their effects on the PWV. In the thoracic aorta of the examined ApoE^(-/-) mice the standard error was increased by almost 30%.

Summarizing the results of this chapter it can be said, that the QA method could be used in vivo to distinguish between atherosclerotic and healthy groups of animals when higher order flow artifacts were moderate. The precision of the local determination of

arterial PWV was comparable to flow waveform TT measurements but the QA method was not as robust when faced with higher order motional artifacts in the thoracic aorta. The distension waveform TT method showed the same proneness. The method also relies on the planimetry of the thoracic aorta. In comparison to flow and distension waveform TT measurements, the accuracy of the QA method showed a systematic deviation of the PWV when manual segmentation of the lumen was applied. The most likely origin of the errors is of human nature.

Chapter 7

Summary

In the broadest sense, the goal of this work was to enhance the research methods of cardiovascular diseases. Particularly, analytical in-vivo methods to assess a functional parameter of the arterial system that describes states of atherosclerosis in a murine animal model of human atherosclerotic disease, the ApoE^(-/-) mouse, were to be developed. The methods have to assure repeated applicability to the animals, i.e., they must be non-invasive in order that long term progression studies can be performed on the animals.

Arterial stiffening is etiologic in atherosclerosis and serves as an early marker for the disease. Interdependent markers for arterial elasticity are, e.g., the arterial compliance, the distensibility, and the Pulse Wave Velocity (PWV). The compliance and distensibility are defined as the vascular cross-sectional area or volume changes per unit change in transmural pressure. The propagation velocity of a wave in a fluid-filled elastic vessel that is induced by pressure changes is termed the PWV. The PWV increases with the stiffness of the vessel wall. It was the marker of choice in this work because it can be determined by MR measurements of intra-luminal blood flow velocities and vascular cross-sectional areas. Intra-luminal pressures are not needed for the determination.

The challenges for studies of arterial function and morphology in mice are the minute dimensions of the organs (approximately 20 times smaller than in humans) and the high heart rates of 500 to 600 beats per minute. Because the measurements are to be performed on anesthetized live animals without harming them the total experiment time must stay below two hours per animal. Heart rate, breathing period, and body temperature must be held at physiologic levels throughout the experiment time.

High-field MRI was the examination method of choice because it is non-invasive and delivers highly resolved two- and three-dimensional images of soft tissue with manifold contrasts, e.g., contrast based on velocities. The used Bruker AVANCE 750 MRI system with a static magnetic field of 17.6 T delivered the necessary Signal-to-Noise Ratio (SNR)

to record the data in sufficiently short experiment times.

Three different *in vivo* MR methods to measure local and regional PWVs were developed. The methods measure transit times (TT) of flow or distension waveforms and the volume flow (Q) to luminal area (A) relation to determine the PWVs locally (QA method). Manual planimetry of luminal areas was applied for the distension waveform method. Segmentation for the QA method was additionally automated.

In the scope of this work, a spatially and temporally highly resolving NMR sequence based on a CINE-FLASH sequence was developed. MRI data is acquired from two imaging slices positioned perpendicularly to the thoracic and the abdominal aorta. First order phase velocity encoding in the through-slice direction and the phase difference method were used for the measurement of intra-luminal blood flow velocity distributions with the spatial resolution of the MR image (see section: 2.1.4.3 on page 27). Velocity compensated gradient switching schemes are applied in the remaining spatial dimensions. The developed sequence provides a spatial resolution of $147 \times 147 \mu\text{m}^2$ and an echo time (TE) of 1.5 ms. The repetition time (TR) and, therefore, the intrinsic temporal resolution of the velocity data is 5 ms. *In vivo* acquisition times range from 5 to 25 minutes for the different measurement methods.

The necessary temporal resolution of 1 ms was achieved by the development of an interleaved data acquisition scheme. Thereto, a set of five data streams each delayed by one millisecond are acquired. The temporal resolution relies on the precise heart trigger signals that are provided by a triggering unit that was built in the department and a pneumatic heart / breath signal tap.

The determinability of the PWV relies on the constancy of mice's heart periods throughout the experiment time. It was found that variations must be below 5 ms. Heat that is dissipated by the gradient system during data acquisition may change the body temperature and, thus, the heart period of the mice. A protocol to control the gradient tempering unit was developed empirically.

To validate the MR methods, a pulsatile elastic vessel phantom made of poly(vinyl alcohol) cryogel was developed. A custom-built pulse generator induced pulse waves in the vessel that were analyzed using the MR methods and pressure catheter measurements for reference.

Software programs were developed for the data analysis of each measurement technique. Graphical graphical user interfaces facilitate the analysis for users who are not familiar with the basic modules of data analysis. Therefore, data can be analyzed as a matter of routine in future animal studies.

The pressure and MR validation measurements on the vessel phantom acknowledged

high accuracies for the flow and distension waveform TT methods and for the QA method that applied automatic intra-luminal area segmentation. The manually segmented QA method underestimated the reference PWV by 9% due to user errors in the manual segmentation. On the phantom, the precisions of the flow waveform method (34% relative standard deviation) and QA methods are the highest (manual segmentation: 36% rel. SD, automatic segmentation: 33% rel. SD). The distension waveform TT method (49%) shows lower precision.

To test the MR and data analysis methods for the suitability for in-vivo studies, they were applied to measure the PWVs of a group of five eight-month-old ApoE^(-/-) mice that received a fatty diet and a group of four age matched C57Bl/6J mice.

The findings of this work demonstrate the feasibility of the non-invasive in vivo determination of regional and local PWV values in descending murine aortas by the TT and QA methods using high-field MRI.

The regional flow and distension waveform TT measurements on the ApoE^(-/-) mice yielded mean PWVs of 3.0 ± 0.2 and 2.9 ± 0.4 m/s, respectively. Higher order motional artifacts in the thoracic aorta complicated the vessel planimetry and increased the error of the distension waveform TT method. For the C57Bl/6J group, both methods delivered mean PWVs 2.4 ± 0.2 m/s. Flow was more moderate in C57Bl/6J mice. Therefore, the two methods showed equal precisions. Both methods have equal accuracies. The mean PWVs of the animal groups differ with statistical significance* only for flow waveform TT measurements.

Only the manually segmented QA method was applicable in vivo; mainly due to circumferentially changing image contrast between lumen and extravascular tissue. On average the locally measured PWV values were 19% below the regional PWV values. Offsets were mainly caused by the user during the area segmentation. The precision was comparable to that of the flow waveform TT method except for the measurements at the thoracic aorta of the ApoE^(-/-) mice. Here higher order motional artifacts increased the standard error by almost 30%. PWV differences between the animal groups were statistically significant at the abdominal aorta only. Despite the limited accuracy, the local PWV may serve as a marker for vascular function of the distal murine aorta.

The PWV values, measured by the TT methods, are 12 to 43% lower than values obtained by pressure catheter and doppler ultrasound measurements on mice that are stated in the literature. Causes might be the differences in the used animals, the measurement techniques, effects of the anesthetic, or animal positioning. PWV values of single animals

*In this work a p-value < 0.05 marked differences with statistical significance.

cannot be used to make a statement about the group membership of the animals because the standard deviation of one single measurement is too large.

The body weight of the examined animals had to be limited to below 35 g. Heavier mice tightly filled the RF resonator and the measured PWV values varied highly. The cause-and-effect chain is unknown. It is surmised that the constriction might have induced stress and alterations of blood pressure or vascular tone which influence the PWV.

The PWV complements the set of MR-appraisable morphologic parameters describing the murine arterial system to form a comprehensive set. The developed method can be applied to mice repeatedly and, therefore, allows for long term studies. Now the method has to prove its value in the practical application and, hopefully, it will turn out to be a contribution to the enhancement of the research methods of cardiovascular diseases.

Chapter 8

Zusammenfassung

Kardiovaskuläre Erkrankungen sind derzeit die häufigste Todesursache. Im Jahre 2002 waren 29,3% der weltweiten Todesfälle auf kardiovaskuläre Erkrankungen zurückzuführen [1]. In Industrienationen ist der Anteil der Todesfälle durch kardiovaskuläre Erkrankungen noch größer. In Deutschland betragen die Ausgaben für die Behandlung von kardiovaskulären Erkrankungen ein Sechstel der Gesamtkosten des Gesundheitswesens des Jahres 2002 [2].

Das Augenmerk der medizinischen Forschung liegt derzeit auf molekularen und zellbiologischen Methoden der Diagnose und Therapie. Hierbei ist die Aufklärung der Zusammenhänge zwischen molekularbiologischen Prozessen, der Pathologien und den Krankheitsverläufen von besonderer Bedeutung. Hierzu werden Tiermodelle der kardiovaskulären Erkrankungen auf molekularer und zellulärer Ebene phenotypisiert. Außerdem sind aber in vivo Untersuchungen an intakten Tieren wichtig, um kardiovaskuläre Erkrankungen umfassend zu charakterisieren.

Das Ziel dieser Arbeit war die Erweiterung der nicht-invasiven Untersuchungsmethoden kardiovaskulärer Erkrankungen an Mäusen. Dazu wurden in vivo Methoden zur Untersuchung eines funktionellen Parameters, der PWV, welche den Krankheitsverlauf der Atherosklerose an einem Mausmodell menschlicher Atherosklerose, der ApoE^(-/-)-Maus, beschreibt, entwickelt. Die Methoden sind wiederholt anwendbar, ohne den Tieren zu schaden. Sie sind nicht-invasiv und ermöglichen Langzeitstudien des Krankheitsverlaufes.

Die Versteifung der Arterien ist charakteristisch für den frühen Krankheitsverlauf der Atherosklerose und dient als Erkennungszeichen der Krankheit. Messgrößen der Gefäßelastizität sind zu Beispiel die Komplianz (Nachgiebigkeit), die Distensibilität (Dehnbarkeit) und die Pulswellengeschwindigkeit (im Englischen: Pulse Wave Velocity, kurz PWV). Die Parameter hängen voneinander ab. Komplianz und Distensibilität sind definiert als Quotient aus Querschnittsflächen- oder Gefäßvolumenänderung und Druckänderung. Die PWV

ist die Ausbreitungsgeschwindigkeit einer Druck- und Flusswelle die durch Druckpulse auf einem flüssigkeitsgefüllten, elastischen Schlauch induziert wurde. Sie steigt mit zunehmender Gefäßversteifung. Die PWV wurde als indirekter Messparameter für die Gefäßelastizität gewählt, da ihr regionaler Mittelwert durch Erfassung der Blutflussgeschwindigkeiten und der Gefäßquerschnittsflächen bestimmt werden kann. Messungen intravaskulärer Drücke sind nicht erforderlich.

Winzige Größenordnungen der murinen Organe (ca. zwanzigfach kleiner als beim Menschen) und hohe Herzschlagraten von 500 bis 600 Schlägen pro Minute sind Herausforderungen für Untersuchungen arterieller Gefäßfunktion und -morphologie an Mäusen. Messdauern an lebenden, narkotisierten Tieren sollen maximal zwei Stunden betragen, damit die Tiere nicht geschädigt werden. Die Herzschlagrate, Atemfrequenz und Körpertemperatur müssen während der Messdauer auf physiologischen Werten gehalten werden.

Hochfeld-MRI wurde als Untersuchungsmethode gewählt. Sie ist nicht-invasiv und liefert zwei- und dreidimensionale Bilddatensätze von Weichteilgewebe mit vielfältigen Kontrasten, z.B. aufgrund von Bewegung. Das verwendete Bruker AVANCE 750 MRI-System mit einer statischen Magnetfeldstärke von 17,6 T lieferte ein hohes Signal-zu-Rausch-Verhältnis, welches das nötige räumliche Auflösungsvermögen in ausreichend kurzen Messzeiten ermöglicht.

In dieser Arbeit wurden verschiedene Methoden zur Messung der regionalen und lokalen Pulswellengeschwindigkeiten entwickelt, die auf der Messung der Transitzeiten von Fluss- und Dehnungswellen oder auf den lokalen Messungen von Volumenfluss und Querschnittsflächen (QA-Methode) basieren. Zur Messung hochaufgelöster, intravaskulärer Geschwindigkeitsverteilungen wurden geschwindigkeitskodierte MRI und die Phasendifferenzmethode verwendet (siehe Abschnitt 2.1.4.3 auf Seite 27). Die vaskulären Querschnittsflächen wurden für die Dehnungswellenmessung manuell segmentiert. Für die QA-Methode wurde zusätzlich eine automatische Segmentierung getestet.

Im Rahmen dieser Arbeit wurde eine zeitlich und räumlich hochauflösende MR-Sequenz basierend auf einer CINE-FLASH Methode zur Messung von Gefäßdehnungen und der Flussgeschwindigkeiten entwickelt. Die MRI-Daten werden in zwei Bildgebungsschichten akquiriert, die senkrecht zur thorakalen und zur abdominellen Aorta plaziert werden. Bewegungskodierung erster Ordnung wurde in der Richtung senkrecht zur Bildgebungsschicht angewendet, um die Signalphase des komplexen MRI-Signals in Abhängigkeit der Blutflussgeschwindigkeit zu kodieren. In den nicht flusskodierten Richtungen wurden Bewegungskompensierte Gradientenschaltsequenzen verwendet. Die entwickelte Sequenz liefert eine räumliche Auflösung von $147 \times 147 \mu\text{m}^2$ und eine Echozeit (TE) von 1,5 ms. Die Repetitionszeit (TR) und somit die intrinsische zeitliche Auflösung der Sequenz liegen

bei 5 ms. Abhängig von der Messmethode dauern in vivo Aufnahmen zwischen 5 und 25 Minuten.

Die benötigte Zeitauflösung von 1 ms wurde durch die Entwicklung eines verschachtelten Datenakquisitionsschemas erreicht. Dazu werden fünf um je 1ms verschobene Datenströme akquiriert. Die Genauigkeit der zeitlichen Auflösung hängt von präzisen Herztriggersignalen ab, die von einer am Lehrstuhl gebauten Triggereinheit in Verbindung mit einem pneumatischen Herz- und Atemsignalabgriff geliefert wurden.

Während der Aufnahme darf sich die Herzperiode um nicht mehr als 5 ms ändern. Wärme, die während des Experiments vom Gradientensystem abgestrahlt wird, kann die Körpertemperatur und die Herzperiode verändern. Ein empirisch ermitteltes Protokoll zur Temperatursteuerung des Gradientensystems gewährleistete Herzperioden im Toleranzbereich.

Zur Validierung der MR-Methode wurde ein pulsatile, elastisches Gefäßphantom aus Polyvinylalkohol-Kryogel entwickelt. Ein eigens dafür konstruierter Pulsgenerator erzeugte auf dem Gefäß Pulswellen, die mittels MR-Methode und Druckkathetermessungen (zur Validierung) untersucht wurden.

Zur Datenauswertung wurden für jede Messmethode Softwaremodule entwickelt. Die Softwaremodule verwenden graphische Oberflächen, um routinemäßige Datenauswertung im Rahmen zukünftiger Tierstudien zu ermöglichen, ohne dass der Anwender mit den Grundbausteinen der Datenauswertung vertraut sein muss.

Die Validierungsmessungen am Gefäßphantom bestätigten hohe Genauigkeiten für die Fluss- und Dehnungswellen Transitzeit Methoden und für die automatisch segmentierte QA-Methode. Die manuell segmentierte QA-Methode unterschätzte die PWV im Mittel um 9% aufgrund von Bedienerfehlern während der Segmentierung. Die Flusswellen-Transitzeit-Methode (relative Standardabweichung (SD) = 34%) und die QA-Methoden (manuell segmentiert: rel. SD = 36%; automatisch segmentiert: rel. SD = 33%) zeigten die größte Präzision. Die Präzision der Dehnungspulsmethode war geringer (rel. SD = 49%).

Um die Eignung der MR- und der Auswertemethoden für in vivo Studien zu testen, wurden die Pulswellengeschwindigkeiten an einer Gruppe aus fünf achtmonatigen ApoE^(-/-)-Mäusen, die eine fettreiche Diät bekamen, und an einer Gruppe aus vier gleichaltrigen C57Bl/6J-Mäusen gemessen.

Die Ergebnisse dieser Arbeit demonstrieren die Durchführbarkeit von nichtinvasiven in vivo Messungen der regionalen und lokalen Pulswellengeschwindigkeiten an der absteigenden murinen Aorta mittels TT- und QA-Methoden und Hochfeldmagnetresonanz.

Die regionalen Fluss- und Dehnungswellenmessungen lieferten an den ApoE^(-/-)-Mäusen mittlere Pulswellengeschwindigkeiten $PWV = 3,0 \pm 0,2$ und $2,9 \pm 0,4$ m/s. Bewegungs-

artefakte höherer Ordnungen erschwerten die Segmentierung der Gefäßquerschnitte und erhöhten dadurch den Fehler der Dehnungswellenmessungen. Für die C57Bl/6J-Gruppe ermittelten beide Messmethoden mittlere PWVs = $2,4 \pm 0,2$ m/s. Die Fehler gleichen sich, denn der Blutfluss weist in C57Bl/6J-Mäusen weniger Turbulenzen auf. Die mittleren PWVs der Tiergruppen unterscheiden sich mit statistischer Signifikanz*.

Nur die manuell segmentierte QA-Methode war in vivo anwendbar, da der Bildkontrast entlang des Gefäßumfangs variierte. Durchschnittlich lagen die lokal gemessenen PWV-Werte 19% unter denen der Transitzeitmethoden. Die systematischen Abweichungen resultieren hauptsächlich aus Fehlern bei der manuellen Segmentierung. Bis auf Messungen an der thorakalen Aorta der ApoE^(-/-)-Mäuse war die Präzision vergleichbar mit der Flusswellenmethode. Bewegungsartefakte höherer Ordnungen verstärkten den relativen Fehler um fast 30%. Unterschiedliche PWV-Werte konnten für die Tiergruppen nur in der Bauchaorta gemessen werden. Trotz der systematischen Abweichungen, kann die PWV in der distalen murinen Aorta als funktioneller vaskulärer Parameter verwendet werden.

Die mit den Transitzeitmethoden gemessenen PWV-Werte sind 12 bis 43% niedriger als Literaturwerte die mit Druckkathetern und Doppler-Ultraschall gemessen wurden. Ursachen dafür können die Unterschiede in den verwendeten Tieren, den Messmethoden, der Tierlagerung oder den Wirkungen des Anesthetikums darstellen. Die Pulswellengeschwindigkeit einzelner Tiere kann nicht herangezogen werden, um Aussagen über die Gruppenzugehörigkeit zu treffen, da die Standardabweichung der Einzelmessung zu hoch ist.

Die Körpermasse der untersuchten Tiere muss unter 35 Gramm liegen. Schwerere Tiere wurden vom RF-Resonator eingengt und die gemessenen PWV-Werte wiesen starke Schwankungen auf. Die Ursachen dafür sind unbekannt. Es wird vermutet, dass die Eingenkung der Tiere Stress, Blutdruckschwankungen oder Änderungen des arteriellen Tonus verursachte, welche die PWV beeinflussten.

Die MR-Methoden zur Erfassung der PWV erweitern die Gruppe der Gefäßparameter zur Beschreibung des murinen arteriellen Systems zu einem umfassenden Parametersatz. Die entwickelten Methoden können an ein und demselben Tier mehrfach angewendet werden, wodurch Langzeitstudien ermöglicht werden. Nun müssen sich die Methoden in der praktischen Anwendung bewähren und werden hoffentlich zu einer Bereicherung der Untersuchungsmethoden kardiovaskulärer Erkrankungen.

*In dieser Arbeit werden Differenzen mit statistischer Signifikanz für p-Werte < 0,05 angenommen.

Bibliography

- [1] World Health Organization. World Health Report 2004: changing history. Available at <http://www.who.int/whr>
- [2] Böhm K, Cordes M, Forster T, Krah K in Zusammenarbeit mit Mitarbeiterinnen und Mitarbeitern der Gruppe VIII A des Statistischen Bundesamtes. Bericht „Krankheitskosten 2002“. Statistisches Bundesamt - Pressestelle, Wiesbaden, Germany, 2004.
- [3] Stergiopoulos N, Segers P, Westerhof N. Use of pulse pressure method for estimating total arterial compliance in vivo. *Am J Physiol* 1999;276(2 Pt 2):H424-428.
- [4] Arnett DK, Evans GW, Riley WA. Arterial stiffness: a new cardiovascular risk factor? *Am J Epidemiol* 1994;140(8):669-682.
- [5] Laurent S, Cockcroft J, Van Bortel L, Boutouyrie P, Giannattasio C, Hayoz D, Pannier B, Vlachopoulos C, Wilkinson I, Struijker-Boudier H. Expert consensus document on arterial stiffness: methodological issues and clinical applications. *Eur Heart J* 2006;27(21):2588-2605.
- [6] Callaghan FJ, Geddes LA, Babbs CF, Bourland JD. Relationship between pulse-wave velocity and arterial elasticity. *Med Biol Eng Comput* 1986;24(3):248-254.
- [7] Laurent S, Katsahian S, Fassot C, Tropeano AI, Gautier I, Laloux B, Boutouyrie P. Aortic stiffness is an independent predictor of fatal stroke in essential hypertension. *Stroke* 2003;34(5):1203-1206.
- [8] Bramwell JC, Hill AV. Velocity of transmission of the pulse-wave and elasticity of arteries. *The Lancet* 1922;199(5149):891-892.
- [9] Latham RD, Westerhof N, Sipkema P, Rubal BJ, Reuderink P, Murgu JP. Regional wave travel and reflections along the human aorta: a study with six simultaneous micromanometric pressures. *Circulation* 1985;72(6):1257-1269.

-
- [10] Kelly R, Hayward C, Avolio A, O'Rourke M. Noninvasive determination of age-related changes in the human arterial pulse. *Circulation* 1989;80(6):1652-1659.
- [11] Benthin M, Dahl P, Ruzicka R, Lindstrom K. Calculation of pulse-wave velocity using cross correlation—effects of reflexes in the arterial tree. *Ultrasound Med Biol* 1991;17(5):461-469.
- [12] Lehmann ED, Hopkins KD, Gosling RG. Aortic compliance measurements using Doppler ultrasound: in vivo biochemical correlates. *Ultrasound Med Biol* 1993;19(9):683-710.
- [13] Mohiaddin RH, Firmin DN, Longmore DB. Age-related changes of human aortic flow wave velocity measured noninvasively by magnetic resonance imaging. *J Appl Physiol* 1993;74(1):492-497.
- [14] Dumoulin CL, Souza SP, Hardy CJ, Ash SA. Quantitative measurement of blood flow using cylindrically localized Fourier velocity encoding. *Magn Reson Med* 1991;21(2):242-50.
- [15] Kraft KA, Itskovich VV, Fei DY. Rapid measurement of aortic wave velocity: in vivo evaluation. *Magn Reson Med* 2001;46(1):95-102.
- [16] Vulliemoz S, Stergiopoulos N, Meuli R. Estimation of local aortic elastic properties with MRI. *Magn Reson Med* 2002;47(4):649-654.
- [17] Bloch F, Hansen WW, Packard M. Nuclear Induction. *Phys Rev* 1946;69:117.
- [18] Purcell EM, Torrey HC, Pound RV. Resonance absorption by nuclear magnetic moments in solids. *Phys Rev* 1946;69:37-38.
- [19] Mansfield P, Grannel PK. NMR “diffraction” in solids? *J Phys C* 1973;6:L422.
- [20] Lauterbur PC. Image formation by induced local interactions: examples employing nuclear magnetic resonance. *Nature* 1973;242:190-191.
- [21] Kumar A, Welte D, Ernst EE. NMR Fourier zeugmatography. *J Magn Reson* 1975;18(1):69-83.
- [22] Reddick RL, Zhang SH, Maeda N. Atherosclerosis in mice lacking apo E. Evaluation of lesional development and progression. *Arterioscler Thromb* 1994;14(1):141-147.

- [23] Nakashima Y, Plump AS, Raines EW, Breslow JL, Ross R. ApoE-deficient mice develop lesions of all phases of atherosclerosis throughout the arterial tree. *Arterioscler Thromb* 1994;14(1):133-140.
- [24] Osada J, Joven J, Maeda N. The value of apolipoprotein E knockout mice for studying the effects of dietary fat and cholesterol on atherogenesis. *Curr Opin Lipidol* 2000;11(1):25-29.
- [25] Hoult DI, Richards RE. The Signal-to-Noise Ratio of the Nuclear Magnetic Resonance Experiment. *J Magn Reson* 1976;24:71-85.
- [26] Itskovich VV, Choudhury RP, Aguinaldo JG, Fallon JT, Omerhodzic S, Fisher EA, Fayad ZA. Characterization of aortic root atherosclerosis in ApoE knockout mice: high-resolution in vivo and ex vivo MRM with histological correlation. *Magn Reson Med* 2003;49:381-385.
- [27] Schneider JE, McAteer MA, Tyler DJ, Clarke K, Channon KM, Choudhury RP, Neubauer S. High-resolution, multicontrast three-dimensional-MRI characterizes atherosclerotic plaque composition in ApoE^{-/-} mice ex vivo. *J Magn Reson Imaging* 2004;20:981-989.
- [28] Herold V, Wellen J, Ziener CH, Weber T, Hiller KH, Nordbeck P, Rommel E, Haase A, Bauer WR, Jakob PM, Sarkar SK. In vivo comparison of atherosclerotic plaque progression with vessel wall strain and blood flow velocity in apoE(-/-) mice with MR microscopy at 17.6 T. *MAGMA* 2009;22(3):159-166.
- [29] Herold V, Parczyk M, Mörchel P, Ziener CH, Klug G, Bauer WR, Rommel E, Jakob PM. In vivo measurement of local aortic pulse-wave velocity in mice with MR microscopy at 17.6 Tesla. *Magn Reson Med* 2009;61(6):1293-1299.
- [30] Hartley CJ, Taffet GE, Michael LH, Pham TT, Entman ML. Noninvasive determination of pulse-wave velocity in mice. *Am J Physiol* 1997;273(1 Pt 2):H494-500.
- [31] Wang YX. Cardiovascular functional phenotypes and pharmacological responses in apolipoprotein E deficient mice. *Neurobiol Aging* 2005;26(3):309-316.
- [32] Reddy AK, Li YH, Pham TT, Ochoa LN, Trevino MT, Hartley CJ, Michael LH, Entman ML, Taffet GE. Measurement of aortic input impedance in mice: effects of age on aortic stiffness. *Am J Physiol Heart Circ Physiol* 2003;285(4):H1464-1470.

-
- [33] Stadler RW, Taylor JA, Lees RS. Comparison of B-mode, M-mode and echo-tracking methods for measurement of the arterial distension waveform. *Ultrasound Med Biol* 1997;23(6):879-887.
- [34] Williams R, Needles A, Cherin E, Zhou YQ, Henkelman RM, Adamson SL, Foster FS. Noninvasive ultrasonic measurement of regional and local pulse-wave velocity in mice. *Ultrasound Med Biol* 2007;33(9):1368-1375.
- [35] Goswami A. *Quantum Mechanics*. Waveland Press Inc, Long Grove, IL, USA, 2-nd edition, 2003.
- [36] Reif F. *Statistische Physik und Theorie der Wärme*. Walter de Gruyter, New York, NY, USA, 1987.
- [37] Haacke EM, Brown RW, Thompson MR, Venkatesan R. *Magnetic Resonance Imaging*. John Wiley and Sons, Inc., Hoboken, NJ, USA 1999.
- [38] Bloch F, Hansen WW, Packard M: Nuclear Induction. *Phys Rev* 1946;70:460-474.
- [39] Callaghan PT. *Principles of nuclear magnetic resonance microscopy*. Oxford University Press, New York, USA 1995.
- [40] Hua J, Hurst GC, Duerk JL. Some noise properties of 2D FT MR images from asymmetrically sampled data. *Med Phys* 1992;19(5):1191-1194.
- [41] Black HS. *Modulation theory*. Van Nostrand, Princeton, USA 1953.
- [42] Haase A, Frahm J, Mathaei D, Hänicke W, Merboldt D. FLASH imaging: rapid NMR imaging using low flip-angle pulses. *J Magn Reson* 1986;67:258-266.
- [43] Zerhouni EA, Parish DM, Rogers WJ, Yang A, Shapiro EP. Human heart: Tagging with MR imaging - A method for noninvasive assessment of myocardial motion. *Radiology* 1988;169:59.
- [44] Axel L, Dougherty L. MR imaging of motion with spatial modulation of magnetization. *Radiology* 1989;171:841-845.
- [45] Edelmann PR, Mattle HP, Kleefeld J, Silver M: Quantification of blood flow with dynamic MR imaging and presaturation bolus tracking. *Radiology* 1989;171:551-556.
- [46] Wehrli F. Time-of-flight effects in MR imaging of flow. *Magn Reson Med* 1990;14:187-193.

-
- [47] Aletras AH, Ding S, Balaban RS, Wen H. DENSE: Displacement encoding with stimulated echoes in cardiac functional MRI. *J Magn Reson* 1999;137:247-252.
- [48] Korin HW, Farzanth F, Wright RC, Riederer SJ. Compensation for effects of linear motion in MR imaging. *Magn Reson Med* 1989;12:99-113.
- [49] van Weeden J, Wendt III RE, Jerosch-Herold M. Motional phase artifacts in Fourier transform MRI. *Magn Reson Med* 1989;11:114-120.
- [50] Nishimura DG, Jackson JI, Pauly JM. On the nature and reduction of displacement artefacts in flow images. *Magn Reson Med* 1991;22:481-492.
- [51] Kuhstrebe J. Diplomarbeit: Flussmessung am Mäuseherzen mit Hilfe von NMR-Methoden. Physikalisches Institut der Universität Würzburg, August 2000.
- [52] Stahlberg F, Thomson C, Soondergaard L, Henriksen O. Pulse Sequence Design for MR Velocity Mapping of Complex Flow: Notes on necessity of low echo times. *Magn Reson Imag* 1994;12(8):1255-1262.
- [53] Axel L, Morton D. MR flow imaging of velocity compensated / uncompensated difference images. *J Comput Assist Tomogr* 1987;11:31.
- [54] Haacke EM, Lenz GW. Improving MR image quality in the presence of motion by using rephasing gradients. *Am J Roentgenology* 1987;148:1251-1258.
- [55] Macgowan CK, Wood ML. Phase-encode reordering to minimize errors caused by motion. *Magn Reson Med* 1996;11:391-398.
- [56] Mörchel P. Quantitative 3D-Bewegungsmessungen am Myokard der Maus mit Phasendifferenz NMR-Methoden bei 17,6 Tesla. Diplomarbeit, Physikalisches Institut der Universität Würzburg, Juni 2003.
- [57] Haacke EM, Patrick JL. Reducing motion artifacts in two-dimensional fourier transform imaging. *Magn Reson Imag* 1986;4:359-376.
- [58] Moran PR. A Flow Velocity Zeugmaathographic Interlace for NMR Imaging in Humans. *Magn Reson Imag* 1982;1:197-203.
- [59] van Dijk P. Direct Cardiac NMR Imaging of Heart Wall and Blood Flow Velocity. *J Comput Assist Tomogr* 1984;8:429-436.

- [60] Bryant DJ, Payne JA, Firmin DN, Longmire DB. Measurement of flow with NMR imaging using a gradient pulse and phase difference technique. *J Comput Assist Tomogr* 1984;8:588-593.
- [61] Drangova M, Zhu Y, Pelc NJ. Effect of artifacts due to flowing blood on the reproducibility of phase-contrast measurements of myocardial motion. *J Magn Reson Imag* 1997;7:664-668.
- [62] Ross R, Glomset JA. Atherosclerosis and the arterial smooth muscle cell: Proliferation of smooth muscle is a key event in the genesis of the lesions of atherosclerosis. *Science* 1973;180(93):1332-1339.
- [63] Brown MS, Goldstein JL. Lipoprotein Metabolism in the Macrophage: Implications for Cholesterol Deposition in Atherosclerosis. *Annual Rev Biochem* 1983;52:223-261.
- [64] Herold V. Dissertation, Physikalisches Institut der Universität Würzburg 2010.
- [65] Frank O. Die Elastizität der Blutgefäße. *Zeitschrift für Biologie* 1920;71:255-272.
- [66] Caro CG, Pedley TJ, Schroter RC, Seed WA. *The mechanics of the circulation*. Oxford University Press, Oxford, UK; 1978.
- [67] Hoppe W, Lohmann W, Markl H, Ziegler H. *Biophysik*. Springer, Berlin, 1978.
- [68] Li JKJ, Melbin J, Riffle RA, Noodergraaf A. Pulse wave propagation. *Circ Res* 1981;49(2):442-452.
- [69] Li JKJ. *Dynamics of the vascular system*. World Scientific Publishing Co. Pte. Ltd., 5 Toh Tuck Link, Singapore 2004.
- [70] Zamir M. *The Physics of Pulsatile Flow*. Greenbaum E, editor. New York, NY, USA: Springer-Verlag New York, Inc.; 2000.
- [71] Womersley JR. Method for the calculation of velocity, rate of flow and viscous drag in arteries when the pressure gradient is known. *J Physiol* 1955;127:553-563.
- [72] Duan B, Zamir M. Viscous damping in one-dimensional wave transmission. *J Acoust Sec Am* 1992;92(6):3358-3363.
- [73] O'Rourke MF, Staessen JA, Vlachopoulos C, Duprez D, Plante GE. Clinical Applications of Arterial Stiffness; Definitions and Reference Values. *Am J Hypertens* 2002;15:426-444.

- [74] Lang RM, Cholley BP, Korcarz C, Marcus RH, Shroff SG. Measurement of regional elastic properties of the human aorta. A new application of transesophageal echocardiography with automated border detection and calibrated subclavian pulse tracings. *Circulation* 1994;90(4):1875-1882.
- [75] Berger DS, Li JK, Noordergraaf A. Differential effects of wave reections and peripheral resistance on aortic blood pressure: a model-based study. *Am J Physiol* 1994;266:H1626-H1642.
- [76] Hartley CJ, Taffet GE, Reddy AK, Entman ML, Lloyd HM. Noninvasive cardiovascular Phenotyping in mice. *ILAR Journal* 2002;43(3):147-158.
- [77] Dujardin JP, Stone DN. Characteristic impedance of the proximal aorta determined in the time and frequency domain: a comparison. *Med Biol Eng Comput* 1981;19(5):565-568.
- [78] Mural RJ, Adams RD, Myers MD et al. A comparison of whole-genome shotgun-derived mouse chromosome 16 and the human genome. *Science* 2002;296:1661-1671.
- [79] Qiao JH, Xie PZ, Fishbein MC, Kreuzer J, Drake TA, Demer LL, Lusis AJ. Pathology of Atheromatous Lesions in Inbred and Genetically Engineered Mice Genetic Determination of Arterial Calcification. *Arterioscler Thromb* 1994;14:1480-1497.
- [80] Gareis D. Diplomarbeit: Design und Bau von linearen Resonatoren und Phased-Arrays für die NMR-Bildgebung bei 17,6 Tesla. Physikalisches Institut der Bayerischen Julius-Maximilians-Universität Würzburg, 2004.
- [81] Wiesmann F, Szimtenings M, Frydrychowicz A, Illinger R, Hunecke A, Rommel E, Neubauer S, Haase A. High-resolution MRI with cardiac and respiratory gating allows for accurate in vivo atherosclerotic plaque visualization in the murine aortic arch. *Magn Reson Med* 2003 Jul;50(1):69-74.
- [82] Madsen EL, Fullerton GD. Prospective tissue-mimicking materials for use in NMR imaging phantoms. *Magn Reson Imaging* 1982;1(3):135-141.
- [83] Frayne R, Gowman LM, Rickey DW, Holdsworth DW, Picot PA, Drangova M, Chu KC, Caldwell CB, Fenster A, Rutt BK. A geometrically accurate vascular phantom for comparative studies of x-ray, ultrasound, and magnetic resonance vascular imaging: construction and geometrical verification. *Med Phys* 1993;20(2 Pt 1):415-425.

- [84] Kraft KA, Fatouros PP, Clarke GD, Kishore PR. An MRI phantom material for quantitative relaxometry. *Magn Reson Med* 1987;5(6):555-562.
- [85] Groch MW, Urbon JA, Erwin WD, al-Doochan S. An MRI tissue equivalent lesion phantom using a novel polysaccharide material. *Magn Reson Imaging* 1991;9(3):417-421.
- [86] Chu KC, Rutt BK. Polyvinyl alcohol cryogel: an ideal phantom material for MR studies of arterial flow and elasticity. *Magn Reson Med* 1997;37(2):314-319.
- [87] Peppas N. Turbidimetric studies of aqueous poly(vinyl alcohol) solutions. *Die Makromolekulare Chemie* 1975;176(11):3433-3440.
- [88] Nambu M; A hydrogel. Japan patent 57/130543. 1982.
- [89] Surry KJM, Austin HJB, Fenster A, Peters TM. Poly(vinyl alcohol) cryogel phantoms for use in ultrasound and MR imaging. *Phys Med Biol* 2004;49(24):5529-5546.
- [90] Nichols WW, O'Rourke MF. Vascular impedance. In: McDonald's blood flow in arteries: Theoretical, experimental and clinical principles. 4th ed. London, UK: Edward Arnold; 1998.
- [91] Dineley J, Meagher S, Poepping TL, McDicken WN, Hoskins PR. Design and characterisation of a wall motion phantom. *Ultrasound Med Biol* 2006;32(9):1349-1357.
- [92] Pannier BM, Avolio AP, Hoeks A, Mancina G, Takazawa K. Methods and devices for measuring arterial compliance in humans. *Am J Hypertens* 2001;15(8):743-753.
- [93] Lankhaar JW, Hofman MBM, Marcus T, Zwanenburg JJM, Faes TJC, Vonk-Noordegraaf A. Correction of phase offset errors in main pulmonary artery flow quantification. *J Magn Reson Imaging* 2005;22:73-79.
- [94] Feintuch A, Ruengsakulrach P, Lin A, Zhang J, Zhou YQ, Bishop J, Davidson L, Courtman D, Foster FS, Steinman DA, Henkelman RM, Ethier CR. Hemodynamics in the mouse aortic arch as assessed by MRI, ultrasound, and numerical modeling. *Am J Physiol Heart Circ Physiol* 2007;292:H884-H892.
- [95] Wang YX, Halks-Miller M, Vergona R, Sullivan ME, Fitch R, Mallari C, Martin-McNulty B, da Cunha V, Freay A, Rubanyi GM, Kauser K. Increased aortic stiffness assessed by pulse wave velocity in apolipoprotein E-deficient mice. *Am J Physiol Heart Circ Physiol* 2000;278(2):H428-434.

- [96] Hartley CJ, Reddy AK, Madala S, Martin-McNulty B, Vergona R, Sullivan ME, Halks-Miller M, Taffet GE, Michael LH, Entman ML, Wang YX. Hemodynamic changes in apolipoprotein E-knockout mice. *Am J Physiol Heart Circ Physiol* 2000;279(5):H2326-2334.
- [97] Zhang SH, Reddick RL, Burkey B, Maeda N. Diet-induced atherosclerosis in mice heterozygous and homozygous for apolipoprotein E gene disruption. *J Clin Invest* 1994;94(3):937-945.
- [98] Zhao X, Pratt R, Wansapura J. Quantification of Aortic Compliance in Mice Using Radial Phase Contrast MRI. *J Magn Reson Imag* 2009; 30:286-291.
- [99] Vlachopoulos C, O'Rourke M. Genesis of the normal and abnormal arterial pulse. *Curr Probl Cardiol* 2000;25(5):303-367.
- [100] Hoeks APG, Brands PJ, Reneman RS. Assessment of arterial distension waveform using Doppler signal processing. *J Hypertens* 1992;10(suppl 6):S19-S22.
- [101] Tymofiyeva O, Schmid F, von Kienlin M, Breuer FA, Rottner K, Boldt J, Richter E-J, Jakob PM. On precise localization of boundaries between extended uniform objects in MRI: Tooth imaging as an example. *Magn Reson Mater Phys Biol Med* (submitted).
- [102] Tymofiyeva O. Dissertation: Magnetic Resonance Imaging in Dental Medicine. Physikalisches Institut der Universität Würzburg 2010.
- [103] Bland JM, Altman DG. Statistical methods for assessing agreement between two methods of clinical measurement. *Lancet* 1986;8(1):307-310.
- [104] Ibrahim EH, Johnson KR, Miller AB, Schaffer JM, White RD: Measuring aortic pulse wave velocity using high-field cardiovascular magnetic resonance: comparison of techniques. *J Cardiovasc Magn Reson* 2010;12:26-38.
- [105] Wolf RL, Ehman RL, Riederer SJ, Rossman PJ. Analysis of systematic and random error in MR volumetric flow measurements. *Magn Reson Med* 1993;30:82-91.

Eigene Veröffentlichungen

Originalarbeiten

Parczyk M, Herold V, Klug G, Bauer WR, Rommel E, Jakob PM. Regional in vivo transit time measurements of aortic pulse wave velocity in mice with high-field MRI at 17.6 Tesla. *J Cardiovasc Magn Reson* 2010 (eingereicht).

Herold V, **Parczyk M**, Mörchel P, Ziener CH, Klug G, Bauer WR, Rommel E, Jakob PM. In vivo measurement of local aortic pulse-wave velocity in mice with MR microscopy at 17.6 Tesla. *Magn Reson Med* 2009;61(6):1293-1299.

Klug G, Kampf T, Ziener C, **Parczyk M**, Bauer E, Herold V, Rommel E, Jakob PM, Bauer WR. Murine atherosclerotic plaque imaging with the USPIO Ferumoxtran-10. *Front Biosci* 2009;14:2546-2552.

Vorträge

Parczyk M, Herold V, Klug G, Bauer WR, Rommel E, Jakob PM. In vivo measurement of regional and local aortic pulse-wave velocity in mice with MRI at 17.6 Tesla. In: *Proceedings of the ESC Congress; 2008; München, Germany.*

Parczyk M, Herold V, Klug G, Bauer WR, Rommel E, Jakob PM. Regional transit time measurement of pulse wave velocity in the murine aorta. In: *Proceedings of the 25-th Annual Scientific Meeting of the ESMRMB; 2008; Valencia, Spain.*

Klug G, Kampf T, Helluy X, **Parczyk M**, Schulze-Till T, Herold V, Rommel E, Jakob PM, Bauer WR. Murine atherosclerotic plaque characterization with multimodal MR-imaging

and data postprocessing at 17.6 Tesla. In: Tagungsband der Tagung für Molekulare Bildgebung; 2007; Kiel, Germany.

Poster

Parczyk M, Klug G, Schulze-Till T, Bauer WR, Rommel E, Jakob PM. In vivo MR-Messungen der Pulswellengeschwindigkeit in der murinen Aorta bei 17.6 Tesla. In: Tagungsband der 10. Jahrestagung der Deutschen Sektion der ISMRM e.V.; 2007; Würzburg, Germany.

Parczyk M, Herold V, Klug G, Schulze-Till T, Bauer WR, Rommel E, Jakob PM. In Vivo Transit Time MR-Measurements of Pulse Wave Velocity in the Murine Aorta at 17.6 Tesla. In: Proceedings of the 16th Annual Meeting of the ISMRM; 2008; Toronto, Canada.

Klug G, Herold V, **Parczyk M**, Bauer E, Schulze-Till T, Rommel E, Jakob PM, Bauer WR. In vivo and ex vivo plaque characterisation in the aortic arch of apoE $-/-$ mice with high-resolution multi-parametric magnetic resonance imaging at 17.6 Tesla. In: Proceedings of the 16th Annual Meeting of the ISMRM; 2008; Toronto, Canada.

Herold V, Klug G, **Parczyk M**, Ziener C, Weber T, Sarkar S, Bauer WR, Rommel E, Jakob PM. In vivo measurement of local pulse-wave velocity in mice with MRI at 17.6 T. In: Proceedings of the 16th Annual Meeting of the ISMRM; 2008; Toronto, Canada.

Herold V, **Parczyk M**, Ziener CH, Klug G, Rommel E, Bauer WR, Jakob PM. In vivo Magnetresonanzbildgebung zur Messung der lokalen Pulswellengeschwindigkeit an der Maus bei 17,6 Tesla. In: Tagungsband der 74. Jahrestagung der Deutschen Gesellschaft für Kardiologie Herz - und Kreislaufforschung e.V.; 2008; Mannheim, Germany.

Ziener CH, Herold V, Klug G, **Parczyk M**, Rommel E, Jakob PM, Bauer WR. Nichtinvasive in vivo Messung der regionalen Pulswellengeschwindigkeit mittels hochauflösender MRI. In: Tagungsband der 74. Jahrestagung der Deutschen Gesellschaft für Kardiologie Herz- und Kreislaufforschung e.V.; 2008; Mannheim, Germany.

Klug G, Herold V, **Parczyk M**, Bauer E, Schulze-Till T, Rommel E, Jakob PM, Bauer WR. In vivo und ex vivo Plaque Charakterisierung im Aortenbogen von apoE $^{(-/-)}$ -Mäusen mittels hochaufgelöster multi-parametrischer MRT bei 17,6 Tesla. In: Tagungsband des

114. Kongresses der Deutschen Gesellschaft für Innere Medizin; 2008; Wiesbaden, Germany.

Ziener CH, Herold V, **Parczyk M**, Klug G, Kampf T, Rommel E, Jakob PM, Bauer WR. In-vivo-Messung der regionalen und lokalen Pulswellengeschwindigkeit in der Aorta der Maus mittels MR-Bildgebung bei 17,6 Tesla. In: Tagungsband des 114. Kongresses der Deutschen Gesellschaft für Innere Medizin; 2008; Wiesbaden, Germany.

Klug G, Herold V, **Parczyk M**, Bauer E, Schulze-Till T, Rommel E, Jakob PM, Bauer WR. In vivo and ex vivo plaque characterisation in the aortic arch of apoE $-/-$ mice with high-resolution multi-parametric magnetic resonance imaging at 17.6 Tesla. In: Proceedings of the ESC Congress; 2008; München, Germany.

Herold V, **Parczyk M**, Klug G, Bauer WR, Rommel E, Jakob PM. In vivo measurement of regional pulse-wave velocity in mice with twodimensional in-plane flow encoded PC-Cine-MRI at 17.6 T. In: Proceedings of the 25-th Annual Scientific Meeting of the ESMRMB; 2008; Valencia, Spain.

Parczyk M, Herold V, Klug G, Bauer WR, Rommel E, Jakob PM. Regional transit time measurement of pulse wave velocity in the murine aorta. In: Proceedings of the 17th Annual Meeting of the ISMRM; 2009; Honolulu, Hawaii, USA.

Klug G, Basse-Lüsebrink T, Schnell C, Kampf T, Bauer E, Herold V, **Parczyk M**, Rommel E, Stoll G, Jakob PM, Bauer WR. $^1\text{H}/^{19}\text{F}$ Molecular MR-Imaging in Mouse Models of Acute and Chronic Inflammation. In: Proceedings of the 17th Annual Meeting of the ISMRM; 2009; Honolulu, Hawaii, USA.

Herold V, **Parczyk M**, Klug G, Bauer WR, Jakob PM, Rommel E. In vivo measurement of regional and local pulse-wave velocity in mice with MRI at 17.6 T. In: Proceedings of the 17th Annual Meeting of the ISMRM; 2009; Honolulu, Hawaii, USA.

Lebenslauf

Marco Parczyk

St-Rochus-Straße 38
97078 Würzburg

Persönliche Daten

geboren am
Nationalität
Familienstand

18.07.1976 in Halle an der Saale
deutsch
ledig

Schulbildung

07/83 - 07/91
07/91 - 07/96

Grundschule in Nebra an der Unstrut
Gymnasium Laucha, Landesschule Pforta,
Wyoming High School, Cincinnati, OH, USA

Wehrdienst

07/96 - 09/97

Elektronikinstandsetzung Regensburg

Studium

10/97 - 11/03

Studium der Physik
Bayerische Julius-Maximilians-Universität Würzburg
University of New Mexico, Albuquerque, NM, USA

Diplomarbeit am Lehrstuhl für Experimentelle Physik V
der Bayerischen Julius-Maximilians-Universität Würzburg:
“Low-Field NMR Hardware Methods”

12/03 - 06/04

Wissenschaftliche Hilfskraft an der
Bayrischen Julius-Maximilians-Universität Würzburg

Promotion

seit 07/04

Promotion am Lehrstuhl für Experimentelle Physik V
der Bayerischen Julius-Maximilians-Universität Würzburg:
“In vivo NMR-methods to study the effects of
atherosclerosis in mice”

Beruf

seit 08/09

Medizinphysiker an der Klinik und Poliklinik für Strahlentherapie
des Universitätsklinikums Würzburg

Würzburg, 13. August 2010

Marco Parczyk

Ehrenwörtliche Erklärung

gemäß §5 Abs. 2 Ziff. 2, 5 und 3
der Promotionsordnung für die Fakultät für Physik und Astronomie
der Julius-Maximilians-Universität Würzburg
vom 22. September 2003 (KWMBI II 2004 S. 2504)

Hiermit erkläre ich ehrenwörtlich, dass ich die Dissertation selbständig und ohne die Hilfe eines Promotionsberaters angefertigt und keine anderen als die angegebenen Quellen und Hilfsmittel benutzt habe.

Die Dissertation wurde bisher weder vollständig noch teilweise einer anderen Hochschule mit dem Ziel, einen akademischen Grad zu erwerben, vorgelegt.

Am 15. Juni 2004 wurde mir von der Universität Würzburg der akademische Grad “Diplom-Physiker (Univ.)” verliehen. Weitere akademische Grade habe ich weder erworben noch versucht zu erwerben.

Die Dissertation wurde von Prof. Dr. Peter M. Jakob betreut.

Würzburg, 13. August 2010

Marco Parczyk

Danksagung

Diese Arbeit wurde von der Deutschen Forschungsgemeinschaft im Rahmen des SFB 688 **Mechanisms and imaging of cardiovascular cell-cell-interactions** gefördert.

Mein Dank geht an die folgenden Personen, die mich bei der Anfertigung der Arbeit unterstützt haben und ohne welche diese Arbeit nicht entstanden wäre:

Prof. Dr. Peter M. Jakob hat mir die Möglichkeit gegeben, diese Arbeit an seinem Lehrstuhl anzufertigen. Für die interessanten Diskussionen und seine konstruktive Kritik bin ich besonders Dankbar.

Dr. Frank Wiesmann machte mir das Angebot, unter seiner Obhut Pulswellengeschwindigkeiten an der murinen Aorta zu untersuchen. Leider konnte er die Ergebnisse seiner Idee nicht mehr erleben.

Prof. Dr. Dr. Wolfgang R. Bauer und **PD Dr. Eberhard Rommel** übernahmen die Betreuung des Forschungsprojektes. Prof. Dr. Dr. Wolfgang R. Bauer danke ich für sein großes Interesse an der Arbeit und für die vielen Freiräume, die er mir bei der Ausfertigung der Arbeit ließ. PD Dr. Eberhard Rommel danke ich für die Betreuung der Arbeit. Er hat mir besonders bei technischen Fragestellungen oft geholfen.

Volker Herold und **Dr. Gert Klug** waren meine Mitarbeiter. Wir waren ein gutes Team. Danke für die Zusammenarbeit.

Prof. Dr. Peter M. Jakob, PD Dr. Eberhard Rommel, Volker Herold und **Robert Mason** danke ich für das Korrekturlesen der Arbeit.

Sabine Voll, Carmen Bundschuh, Esra Lang, Sonngard Vay und **Philip Kagerbauer** waren nicht nur die besten Zimmerkollegen, die man sich vorstellen kann, auch bei jeglichen Fragen zu Mäuseaorten, Chemikalien, Pulswellenphantomen und sogar psychologischer Matlab-Programmierung konnten sie immer helfen.

Reza Kharrazian und **Volker Behr** waren meine Lehrmeister bezüglich der MR-Hardware.

Ich danke auch allen andren Mitarbeitern am **Lehrstuhl für Experimentelle Physik 5**. Es war schön mit Euch zu arbeiten.

Meinen Kollegen von der Strahlenklinik, besonders **Prof. Dr. Otto Sauer, Dr. Klaus Bratengeier** und **Dr. Franz Schwab** danke ich für ihre Unterstützung bei der Ausfertigung dieser Arbeit.

Besonderer Dank geht an meine Freunde **Steffi Sparka, Antje Unterforsthuber, Christina Baacke** und **Armin Porea**, auch weil sie mir, wenn ich sie brauchte, immer eine große Stütze waren. A big 'thank you' goes to my American family **Carolyn, Robert, Tony, Glenna, and Kate Mason**. Ich danke auch allen Freunden, die ich hier aus Platzgründen nicht persönlich aufführen kann.

Ebenso danke ich meiner Familie, meinen Schwestern **Nancy** und **Kathi**, dem Hasen **Dominic Bisignano, Nils** und **Arvid Schöffner**, meinen Großeltern **Gerhard** und **Elfriede Hesse** und Oma **Leni Herda**, Familie **Silvia** und **Axel Herda** - ja, auch Dir, Onkel - natürlich, und meinen Eltern **Gudrun** und **Uwe Parczyk**.

Euch allen ein großes Danke von Herzen!

